UNIVERSITY OF CALIFORNIA
SANTA CRUZ

NUMERICAL ADVENTURES IN EXOPLANET FORMATION, DETECTION AND CHARACTERIZATION

A dissertation submitted in partial satisfaction of the
requirements for the degree of

DOCTOR OF PHILOSOPHY

in

ASTRONOMY AND ASTROPHYSICS

by

Stefano Meschiari

June 2012

The Dissertation of Stefano Meschiari
is approved:

Professor Gregory Laughlin, Chair

Professor Steven S. Vogt

Professor Daniel C. Fabrycky

Tyrus Miller
Vice Provost and Dean of Graduate Studies

Table of Contents

List of Figures

List of Tables

Abstract

Numerical Adventures in Exoplanet Formation, Detection and Characterization

by

Stefano Meschiari

In this thesis I investigate the use of numerical modeling techniques applied to the study of extrasolar planets. In the first part (Chapters 2-4) I discuss the algorithms and applications of the SYSTEMIC code in the detection and characterization of exoplanets through radial velocity (RV) and transit timing observations. The second part (Chapters 5-6) deals with hydrodynamic and N-body simulations applied to the study of planet formation. For each chapter, I provide a detailed review of the numerical techniques involved in the respective introductions.

Chapter 2 discusses several aspects related to the dynamical fitting of RV observations. I introduce the SYSTEMIC package I developed, and describe several applications of the numerical algorithms developed for the code. As a case study, I investigate the dynamical fitting of HD128311 and the characterization of the 2:1 mean motion resonance (MMR) through radial velocities and a small number of central transit times. I present an updated Keck RV dataset and show that the addition of three years of new RV coverage yields only a modest improvement in the characterization of the system.

In Chapter 3, I study planet detection through transit timing variations (TTV), deviations from linear transit ephemeris that can be caused by additional planets exerting gravitational perturbations on a transiting planet. I created synthetic RV and TTV datasets for several planetary configurations, with the intent of modeling timing observations from the *Kepler* mission. I use the algorithms described in Chapter 2 to solve the so-called "inverse problem", the task of characterizing additional, non-transiting planets through their signatures in the RV and

TTV datasets of transiting. I show that the space of the best-fitting solutions may be remarkably degenerate if the perturbing planet is not observed directly (e.g. as in the case of Kepler 19-c), and that more extensive RV coverage can be used to break the degeneracy.

In Chapter 4, I present the discovery of four new exoplanet candidates characterized with Keck/HIRES RV observations. The new exoplanets discovered around the host stars HD31253, HD218566, HD177830 and HD99492 comprise masses between $\mathcal{M} \sin i \approx 27 \mathcal{M}_{\oplus}$ to $\mathcal{M} \sin i \approx 8 \mathcal{M}_{J}$. Of particular interest for the scope of this thesis, HD177830 is currently the only multiple-planet system orbiting a binary with $a_B < 100$ AU. This separation is slightly below the limit at which the binarity of the system influences planet formation. Finally, we strengthen the case for the non-detection of HD74156d, the detection of which was claimed to be in accordance to the "Packed Planetary System" hypothesis.

Chapter 5 explores a class of self-gravitating instabilities driven by features in the surface density of protoplanetary disks (*groove modes*). The emergence of these instabilities is studied via a generalized eigenvalue code and full two-dimensional hydrodynamical simulations. I find that gaps in the surface density, such as those naturally carved in response to the formation of a giant planet, can excite a global two-armed mode at comparatively lower disk masses than in absence of such gaps.

Chapter 6 describes a new code, SPHIGA, used to explore the issue of forming planets in circumstellar (CS) or circumbinary (CB) orbits during the planetesimal accretion phase and its feasibility within the core accretion framework. I investigate the balance between accreting and erosive impacts for the circumbinary planet Kepler 16-b and the feasibility of planet formation *in situ* as opposed to migration of an embryo formed at or outside the ice line.

This dissertation includes reprints of the following material: (a) Meschiari, S., & Laughlin, G. 2008, ApJ, 679, L135; (b) Meschiari, S., Wolf, A. S., Rivera, E., et al. 2009, PASP, 121, 1016; (c) Meschiari, S., & Laughlin, G. P. 2010, ApJ, 718, 543; (d) Meschiari, S., Laughlin, G.,

Vogt, S. S., et al. 2011, ApJ, 727, 117; (e) Meschiari, S., 2012, ApJ, in press.

Io stimo più il trovar un vero, benché di cosa leggiera, che 'l disputar lungamente delle massime questioni senza conseguir verità nissuna.

– Galileo Galilei

To doubt everything or to believe everything are two equally convenient truths; both dispense with the necessity of reflection.

– Henri Poincarè

[...] Have no respect whatsoever for authority; forget who said it and instead look what he starts with, where he ends up, and ask yourself, "Is it reasonable?"

– Richard Feynman

To the love of my life and my family:

♡.

Acknowledgments

I want to thank my advisor Greg Laughlin for his continued guidance, generosity and creative input throughout my undergraduate and graduate career. His foresight in shaping my academic path through gentle prodding, while ensuring I was conducting my research in an independent manner, made the road to this thesis a fulfilling one. I also want to thank Daniel Fabrycky and Steve Vogt for showing me a successful career path.

I am greatly indebted with my fellow graduate students, Anna, Anne, Feña, Javiera, Judy, Rachel, Valentino and everyone else. Grad school would have not been the same without frequent coffee (and ice cream, and latte) breaks, campus strolls, and chit-chats in the sun (sometimes involving science, too!). This dissertation year was made just bearable by the constant commiseration with my officemate Judy, without whom the job search would have been only half as "fun".

A lot of friends cheered and supported me to the end of this journey. There are too many people to mention and too many languages involved to really do justice to the amount of love and friendship that I am fortunate to be surrounded with. My dearest friends from Italy, Andrea, Claudia, Daniela, Federica, Giulia, Lucia (x2) and Pietro were there during the whole trek, and we have shared each other's good luck and sorrows. My American family was just as fundamental to my sanity and happiness in these six years in the United States. Finally, during those long nights coding, many friends kept me company in a little window on the screen: Lucy and Ethel, Liz and Jack, Homer and Marge, Fran and Maxwell, Dorothy, Rose, Blanche and Sophia, Fry and Leela, Ted and Barney, Frasier and Niles, Jerry and Elaine, Hyacinth B-U-C-K-E-T and many more.

My family, Silvano, Patrizia and Valentina had faith in me since the beginning, helped me grow and be proud of who I am. None of this would have been possible without their help,

affection and strength. My partner Daniel helped me more than anyone else with his patience, his love and, most of all, his ability to make me happy at any given time. He gave me a goal to strive for with my work.

Finally, I dedicate this thesis to my honorary nephews who were born during graduate school, Davide and Gaël, and the nephew I am about to meet, Jacopo. I can't wait to show you around in this beautiful universe we live in.

Chapter 1

Introduction

The size and variety of the planetary census has come a long way from the discovery of the first hot Jupiters around main-sequence stars. Driven by increasingly prolific and precise detection methods, astronomers are pushing the observational envelope to include long-period giants, super-Earths and terrestrial-mass, habitable planets (the "holy grail" of exoplanets). In order to extract maximum value from these expensive long-term surveys, analysis techniques and algorithms have also become more sophisticated and adept at teasing out planetary signals from stellar noise. Thanks to this combination of observational and reduction advances, the wealth of diverse planet candidates is ushering an era where observations can provide detailed insights into the physics of planet formation in regimes very different than those of our own Solar System. In parallel, observations of protoplanetary disks and young stellar systems at various stages of their evolution are providing new constraints for theories of planet formation.

In spite of these observational advancements, several fundamental shortcomings persist in our understanding of the process of planet formation. Due to the enormous dynamical range involved in the assembly of planetary embryos ($\gtrsim 10^8$ cm) from dust ($\sim 1 - 10\mu$m) within the core accretion paradigm, it is presently beyond our computational capabilities to attempt to

model planet formation with end-to-end simulations. Even if that were feasible, models still need to address the uncertainties surrounding the relative importance of the many physical processes at play and the transition between different scales of planetary buildup.

Since our Solar System and the large majority of planet candidates discovered to date orbit single stars, our understanding of planet formation is firmly rooted in dynamical systems where the bulk of the mass is concentrated in the central body and the bulk of the angular momentum in the protoplanetary disk. However, a growing fraction of the planetary census is represented by planet candidates belonging to a binary or multiple system, in either circumstellar or circumbinary configurations. Far from being exotic oddities, planet candidates in binary systems represent an even more stringent test of the environments in which our theories of planet formation are applicable, due to the more extreme conditions in which planetary assembly must be successful. The recent discovery of Kepler 16-b, Kepler 34-b and Kepler 35-b, among the more than 2,000 eclipsing binaries monitored by *Kepler*, implies a $\approx 1\%$ frequency of circumbinary planets with comparable transit probabilities. There is also considerable theoretical and observational interest in the α Centauri system, and the feasibility of forming a terrestrial planet in the habitable zone of either stellar component. The system is composed of a close binary with nearly solar-mass components and moderate eccentricity, orbited by a distant third star (Proxima). The system provides excellent candidates from an observational point of view due to their brightness, absence of long-term variability, position in the sky and relatively high metallicity. These appealing features made the system a long-term target for several radial velocity surveys and the subject of numerous theoretical works. However, a straightforward extension of the standard planet formation paradigm in the presence of the binary companion gives rise to a different set of weaknesses in our theory of planet formation, including the 'planetesimal bottleneck' discussed in this work.

This dissertation investigates two broad themes. The first part deals with planet detec-

tion using radial velocity (RV) and transit timing observations, using both synthetic test cases and actual data taken at the Keck telescope (§2, §3, §4). The second part investigates planet formation in two regimes outside the parameter space well-trodden in the literature, namely, giant planet formation in a moderately massive protoplanetary disk (§5) and planet formation in a circumbinary configuration (§6).

In the present chapter, I begin with a broad introduction to the current state of exoplanetary science and some of the themes that will be discussed in this dissertation. In Section (1.1), I briefly review the methods for detecting planet candidates and the composition of the current planetary census. In Section (1.2), I present a broad overview of planet formation. In Section (1.3), I review some of the numerical schemes used in the rest of the dissertation.

1.1 Planet detection

Since the stunning discoveries of the first planets orbiting a pulsar (PSR 1257+12; Wolszczan & Frail 1992) and the first planet around a main-sequence star (the hot Jupiter 51 Peg; Mayor & Queloz 1995), planetary science has witnessed a *renaissance*, becoming once again a fashionable and fast-moving field. Figure 1.1 is a testament to this renewed interest and the role of exoplanet detection in driving both theoretical and observational work.

Figure 1.2 shows a mass/semimajor axis/eccentricity diagram of the known exoplanet candidates. To date, 763 candidates have been detected using a variety of methods and survey programs[1]. Each technique is naturally biased towards different regions of the diagram: for instance, radial velocity and astrometry are better suited to detecting long-period planets than transits, and direct imaging is most sensitive to bright, massive planets at even larger distances. Furthermore, masses may be known only as a lower limit (in the case of radial velocity) or even

[1] http://www.exoplanet.eu, retrieved on April 29, 2012

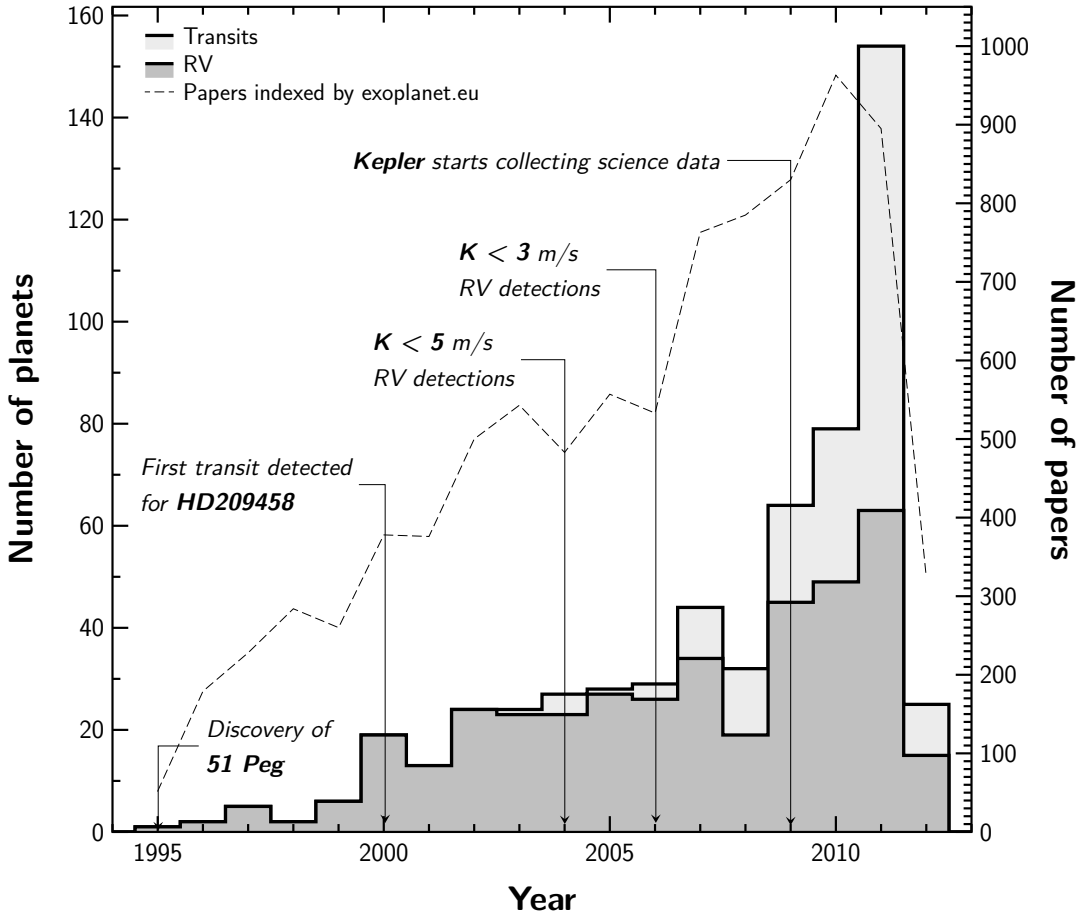

Figure 1.1: Plot of number of planets published per year. Notice the increasing importance of the transit method in driving the field forward. Overlaid is the approximate number of papers published per year in the field of exoplanets, retrieved from the SYSTEMIC spider (as indexed by exoplanet.eu.)

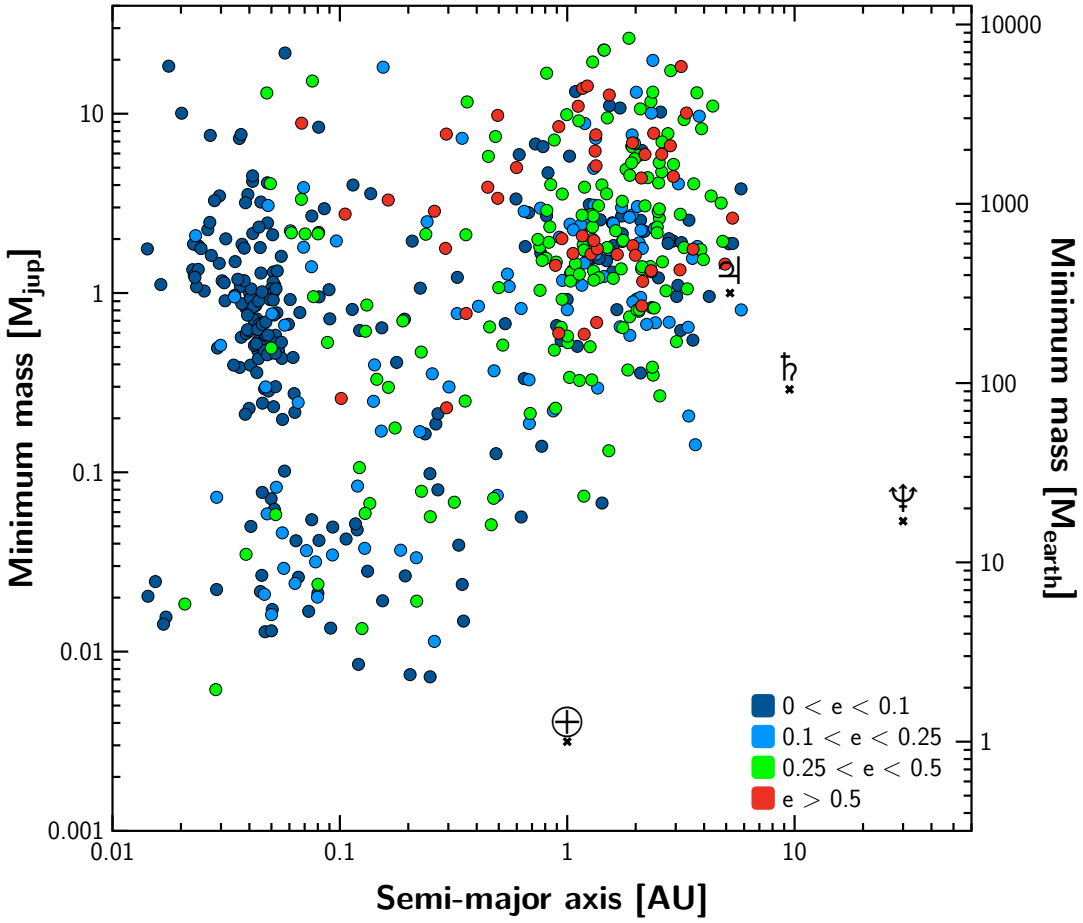

Figure 1.2: Plot of minimum-mass vs. semi-major axis for all the known exoplanets as of April 2012; the symbols are colored according to the reported eccentricity. Earth, Jupiter, Saturn and Neptune are plotted for comparison.

unknown (in the case of transits). In the latter situation, only radial velocity follow-up or the detection of transit timing variations can constrain planetary masses.

Nonetheless, it is possible to discern a number of clear features in Figure 1.2 independent of these limitations:

- The distribution of massive exoplanets is bimodal in period, with a population of hot Jupiters clustering around a period of a few days and long-period eccentric planets with $P > 200$ d. Outside a few AUs the limited time span of RV surveys prevent the secure detection of longer-period planets.

- A new population of relatively low-mass planets (super-Earths, $\mathcal{M} \lesssim 10\mathcal{M}_\oplus$) has been uncovered by precise RV (e.g. Rivera et al. 2005, Mayor et al. 2009a, Vogt et al. 2010) and transit observations (e.g. Léger et al. 2009); on the other hand, there is a distinct lack of planets with $10 \lesssim \mathcal{M} \lesssim 100\mathcal{M}_\oplus$ and $P \lesssim 50$ days, despite the relative ease of detection.

- Correcting for detection biases in the mass domain, the planet frequency increases at smaller masses (Butler et al. 2006, Howard et al. 2011).

- Planets with $P \lesssim 10$ days are tidally circularized, whereas planets at larger distances have an eccentricity distribution peaking at $e \approx 0.25$, with a long tail. Such high eccentricities are presumably excited by planet-planet scattering (e.g. Jurić & Tremaine 2008) or Kozai oscillations (Fabrycky & Tremaine 2007), as is likely the case of the super-eccentric planet HD80606 (Wu & Murray 2003, Laughlin et al. 2009).

Explaining these features and other correlations, including mass-distance and metallicity correlations, is the domain of planet synthesis models (e.g., Ida & Lin 2004, Mordasini et al. 2009). The validity of these models, which distill the current state of planet formation theory into large-scale Monte Carlo simulations, can be tested by comparison with the observed plan-

etary census. Therefore, in order to test and push theory forward, it is imperative to continue improving the completeness of the sample (together with the pursuit of the alluring habitable Earth twins).

In the next few sections we describe the radial velocity and transit detection methods. Given the rapid progress in the field since the writing of Chapters §2 and §3 (thanks in particular to the launch of *Kepler*), we will review some of the most recent literature, where appropriate, or point the reader to up-to-date references. For the sake of brevity, we will not cover other successful techniques, including microlensing (Bennett 2008), astrometry (Benedict et al. 2002, Bean & Seifahrt 2009), stellar pulsations (Silvotti et al. 2007), direct imaging (Chauvin et al. 2005, Kalas et al. 2008, Marois et al. 2008) and pulsar timing (Wolszczan & Frail 1992).

1.1.1 Radial Velocity

The radial velocity method searches for periodic Doppler shifts in the absorption spectra of stars caused by motion along the line of sight as the star orbits the center of mass of the system. To first approximation, the resulting signal is a linear superposition of Keplerian orbits with semi-amplitude

$$K_j = \left(\frac{2\pi G}{P_j}\right)^{1/3} \frac{\mathcal{M}_j \sin i_j}{(\mathcal{M}_\star + \mathcal{M}_j)^{2/3}} \frac{1}{\sqrt{1-e_j^2}}\,, \tag{1.1}$$

where $\mathcal{M}_\star$ is the mass of the star and $\mathcal{M}_j$, e_j and i_j are mass, orbital eccentricity and orbital inclination to the plane of the sky of the j-th planet, respectively (Murray & Dermott 2000). In general, mass and inclination cannot be determined independently from the RV signature alone; therefore, we can only infer the *minimum mass* $\mathcal{M}_j \sin i_j$.

The radial velocity signal has to be extracted from spectral shifts with incredible precision: better than 12 m/s for a Jupiter-like planet at 5.2 AU, 3 m/s for the typical super-Earth and better than 0.1 m/s for an Earth-like planet in the habitable zone. These translate to spectral

shifts of the order of 10^{-4} to $10^{-6}\mathring{A}$. Worse, a naïve exposure taken with the highest-resolution spectrograph available would still be ineffectual due to thermal flexures and pressure fluctuations, which alone produce shifts of the order of hundreds of m/s and completely overwhelm any planetary signal.

Modern precision radial velocity sidesteps this issue by employing high-resolution echelle spectrographs and taking simultaneous reference spectra for continuous calibration of the stellar spectra. The two prominent approaches to coping with drifts are the thorium-argon reference (e.g. ELODIE, CORALIE, HARPS; Mayor et al. 2003) and the iodine absorption cell techniques (e.g. HIRES; Vogt et al. 1994).

The latter technique, used to obtain the data in Table A.1, employs an absorbing cell filled with low-pressure gaseous iodine. This cell is interposed on the light beam, placing a forest of strong absorption lines on top of the shifted stellar spectrum. The resulting spectrum will be composed of a blend of iodine and stellar lines, both suffering from instrumental drifts in the same manner and convolved with the point spread function (PSF) of the instrument:

$$I_{obs}(\lambda) \propto [T_{iodine}(\lambda) I_{template}(\lambda + \Delta\lambda)] * \mathrm{PSF} \tag{1.2}$$

(Butler et al. 1996). In Equation (1.2), T_{iodine} is a high-resolution spectrum of the iodine cell, $I_{template}$ is a high-resolution template spectrum of the star and the $*$ operator indicates a convolution. Thus, a typical observing night follows these steps to obtain the shift $\Delta\lambda$:

1. A sample of targets is selected, depending on the observability conditions of each object and instrumental constraints (e.g. altitude/azimuth restrictions, telescope slews, stellar brightness, etc.).

2. A featureless star (typically, a B star) is observed through the iodine cell held at a fixed temperature, yielding a spectrum of the iodine cell convolved with the PSF of the instrument. The PSF is then derived by comparison with tabulated spectra of iodine, and used

to deconvolve the stellar templates.

3. Several flat fields are taken to compensate for pixel-to-pixel sensitivity variations in the CCD.

4. For each star, the spectrum is divided into several bins and modeled using Equation 1.2. The shift $\Delta\lambda/\lambda$ is derived by minimizing the χ^2 of the model and the PSF parameters.

Thanks to these instrumental advances, instrumental error budgets of better than 1 m/s are now attainable. Nonetheless, a number of intrinsic limitations make reaching the sub-m/s precision, which is required to detect Earth-mass planets around solar-type stars ($K \approx 0.1$ m/s), a challenge.

Photon statistics establishes an unavoidable baseline Poisson noise, due to the quantum fluctuations in the electromagnetic field. However, this can be minimized by restricting the sample to bright stars such that photon noise is a small fraction of the error budget, or by increasing the number of photons collected (e.g. by employing a more efficient CCD or a larger telescope mirror). More troublingly, intrinsic stellar noise, both on the short term (of the order of tens of minutes; e.g. atmospheric oscillations, granulation, and other magnetic activity) and long term (e.g. magnetic activity cycles) can dominate the error budget in the form of "jitter". Short-term activity can generally be averaged out by combining several exposures, bringing the error budget down to $\gtrsim 0.7$ m/s for the quietest stars. This precision can generally only be achieved with old late-G to early-K stars showing small RV scatter and low activity indicators. However, by the very design of such a survey, this presents the risk of only selecting stars that do not display significant RV scatter, and therefore may not harbor any planet at all (e.g. Pepe et al. 2011). For an in-depth review of the noise sources that have to be taken into account in high-precision RV surveys, see Lovis & Fischer (2010) and references therein.

Overall, this technique has been the most prolific in terms of number of planets discov-

ered; as of April 2012, 399 planets were first detected through their radial velocity signal. The RV technique is intrinsically biased towards planets that produce large Ks (Equation 1.1): massive, short-period planets will be more easily detected, which explains the initial preponderance of hot Jupiters among planet candidates. Long-period and very eccentric orbits, on the other hand, suffer from inadequate phase coverage (e.g. Cumming 2004, Cumming et al. 2008).

1.1.2 Transits

Transit surveys look for photometric variations consistent with planets eclipsing their parent star. Since the detection of transits for HD209458 b (Charbonneau et al. 2000, Henry et al. 2000), the transit method has acquired an increasingly instrumental role in the advancement of exoplanetary science. This is a result of the low cost of bootstrapping automated networks of telescopes for photometric monitoring (e.g. Alonso et al. 2004, Charbonneau et al. 2009, Bakos et al. 2011), the advent of dedicated space missions (such as CoRoT; Léger et al. 2009) and even involvement of amateur astronomers (Gary 2009). The launch of *Kepler* in 2009 and the following two years of continuous photometric monitoring of 150,000 target stars has further accelerated the field, producing a large number of new, confirmed planets and "*Kepler* Objects of Interest" (KOI)[2]. These new discoveries have extended the planetary sample into mass regimes and system architectures previously unexplored (e.g. Lissauer et al. 2011, Doyle et al. 2011, Gautier et al. 2012).

A planetary transit is a rare event, as only a small fraction

$$P_{tr} = 0.0045 \left(\frac{1\mathrm{AU}}{a}\right) \left(\frac{R_* + R_{pl}}{R_\odot}\right) \left[\frac{1 - e\cos(\frac{\pi}{2} - \varpi)}{1 - e^2}\right] \tag{1.3}$$

of orbital elements is geometrically aligned to produce an eclipse along the line of sight; additionally, only a small fraction of the orbital period is spent in transit. Therefore, transit campaigns

[2]See http://kepler.nasa.gov/Mission/discoveries/ for an up-to-date list of confirmed planets

have to survey a large number of stars looking for photometric variations. When several transits are observed, the period, phase, impact parameter and inclination are precisely determined by the flux loss, timing and duration of the eclipses. When occultations (i.e. when the planet is hidden by the parent star) are detected, they place tight constraints on a combination of eccentricity and argument of pericenter as well (Deming et al. 2007).

1.1.3 Mass determination and Transit Timing Variations

Obtaining the actual mass of candidates that are detected through their transits can be challenging: the flux drop observed in transit only determines the ratio of the planetary radius to the stellar radius. Therefore, follow-up with radial velocity observations is often used to determine the true masses of the candidates and ascertain their planetary status (e.g. Borucki et al. 2010b). Analogously, follow-up of radial velocity observations with transit monitoring can be used to determine true masses (as the inclination is determined from the impact parameter). As an example, Figure (1.3) shows radial velocity (from HARPS, KECK and HET) and transit timing (including Hubble, Spitzer, and amateur observations) for the Neptune-mass planet GJ436 b (Deming et al. 2007). In this case, both primary transits and occultations were detected, accurately determining the orbital elements. Radial velocities establish the true mass of b through the semiamplitude K; datasets from different observatories can be combined to produce a longer baseline, provided they are appropriately shifted to a common zero-point offset.

Follow-up via RV observations is not always practical, or even feasible. This can be due to the low mass of the planets (e.g. Lissauer et al. 2011), faintness of the star (Ford et al. 2012) or high stellar activity (Queloz et al. 2009). This is especially problematic for *Kepler* stars, due to the faintness and high stellar activity of its sample (Gilliland et al. 2011). Additionally, its stated mission goals are the detection of small, rocky planets in the habitable zone, which are at present outside the reach of Doppler surveys.

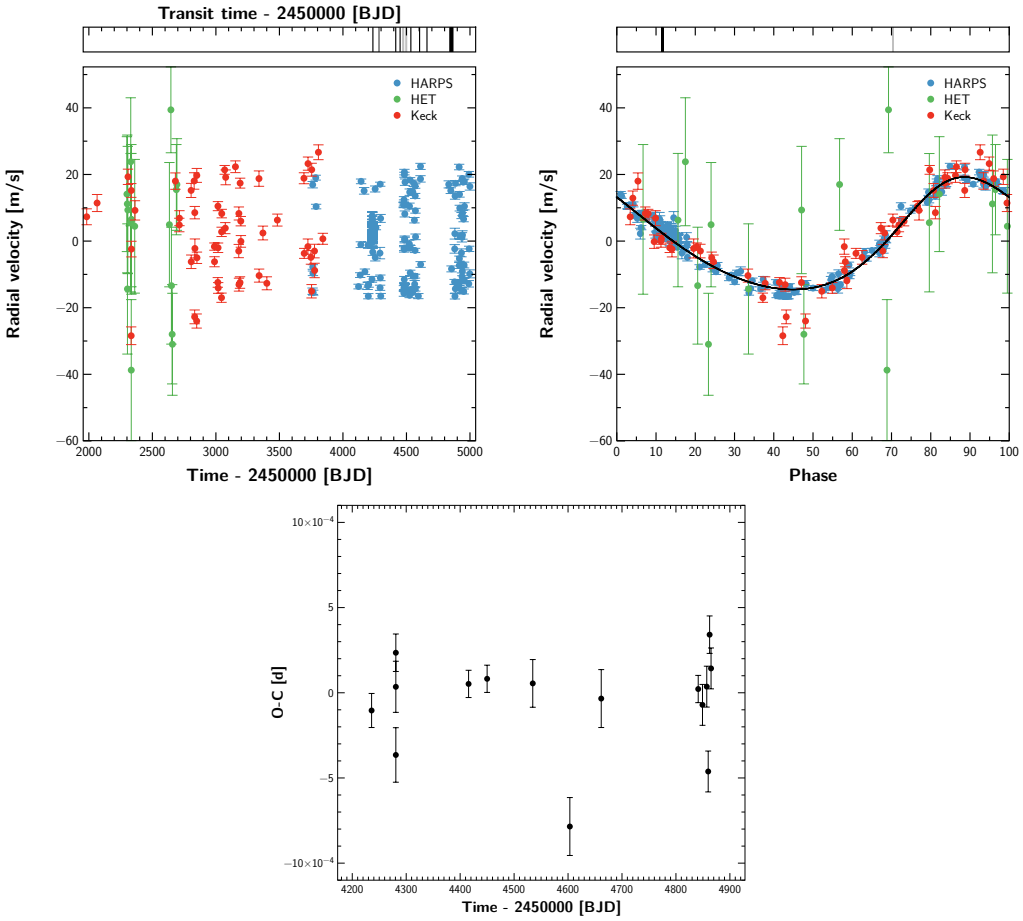

Figure 1.3: (Left) Full radial velocity (symbols; showing HET, Keck and HARPS data) and transit timing dataset (vertical lines; black lines are transits, gray lines are occultations) for GJ436. (Right) Dataset shifted and folded according to the best-fit model (solid line). (Bottom) Transit timing residuals.

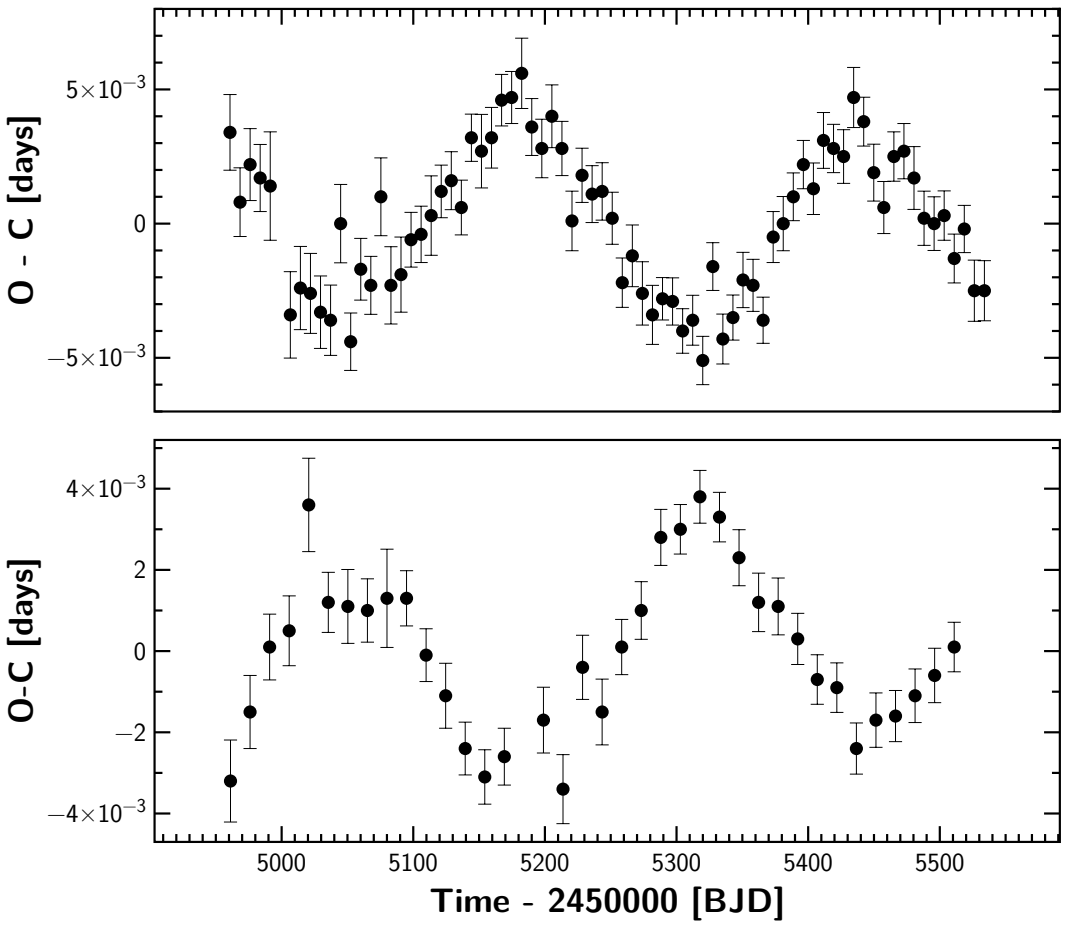

Figure 1.4: Transit timing variations for Kepler-18 c (top) and d (bottom).

Transit timing variations (TTV; deviations from a linear ephemeris of the eclipses, due to the dynamical perturbation of one or more companions) provide a new avenue for confirming planet candidates from transit observations alone. These deviations can be readily observed with *Kepler*: Figure (1.4) shows, as an example, the TTVs for Kepler-18 c and d (Cochran et al. 2011).

A statistical analysis of the *Kepler* sample showed that at least 11% of systems showed deviations suggestive of TTVs (Ford et al. 2011). Chapter §3 (Meschiari & Laughlin 2010; written before the first *Kepler* data became available) reviews some of the difficulties associated with this method when the perturbing object is non-transiting (see also Nesvorný 2009, Veras et al. 2011, Boué et al. 2012), due to degeneracies in the fitting process. Such complications impeded the full characterization of Kepler-19 c (Ballard et al. 2011). However, when all planets participating in dynamical interactions transit, it is possible to derive constraints on their mass that confirm their planetary status (e.g. Lissauer et al. 2011, Ford et al. 2012, Fabrycky et al. 2012a).

An analogous procedure can be applied to eclipsing timing variations (ETVs), which are commonly detected in the *Kepler* binary catalog (Slawson et al. 2011). ETVs were used to determine the planetary nature of the circumbinary planets Kepler-16, 34 and 35 b (Doyle et al. 2011, Welsh et al. 2012).

1.2 Planet formation

In this section we briefly cover the stage of planet formation where planetesimals assemble into embryos. We refer the reader to the reviews of Lin & Papaloizou (1993), Lissauer (1993), Papaloizou & Lin (1995), Papaloizou & Terquem (2006), Armitage (2010), Chambers (2010), Kley & Nelson (2012) for a more comprehensive overview of planet formation.

Gas disk	
Surface density	$\Sigma = \Sigma_0 (R/1 \text{ AU})^{-p+1}$
Σ_0	1700 g cm^{-2}
p	2.75
Gas scale height	$H = H_0 (R/1 \text{ AU})^{-q+3/2}$
H_0	0.05 AU
q	0.5
Planetesimals	
Radius	R_p = 1-100 km
Density	$\rho_p \approx 3$ g cm^{-3}
Encounter regimes	$\{ v_{esc}, v_{weak}, v_{strong} \}$ ms^{-1}
1 km	{ 1.29, 3.5, 10 }
5 km	{ 6.47, 16.6, 54.2 }
10 km	{ 12.9, 33.1, 108 }

Table 1.1: Representative parameters for planetesimal accretion models.

1.2.1 Requirements for planetesimal accretion

This section focuses on the growth beyond km-sized planetesimals. Table (1.1) shows the relevant quantities in this stage. In this regime, bodies will primarily grow due to the combined action of planetesimal-planetesimal gravitational interaction, collisional encounters, and gas drag.

For purely head-on encounters, the geometrical cross section of a planetesimal is given by

$$\Gamma = \pi R_p^2 \tag{1.4}$$

However, at the km-sized scale, the gravitational attraction between bodies cannot be neglected, and the cross section is augmented by a gravitational focusing factor:

$$\Gamma = \pi R_p^2 \left(1 + \frac{v_{esc}^2}{\sigma^2} \right) \tag{1.5}$$

where v_{esc} is the escape velocity

$$v_{esc}^2 = \frac{2G(m_1 + m_2)}{R_{p,1} + R_{p,2}} \tag{1.6}$$

and σ is the local velocity dispersion of the planetesimals. The escape velocity represents a

critical speed in determining the balance between accretion, rebound, and disruption of planetesimals.

For a given collision at a speed dv (with velocity at infinity $v_\infty^2 = dv^2 - v_{esc}^2$), accretion can only happen when the rebounding velocity $v_{reb} = \epsilon dv$ (where $\epsilon < 1$ is the rebounding coefficient) is smaller than the escape velocity, i.e. $dv < v_{esc}/\epsilon$. Therefore, accretion requires $v_\infty \sim \sigma < v_{esc}$. When this condition is satisfied (i.e., as long as the velocity dispersion, which depends on the local mean planetesimal eccentricity and inclination, is not too large) a phase of *runaway accretion* occurs, such that $\dot{m}_p \propto m_p^{4/3}$ (Chambers 2010). This phase lasts approximately 10^5 years, during which larger planetesimals can become 50-100 times more massive than the swarm (Kokubo & Ida 2000). Once stirring from the gravitational interaction raises the velocity dispersion of the planetesimals, a phase of *oligarchic growth* ensues, where a few large embryos experience slower, orderly growth until they exhaust their feeding zones.

The onset and duration of runaway growth depends on the balance between excitation due to gravitational stirring (between planetesimals, or due to an external perturbation) and damping mechanisms (dynamical friction, inelastic collisions and aerodynamic gas drag). Assuming that $\sigma \approx e_P v_{kep}$, then we require that eccentricities are damped to small values (Kobayashi & Ida 2001)

$$e_P < \frac{v_{esc}}{v_K} \approx 0.001 \left(\frac{m}{10^{19}\mathrm{g}}\right)^{1/3} \left(\frac{\rho}{3\mathrm{g\ cm^{-3}}}\right)^{1/6} \left(\frac{a}{1\mathrm{AU}}\right)^{1/2} \left(\frac{\mathcal{M}_*}{\mathcal{M}_\odot}\right)^{-1/2} . \tag{1.7}$$

1.2.2 Gas drag

For km-sized objects, aerodynamic gas drag is still the dominant interaction with the gas disk (tidal torques become important at $10^{-4} - 10^{-2}\mathcal{M}_\oplus$). In the Stokes drag regime, the planetesimal suffers a torque due to the headwind of the gas:

$$\mathcal{T} = \pi C_D \frac{R_p^2 a_p \rho_g}{2 m_p} (\delta v)^2 \tag{1.8}$$

where $\delta v = v_p - v_g$ is the relative speed of the planetesimal to the gas (Weidenschilling 1977). For circular orbits, δv determined by the sub-Keplerian speed of the gas due to its pressure support, such that $\delta v \sim H_0^2 v_K \approx 2 \times 10^{-3} v_K$; in this regime, damping is very weak. When significant eccentricity and inclination develop, gas drag becomes important in damping the velocity dispersion. The relevant timescale is given by

$$t_{damp} = \mathcal{L}/\mathcal{T} \approx \frac{4}{3} C_D^{-1} \mathcal{M}_* \frac{\rho_p}{\rho_g} \frac{R_p}{a_p^{1/2}} (\delta v)^{-2} \tag{1.9}$$

where $\mathcal{L}$ is the angular momentum of the planetesimal, C_D is a coefficient of order unity and a_p is the orbital distance of the planetesimal. For $e_P \sim 10^{-3}$, $a = 1$ AU, $R_P = 10$ km, we find a timescale $t_{damp} \approx 10^6$ years, which is sufficient to damp stirring when planetesimals are small (Armitage 2010).

1.2.3 Erosive encounters

For encounter speeds approaching or larger than the escape velocity, the outcome of a planetesimal collision depends on the *specific energy*

$$Q = \frac{m_p v^2}{2 M_p} \tag{1.10}$$

where m_p and v_p are the mass and velocity of the smaller impactor and M_p is the mass of the massive target. The threshold Q^* at which a body shatters (but remains part of a larger fragment) as opposed to complete erosion (in which fragments disperse) is largely determined by a combination of experiments and numerical simulations.

Several estimates of the accretion/disruption limit exist (e.g. Thébault et al. 2006). Chapter §6 follows the prescription of Stewart & Leinhardt (2009) to classify encounters in two limiting regimes ("weak" materials and "strong" materials). A few representative collision speeds in the accreting and erosive regimes are shown in Table (1.1).

1.2.4 Planetesimal collisions in binary environments

The treatment of planetesimal accretion in the previous sections have assumed that planetesimal growth occurs in a single-star environment, where the velocity dispersion, and therefore impact speed, is expected to be low. However, external perturbations, such as those exerted by a stellar companion, can act to stir the planetesimals and increase eccentricities throughout the disk, raising the impact speeds past the threshold of erosive encounters.

For a binary system of mass ratio $\mu = \mathcal{M}_2/(\mathcal{M}_1+\mathcal{M}_2)$, separation a_B, and eccentricity e_B, the eccentricity of a planetesimal at a distance a will oscillate around the forced eccentricity (Marzari & Scholl 2000, Moriwaki & Nakagawa 2004):

$$e_f = \frac{5}{4} \frac{a}{a_B} \frac{e_B}{(1-e_B)^2} \tag{1.11}$$

when the binary is external to the planetesimal (circumstellar orbit), and

$$e_f = \frac{5}{4}(1-2\mu)\frac{a_B}{a} e_B \tag{1.12}$$

when the binary is inside the planetesimal's orbit (circumbinary orbit). N-body simulations where planetesimals are placed on initially low-eccentricity and inclination orbits followed the evolution of encounter speeds as a function of semi-major axis and planetesimal size (e.g. Marzari & Scholl 2000, Moriwaki & Nakagawa 2004, Thébault et al. 2004, Scholl et al. 2007, Thébault et al. 2006; see also Chapter §6). At the beginning of the simulation, eccentricities quickly increased beyond the critical value of Equation (1.7); however, orbits were strongly aligned and encounter velocities relatively low, far lower than expected if orbits were randomized; in that case, $dv \approx e_P v_K$. Subsequently, as the frequency of eccentricity oscillations increases and only weak phasing persists (Figure 6.2), planetesimals on crossing orbits start colliding at different phases, leading to high encounter velocities (Thébault et al. 2006). The presence of a gas disk only worsens the issue, as gas drag acts to phase planetesimals in a size-dependent fashion,

Code	Described in	
SYSTEMIC	§2	http://www.oklo.org
SPHIGA	§1.3.1	Available upon request
Disc-o-Mode	§5	Available upon request

Table 1.2: List of numerical codes used in this dissertation

leading to disruptive encounters between different-size planetesimals (Thébault et al. 2008).

This difficulty leads to a "planetesimal bottleneck" in the process of planet formation around binary stars (for a review of this issue, see Thebault 2011). Earlier stages are likely to be hampered by the binary of the system as well (e.g. grain formation and sticking; Nelson 2000, Zsom et al. 2011), although the literature on this topic is still incomplete. Somewhat reassuringly, if planetesimals were able to form and accrete, then later stages involving the build-up of cores from Moon-sized embryos are generally able to proceed rather undisturbed in almost the entire dynamically stable region (Quintana et al. 2002, Guedes et al. 2008). More sophisticated treatments typically exacerbate the issue (e.g. through additional perturbations from the gas disk), leading to the troubling conclusion that planet formation is hindered or altogether stopped for a large semi-major axis range around the stellar components. This becomes a paradox for planets such as HD196885-b, where ostensibly no region around the stellar primary is conducive to planet formation (Thebault 2011). Chapter §6 discusses this topic further in the context of circumbinary planet formation.

1.3 Numerical techniques

Table (1.2) lists a few of the numerical codes written to run the simulations described in this thesis. In the following section, we describe the SPHIGA code in detail.

1.3.1 SPHIGA: Numerical algorithm and tests

We perform the simulations described in §6 using a new *hybrid* code (SPHIGA). This class of codes are termed "hybrid" because they simultaneously integrate the motion of N_p test particles (the planetesimals) and N_* massive particles, and the hydrodynamical evolution of a protoplanetary disk. The planetesimals are evolved according to the gravity of the massive bodies (typically, a binary system) and the gas, and subject to aerodynamic drag, which is determined locally to the body. The full machinery for calculating the hydrodynamical evolution of the disk constitutes the bulk of the code, but can be turned off and substituted for a static gas background for computational convenience.

The code presented in this section models the hydrodynamical evolution of the disk using Smoothed Particle Hydrodynamics (SPH) method (Gingold & Monaghan (1977), Lucy (1977); see Monaghan (1992), Rosswog (2009), Price (2012) for recent reviews). While the general idea of local sampling of hydrodynamical quantities is common to all SPH formulations, in practice the details of the algorithm diverge significantly among the literature. In particular, the treatment of artificial viscosity, boundary corrections and time-stepping may produce quite different (oftentimes inaccurate) outcomes; this is especially true in the case of circumstellar disks, which are sensitive to the correct integration of shear flows. Our algorithm follows most closely the modern SPH formulations of Price (2004), Rosswog & Price (2007) and Lodato & Price (2010). SPHIGA implements a number of features (gas self-gravity in two and three dimensions, sink particles with corrected boundary conditions, accurate treatment of the adaptive smoothing length) which makes it better suited to follow the evolution of a circumstellar disk compared to other implementations. In the following sections, we briefly describe the numerical scheme and a few tests to verify its validity.

1.3.1.1 Hydrodynamics

SPH is a Lagrangian scheme for solving the equations of hydrodynamics . The evolution of the gas quantities is computed by integrating the equations of motion of N_g gas particles. SPHIGA employs the grad-h formalism of Rosswog & Price (2007), whereby the SPH equations are derived from a discretized Lagrangian, ensuring conservation of energy, linear and angular momentum. In this scheme, the momentum and internal energy (in absence of dissipation) equations for particle a take the form

$$\dot{\mathbf{v}}_a = \mathbf{g}_a - \sum_b m_b \left[\left(\frac{P_a}{\Omega_a \rho_a^2} \right) \nabla_a W(h_a) + \left(\frac{P_b}{\Omega_b \rho_b^2} \right) \nabla_a W(h_b) \right] \tag{1.13}$$

$$\dot{u}_a = \sum_b m_b \left(\frac{P_a}{\Omega_a \rho_a^2} \right) \left[(\mathbf{v}_a - \mathbf{v}_b) \cdot \nabla_a W(h_a) \right] \tag{1.14}$$

where $\mathbf{g}_a$ accounts for all non-hydrodynamical forces (e. g., gravity, indirect terms due to an accelerating frame), P_a and ρ_a are the pressure and density associated with the particle, respectively. The term Ω_a takes into account the spatial and temporal variation of the smoothing length h, and is defined as

$$\Omega_a = \left[1 - \frac{\partial h_a}{\partial \rho_a} \sum_b m_b \frac{\partial W(h_a)}{\partial h_a} \right] \tag{1.15}$$

In the SPHIGA code, the smoothing kernel W is set to the cubic B-spline (Monaghan 1992), which has a compact support; therefore, summations are restricted to neighborhoods of radius $2h$.

Finally, the density ρ and smoothing length h are computed simultaneously by iterating the equations

$$\rho_a = \sum_b m_b W(h_a) \tag{1.16}$$

$$h_a = \eta \left(\frac{m_a}{\rho_a} \right)^{1/\nu} \tag{1.17}$$

using the Brent method (Press et al. 1992) until sufficient accuracy is achieved. ν is the number of dimensions, and η sets the typical number of particles that will be involved in the interpolation. We use $\eta = 1.2$ for all our simulations; this ensures that at least ≈ 20 particles (in two dimensions) or ≈ 50 particles (in three dimensions) are used to approximate fluid quantities.

The code allows for several different equations of state (EOS), including an ideal gas law,

$$P = (\gamma - 1)\rho u \tag{1.18}$$

a locally isothermal EOS appropriate for disks with $c_s^2(R) = c_{s,0}R^{-p}$ (for $p = 1/2$ this corresponds to a disk with constant aspect ratio $h_D = c_{s,0}$), and a polytropic EOS where

$$P = K\rho^\gamma \tag{1.19}$$

The last two equations of state absolve the need to follow the energy equation.

We use the standard SPH artificial viscosity (Monaghan 1992) in all of our simulations to handle shocks and to avoid interparticle penetration. The artificial viscosity prescription adds two additional dissipation terms to the velocity and energy equations:

$$\dot{\mathbf{v}}_{a,diss} = -\sum_b m_b \Pi_{ab} \overline{\nabla_a W} \tag{1.20}$$

$$\dot{u}_{a,diss} = \frac{1}{2}\sum_b m_b \Pi_{ab} \mathbf{v}_{ab} \cdot \overline{\nabla_a W} \tag{1.21}$$

where $\overline{\nabla_a W} = 1/2\ [W(h_a) + W(h_b)]$. The artificial viscosity contributions are defined as

$$\mu_{ab} = \frac{\bar{h}\min\left[(\mathbf{v}_a - \mathbf{v}_b)\cdot(\mathbf{r}_a - \mathbf{r}_b), 0\right]}{r_{ab}^2 + \eta'^2\bar{h}^2} \tag{1.22}$$

$$\Pi_{ab} = \frac{-\bar{\alpha}\bar{c}_s\mu_{ab} + \bar{\beta}\mu_{ab}^2}{\bar{\rho}} \tag{1.23}$$

where barred quantities represent averages ($\bar{X} = [X_a + X_b]/2$), α and β are numerical coefficients that control bulk and shear viscosity, and $\eta' \approx 0.01$ avoids divergences when $r_{ab} \to 0$. Since most of our simulations involve shearing disks (where the artificial viscosity prescription would

be active at all times, even in absence of shocks), it is crucial to ensure that that artificial viscosity is minimized in the absence of shocks, while at the same time ensuring that shocks are resolved correctly. In our simulations, we follow the prescription of Morris & Monaghan (1997). The artificial viscosity coefficient α is evolved for each particle using an additional evolution equation

$$\dot{\alpha}_a = -\frac{\alpha_a - \alpha_{min}}{\tau_a} + \mathcal{S}_a \tag{1.24}$$

whereby the decay timescale $\tau_a = h_a/0.1c_{s,a}$ and the source function is $S_a = \max[-(\nabla \cdot \mathbf{v})_a, 0]$ restrict the growth of artificial viscosity to regions where compressional flows are present. We typically restrict the range of α between 0.05 and 1.5. Additionally, we use the "Balsara switch"

$$\alpha'_a = \alpha_a \frac{|\nabla \cdot \mathbf{v}_a|}{|\nabla \times \mathbf{v}_a| + |\nabla \cdot \mathbf{v}_a|} \tag{1.25}$$

(e.g., Balsara 1995, Lodato & Rice 2004) to further reduce the viscosity in pure shear flows. Although unneeded artificial viscosity cannot be completely eliminated, the use of time-dependent viscosity and the Balsara switch greatly reduced spurious viscous evolution of the disk.

Neighborhood lists are updated using the Barnes-Hut tree algorithm (Barnes & Hut 1986, Hernquist & Katz 1989). At each update of the particle positions, the tree is descended recursively. For each particle i for which the neighborhood list is being updated, the algorithm opens cells nodes that intersect with a cube of size of size $4h_i$ centered around the particle. Once a particle node is reached, the distance between the two particles is computed to check whether the particle lies within $2h_i$, and is added to an array of neighbors. For non-pathological particle distributions, neighbors are determined in $\mathrm{O}(N \log N)$ time.

Gravity is computed using one of the following two methods. When the self-gravity of the gas is neglected, a straightforward loop of all "star" particles accumulates the gravitational acceleration for each particle. We use the spline-softened form of the gravitational potential of Hernquist & Katz (1989) for a given softening length ϵ. If the self-gravity is computed, we reuse

the tree structure built to compute the neighborhood lists to additionally store center of mass and quadrupole moments for each node, and subsequently traverse the tree. The accuracy of the gravity calculation is controlled by the cell opening tolerance θ. Tree descents, SPH summations and gravity calculations are parallelized using OpenMP, where possible.

All units are normalized such that $G = 1$, $R = 1$ AU and the unit of mass is that of the central body. The unit of time is $P(R = 1)/2\pi$, the orbital period at a unit distance from the central star.

1.3.1.2 Planetesimal dynamics and collisions

Planetesimals are treated as test particles, interacting with the star particles through gravity and with the gas disk through gravity and gas drag:

$$\dot{\mathbf{v}}_a = \mathbf{g}_*(\mathbf{r}_a) + \mathbf{g}_{disk}(\mathbf{r}_a) + \mathbf{f}_{drag}(\mathbf{r}_a) \tag{1.26}$$

We approximate the aerodynamic drag force in the km-sized regime as (Weidenschilling 1977)

$$\mathbf{f}_{drag} = -K|\Delta\mathbf{v}|\Delta\mathbf{v} \tag{1.27}$$

where the drag coefficient K is given by

$$K = \frac{\pi C_d \rho_{gas} R_p^2}{2m_p} \tag{1.28}$$

and $\Delta\mathbf{v} = \mathbf{v}_p - \mathbf{v}_{gas}$. Physical radius R_p and mass m_p of the planetesimals are constant in the simulation (i.e., accretion or erosion outcomes following collision are neglected). We take $C_d \approx 0.4$, which is appropriate for spherical objects. In the case of two-dimensional simulations, we approximate the three-dimensional gas density using the local surface density and scale height ($\rho_{gas} \approx \Sigma_{gas}/\sqrt{2\pi}H$).

The gas drag force depends on the properties of the gas flow local to the planetesimal. We approximate these quantities using the SPH interpolation within a distance $2h_p$ to the

planetesimal, where h_p is varied in time to ensure that at least ≈ 20 gas particles (50 in three dimensions) participate in the interpolation. As in the previous section, neighbors are identified by traversing the tree structure.

The number of planetesimals that can be evolved in a computer simulation is bound by the sheer memory and CPU requirements for a realistic simulation. Therefore, we follow the standard inflated radius prescription (e.g., Marzari & Scholl 2000, Thébault et al. 2006; and others), whereby a small population of planetesimals ($N = 5 - 20 \times 10^3$) can yield a sufficient number of collisions to build encounter velocity statistics by setting the search radius to an inflated radius $\sim 10^{-4} - 10^{-5}$ AU. Again, we identify planetesimals for which $r_{ab} < R_{infl}$ during the SPH tree traversal, at a negligible computational overhead (compared to other simulations, e.g., Marzari & Scholl 2000).

1.3.1.3 Time integration

The code supports a number of different integration schemes, including embedded Runge-Kutta schemes (of order 2 and 3) and the drift-kick-drift (DKD) leapfrog. Time step is limited by the SPH Courant condition and the acceleration criterion (e.g., Hernquist & Katz 1989), which is

$$\Delta t_{f,a} = \tau_f \sqrt{h_a / |\dot{\mathbf{v}}_a|} \tag{1.29}$$

for gas particles, and

$$\Delta t_{f,a} = \tau'_f \min \left[\sqrt{r_{ab}/g_{ab}} \right] \tag{1.30}$$

for planetesimals (where the minimum is taken over all particles b accelerating the planetesimal a). We take $\tau_f = 0.5$ and $\tau'_f = 0.01$.

For the simulations presented in this section and Chapter §6, gas particles and planetesimals are evolved using the DKD leapfrog scheme. The leapfrog scheme presents a number

of advantages compared to the Runge-Kutta schemes: the symplectic nature of the algorithm conserves angular momentum, leading to a sufficiently accurate evolution of the semi-major axis and eccentricity of planetesimals. We verify that our time stepping algorithm is sufficiently accurate to model the evolution of the orbital elements of the planetesimals by running a reference N-body simulation comparing the leapfrog algorithm with the output of the Mercury code (Chambers & Migliorini 1997). The Mercury code used the RADAU integrator and default accuracy parameter. As a sample setup, we place 1,500 planetesimals in orbit around the A component of the α Centauri system (with orbital elements of the binary companion taken from Pourbaix et al. 2002). We ran both codes for 8×10^3 years.

Figure 1.5 shows the distribution of semi-major axes versus eccentricities and longitude of pericenter of the planetesimals. We note that the leapfrog algorithm appears to perform quite well as compared to RADAU, deviating somewhat only in the inner part of the planetesimal disk. This was expected, given that the low eccentricities ($e \lesssim 0.15$) involved in the simulation make low-order schemes suitable to evolve the planetesimal orbits. While higher order schemes would be preferable for maximal accuracy, the need to update and traverse the tree at each force evaluation of the planetesimals makes them presently unfeasible. Finally, we note that although the symplectic nature of the algorithm is formally lost due to the variable time step, in practice large time step changes are isolated and should not influence the overall orbital error significantly.

1.3.1.4 Boundary corrections

In gas simulations, we typically follow the evolution of the gas disk down to a minimum radius R_{in} from a sink particle representing the central star(s). However, it is easy to see that particles lying close to the boundary will spuriously accrete into the sink rather than maintaining pressure-supported Keplerian orbits. The reason for this is a particle bias highlighted by the

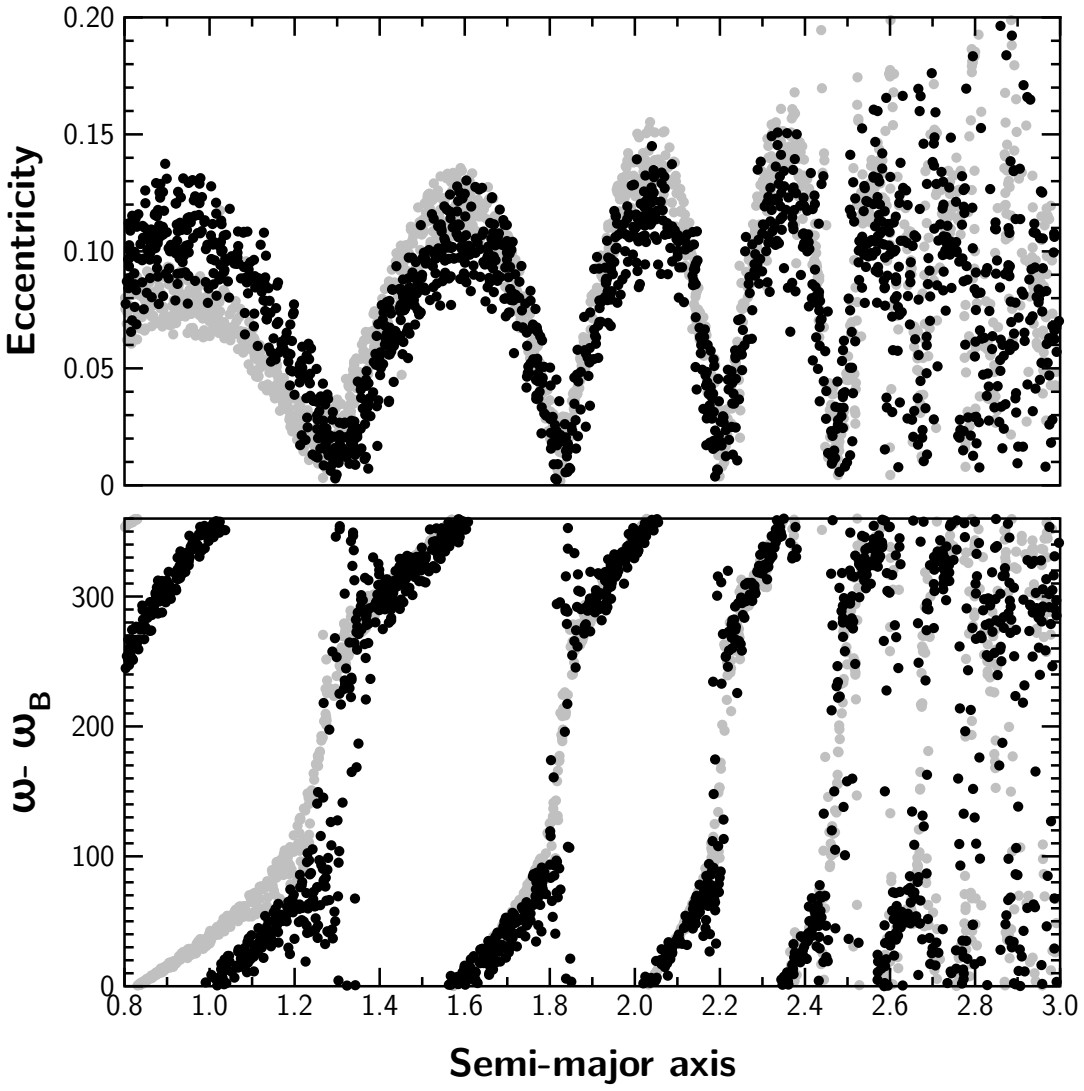

Figure 1.5: Snapshot at $t = 8 \times 10^3$ years of the eccentricity (*top panel*) and longitude of pericenter (*bottom panel*) of planetesimals evolved with the leapfrog integrator (black dots) and Mercury's RADAU (gray dots.).

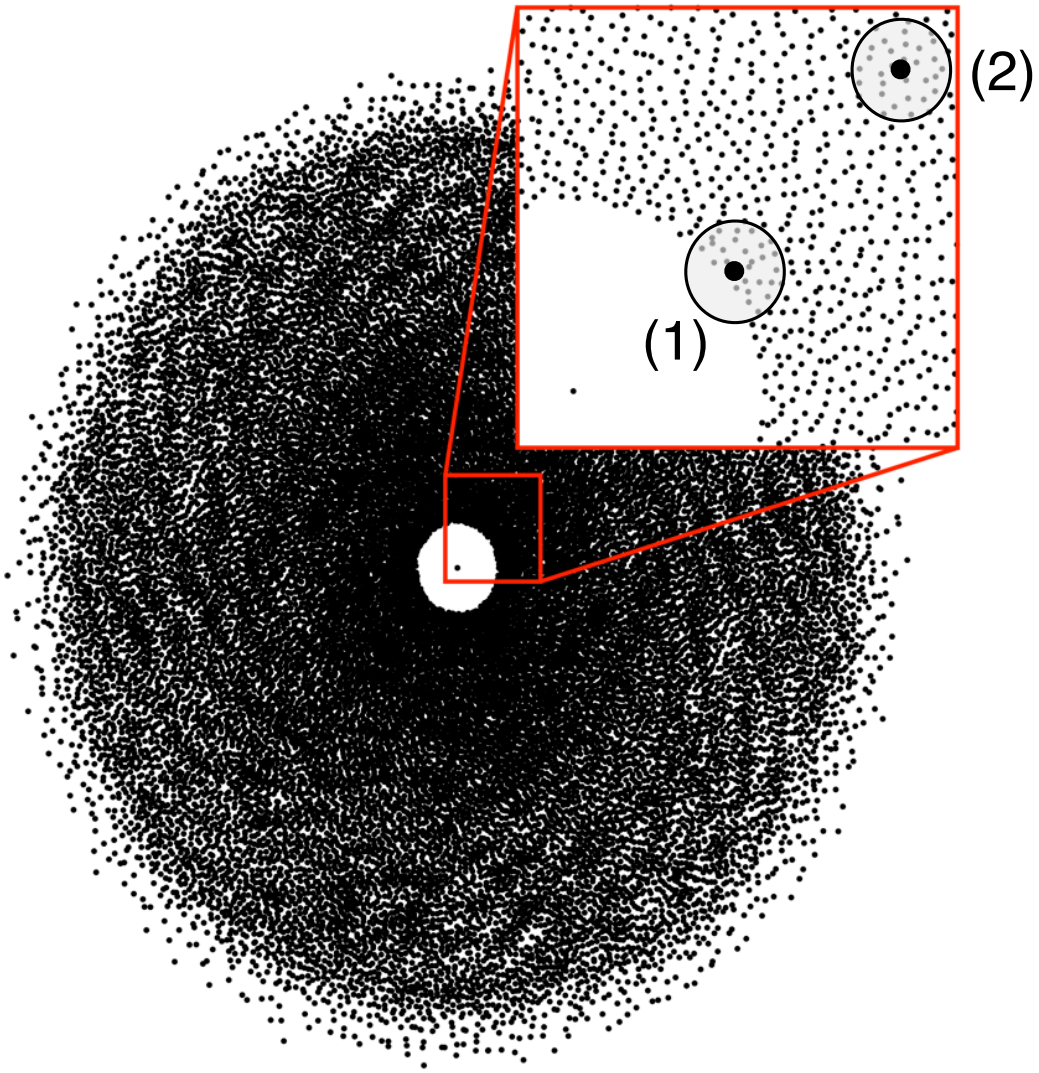

Figure 1.6: Sketch of the inner boundary of a SPH disk, with the neighborhood of two representative particles highlighted. Particles lying within $2h$ from the inner boundary (1) will feel a spurious inward pressure and viscosity gradient due to a lack of neighbors on the side of the sink particle, causing excessive accretion. Particle (2) will be unaffected initially, but will suffer the same spurious gradient once particles inside its orbital radius are accreted.

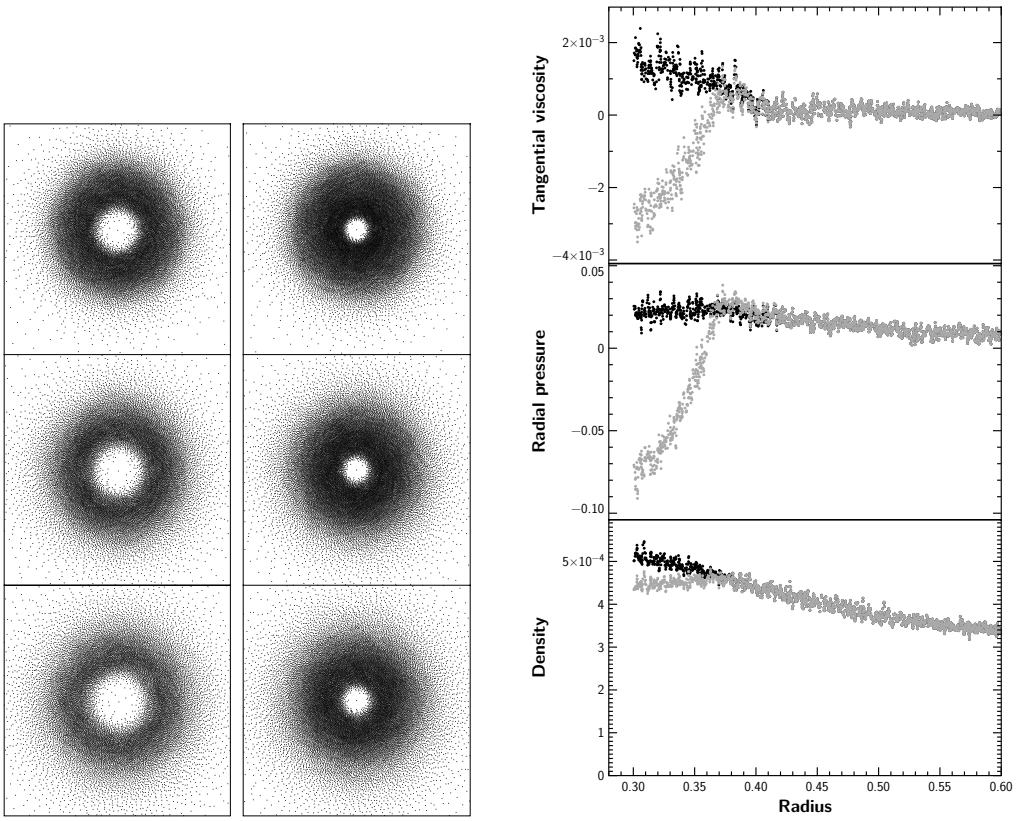

Figure 1.7: (*Left*) Evolution of a 25,000 particle disk without (left) and with (right) boundary corrections. (*Right*) Uncorrected (gray) and corrected (black) values of tangential viscosity, pressure and density for particles near the boundary of a SPH disk. Notice the large drop in pressure near the boundary.

sketch in Figure 1.6. Particles lying within $2h$ of the inner radius will lack pressure support on the side of the neighborhood facing the sink particle, and only particles away from the sink participate in the SPH summations; in effect, it is a "vacuum". This implies that there will be two spurious accelerations pushing the particle towards the sink: a positive pressure gradient (giving an inward radial acceleration) and a negative tangential viscosity, causing loss of angular momentum. The net effect is that accretion at the inner boundary cascades to particles at large distances, leading to an unrealistically high rate of accretion and the creation of a inner hole (Figure 1.7, left panel). The right panel of Figure 1.7 shows the uncorrected density, pressure and tangential viscosity profiles near the boundary of an SPH disk.

This numerical issue is due to the very nature of SPH summations, which rely on a smooth distribution of particles at the smoothing length scale. Such a spurious activity near the inner boundary can be seen in other SPH simulations of astrophysical disks (e.g Nelson et al. 1998, Lodato & Rice 2004). Grid-based codes, for example, avoid this problem by setting boundary values in ghost cells at the edge of the grid. For long-running simulations in which we are interested in a correct behavior of the gaseous disk, this poses an important obstacle. We adapted the procedure of Bate et al. (1995) to correct the hydrodynamical quantities at the boundary in the following manner.

Firstly, we evolve a disk extending all the way to an open inner boundary of $10^{-2}R_{in}$ for a few orbits of the outer edge, to suppress any remaining spurious noise. This procedure provides a snapshot at time $t = t_0$ where the density ρ, the pressure P and tangential viscosity force F_{visc} (hereafter collectively denoted with the generic letter A) at the inner boundary R_{in} are unaffected by the lack of particles towards the central star. We then select all the particles with $R_s < R_{in} + 4h_i$ from the sink. For each particle, we group neighbors on each side from the sink particle, and calculate their mean distance and $\bar{A}$, yielding a linear slope for the density, Ψ such that $A(R) = \Psi(R - R_s) + A_0$. We can then integrate the analytic equation for the

interpolated density to estimate the contribution from particles facing the sink (A_1) and away from the sink (A_2). In 3D, this is:

$$A_1 - A(R_s) = \int_0^{2h} \int_0^{\pi} \int_{-\pi/2}^{\pi/2} (\Psi R) W(r) \sin\phi \; r^2 \; dr d\phi d\theta = -2\pi F_3 \Psi \left(\frac{31h^4}{140} \right) = c_3 \ ,$$

while in 2D,

$$A_1 - A(R_s) = \int_0^{2h} \int_0^{\pi} (\Psi R) W(r) \; r dr d\theta = -2F_2 \Psi \left(\frac{h^3}{3} \right) = c_2$$

(where F_ν is the normalization of the kernel in ν dimensions; Monaghan 1992). Doing the same calculation for A_2 attains a linear relationship between A_2 (the correctly measured quantity) and A_1 (the quantity that needs to be corrected):

$$A_1 = A_2 \kappa_\nu, \quad \kappa_\nu = \frac{1 - c_\nu/A}{1 + c_\nu/A}$$

where A is the correct value. We then cut all particles within R_{in} and start the full simulation. At each timestep t_j, the correction κ_ν is calculated by using the previously corrected value $A(t_{j-1})$ (at the first timestep t_1, this is derived from the real gradient calculated at t_0). Finally, when appropriate (e.g., in circumstellar configurations), we slowly introduce the gravitational perturbation of the secondary companion by linearly ramping up the mass, such that the final mass is reached after four orbital periods.

This setup provides us with a framework for accounting missing neighbors self-consistently and recovering reasonable gradients at the boundary (Figure 1.7). Figure 1.8 shows the mass accreted by the central sink in presence of corrected boundaries, which is a fraction of the mass that would be accreted without corrections.

1.3.1.5 Initial conditions and set up

The typical set-up we are interested in involves a protoplanetary disk and planetesimals either in a circumstellar (CS; i.e., orbiting one of the binary components) or circumbinary

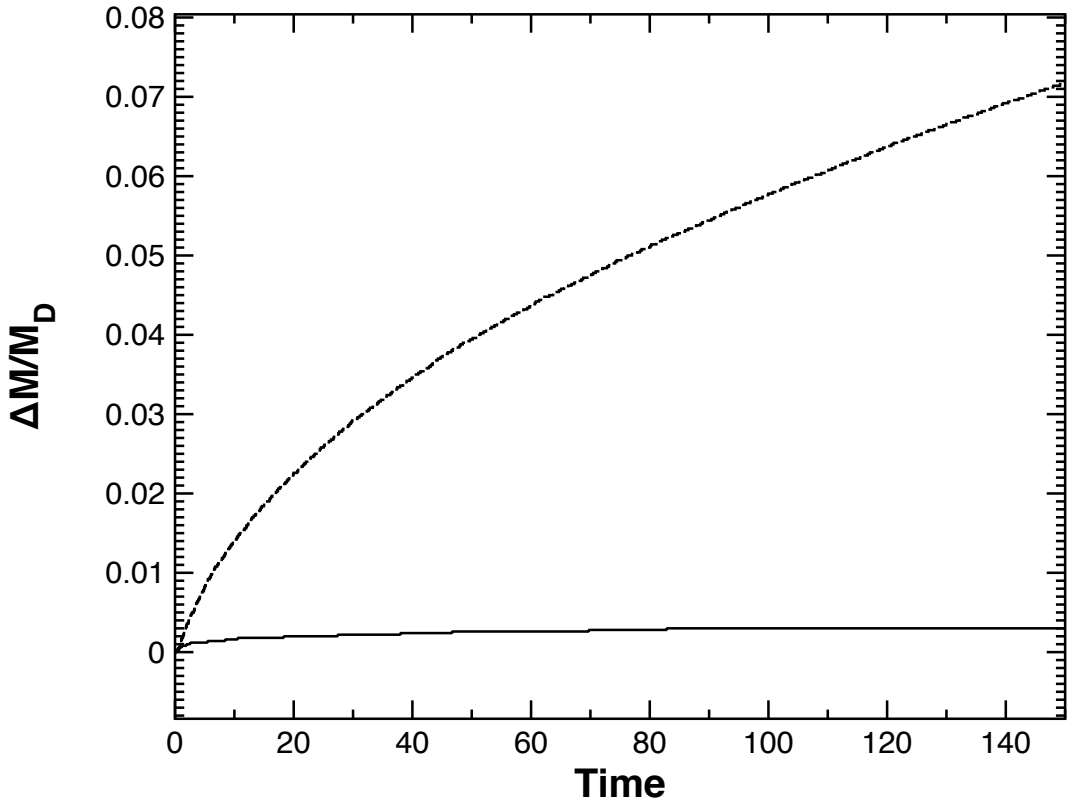

Figure 1.8: Mass accreted by the sink particle as a function of time, normalized by the mass of the disk, with uncorrected (dashed line) and corrected (solid line) boundaries.

(CB; i.e., orbiting around the barycenter of the central binary) configuration. The orbital parameters of the binary are fixed, and the instantaneous position and velocity vectors of the stellar components are determined by solving Kepler's equation (2.3.1).

When simulations are conducted in the non-inertial astrocentric frame of reference, an indirect term is added as an external force such that

$$\mathbf{g}' = \mathbf{g} - \frac{M_B}{B^3}\,\mathbf{B} \tag{1.31}$$

where $\mathbf{B}$ is the instantaneous position vector of the stellar companion.

The SPHIGA code is suited to conduct both pure N-body (gas-free or with a fixed gas drag term) simulations and simulations with an evolving circumprimary gas disk. In the latter case, the disk can be modeled as a two-dimensional, vertically averaged disk or a fully three-dimensional disk. The flow is initialized with zero radial and vertical velocity and sub-Keplerian tangential velocity, given by

$$v_\varphi = \sqrt{\frac{M_*}{R} - \frac{(\alpha + 2p)c_{s,0}^2}{\gamma R^{2p}}} \tag{1.32}$$

All gas simulations have to start from a "quiet" N-body realization, where gas particles are initialized on rings according to the prescribed surface density, at mutual distances such that $\delta R \approx \delta R\varphi$ (e.g., equal distance in radius and azimuth to the nearest neighbors). Although this configuration is quickly erased by SPH relaxation from local pressure and viscosity forces (Price 2012), it provides a less noisy start than a random rejection algorithm. Finally, for CS configurations, the mass of the companion is initially zero to aid in the relaxation of the disk.

1.3.1.6 Numerical tests

We briefly present some of the numerical tests we performed to verify the correct implementation of the SPH algorithm. In particular, we are concerned in the ability of the code

to resolve shocks without excessive dissipation.

Figure 1.9 shows a snapshot of a one-dimensional Sod shock tube (Sod 1978, Monaghan & Gingold 1983). The output of the SPHIGA code is compared with ATHENA, a grid-base hydrodynamical code (Stone et al. 2008). We find very good agreement between SPHIGA and ATHENA. A more stringent test, also shown in Figure 1.9, is represented by the Shu-Osher shock tube. In this case, the code has to accurately follow both a Mach = 3 shock and a small-scale smooth sine wave. Again, we find excellent agreement with the same test case run in ATHENA.

Following Murray (1996), we evolved an axisymmetric ring with a Gaussian surface density distribution

$$\Sigma(r, t = 0) = \exp\left[-\left(\frac{r - r_0}{l}\right)^2\right]$$

centered around $r_0 = 0.85$ and with a half-width of $l = 0.025$, orbiting around a central particle of unit mass. We used the standard SPH artificial viscosity, with a fixed $\alpha = 10$. This corresponds (in the continuum limit) to a kinematic viscosity term $\nu = (1/8)\alpha c_s h$. An approximate analytical solution for the evolution of the surface density for small t is given by

$$\Sigma(r, t) \approx \frac{1}{r^{3/4}\sqrt{12\pi\nu t}} \times \int_{r_1}^{r_2} \rho^{3/4} \exp\left[-\left(\frac{\rho - r_0}{l}\right)^2\right] \exp\left[-\frac{(\rho - r)^2}{12\nu t}\right] d\rho$$

(Murray 1996). This represents an excellent test of the correct implementation of SPH viscosity, as it can be compared to the analytical viscous evolution. The left panel of Figure 1.10 shows the output of a SPH simulation with 20,000 particles. The SPH ring density profile follows the analytic profile quite well, implying that the viscosity is implemented correctly. The right panel of Figure 1.10 shows the same simulation, but with the Balsara switch turned on. The use of the latter prescription effectively turns off viscosity in this purely shearing flow, even for the high value of α used.

Subsequently, we tested the three-dimensional, self-gravitating adiabatic collapse of an isothermal sphere to verify the correctness of the implementation of the energy equation, viscos-

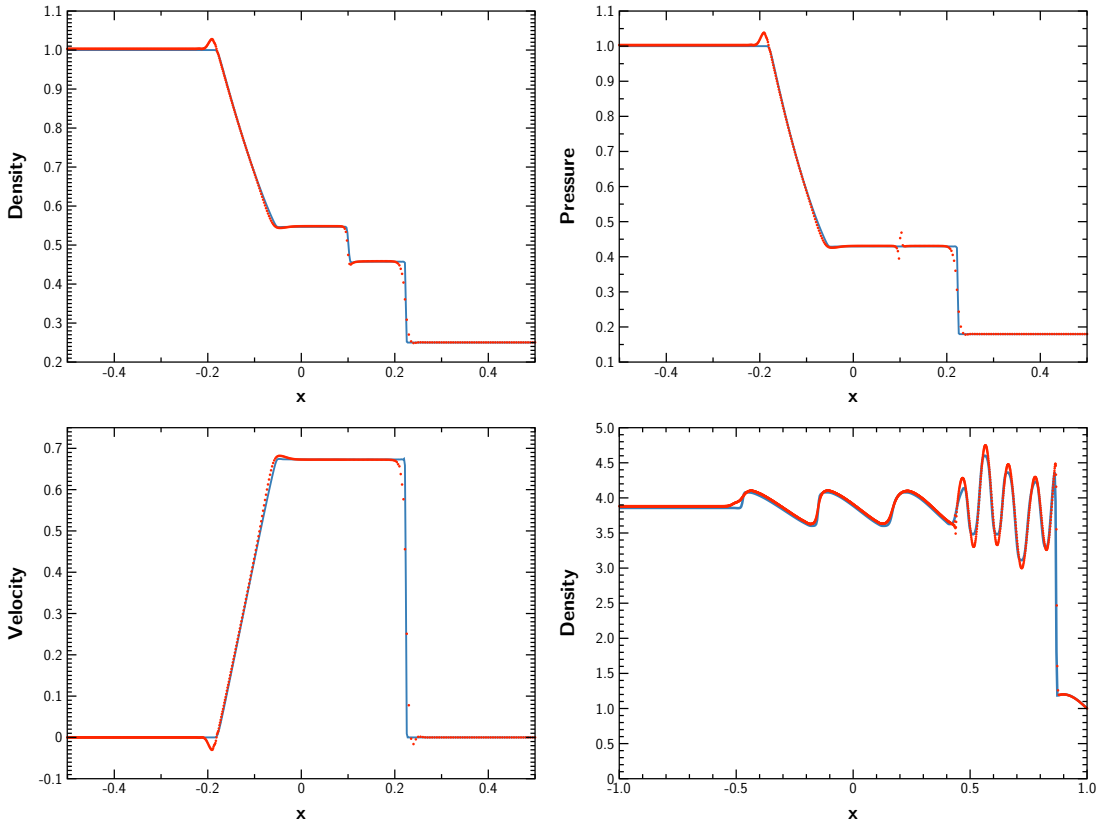

Figure 1.9: One-dimensional shocks as resolved by ATHENA (blue line) and the SPH code (red line). *Panels 1-3:* Density, pressure and velocity at t = 0.5 for the Sod shock test problem. *Panel 4:* Density at = 0.47 for the Shu-Osher shock problem.

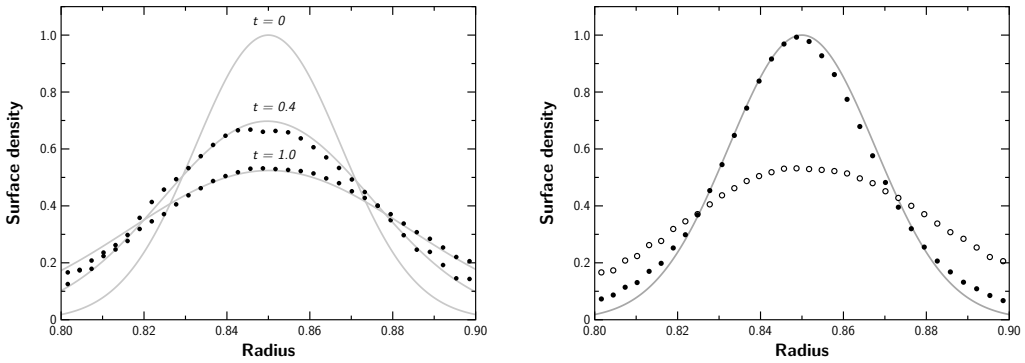

Figure 1.10: Viscous evolution of an axisymmetric Gaussian ring. *Left panel:* Surface density evolution at t = 0.4 and t = 1.0 for $\alpha = 10$ for a Gaussian ring in viscous equilibrium. Results from a 2D SPH simulation (black dots) are compared to analytical predictions of viscous spreading (gray lines). *Right panel:* The same simulation at t = 1.0, with the Balsara switch turned on and off (closed and open symbols, respectively) compared to the initial distribution. The gray line shows the initial density profile.

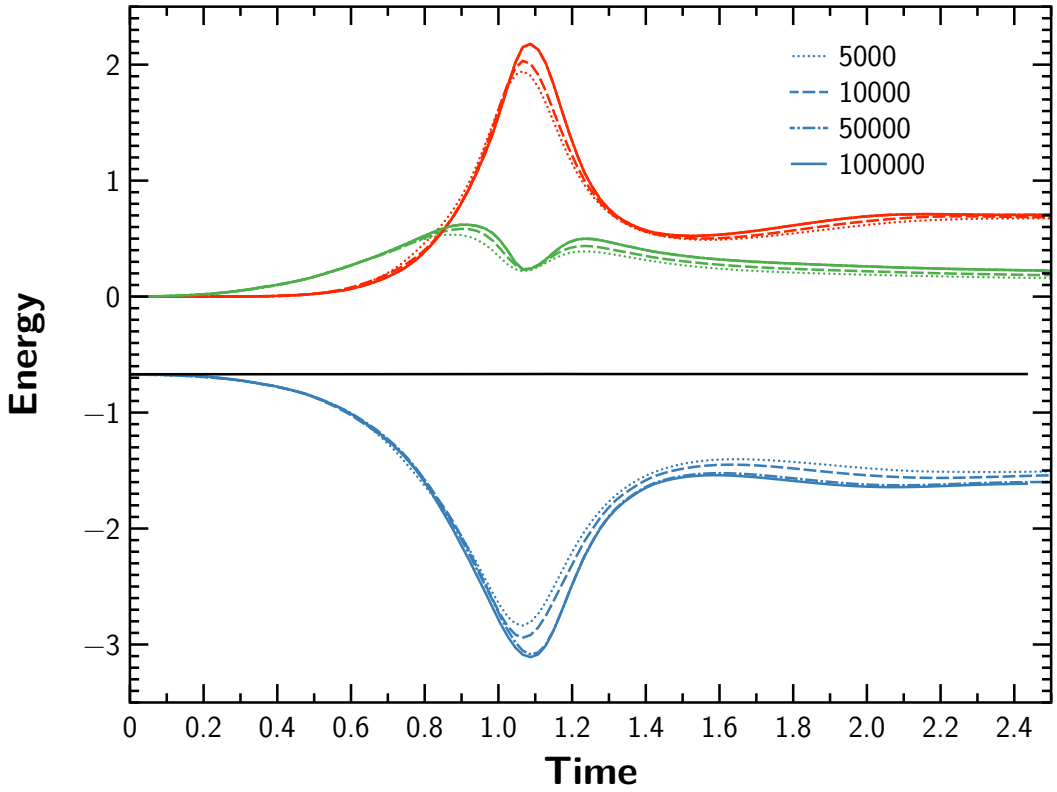

Figure 1.11: Thermal (red), kinetic (green), potential (blue) and total (black) energy during the collapse of an isothermal sphere.

ity and self-gravity. Figure 1.11 shows the energy evolution during the collapse of the isothermal sphere; we found that total energy during the rapid initial collapse is typically conserved to better than 2×10^{-3}. Our results are in agreement with the output of TREESPH (Hernquist & Katz 1989).

Our final test aims to verify the goodness of the SPH approximation in reconstructing the local gas drag acting on a planetesimal. Given the inherent small-scale noisiness of the SPH method, the local SPH summations used to compute the aerodynamic drag on the planetesimals could be construed as too coarse for the scope of this study. To assess this possibility, a benchmark simulation free from the gas flow disturbances imposed by the gravity of the secondary companion is set up as follows.

The system is set up with a binary with mass ratio $\mu = m_2/(m_1 + m_2) = 0.4$, semi-major axis $a_B = 30$ AU and eccentricity $e_B = 0.4$. We take a quiet SPH snapshot of the gas disk orbiting around the primary star, and fix the position of the gas particles relative to the primary. This fixed arrangement of particles could be viewed as a lattice of gas particles that the planetesimals travel through. Since the lattice still carries the properties of the gas flow (density and velocity vector) attached to each particle, it represents a SPH realization of a static gas background. To evaluate the quality of the SPH interpolation, we can therefore compare outputs computed with a pure N-body simulation including an analytic gas drag term (with the gas velocity given by Eqn. 1.3.1.5). We take a constant planetesimal radius of 5 km.

Figure 1.12 shows the orbital elements of 1500 planetesimals, distributed between 0.8 and 1.8 AU, at two stages in the simulation (4×10^3 and 8×10^3 years). Although the local SPH summation will yield a somewhat noisy interpolation of the local $\mathbf{\Delta v}$ (the difference between the planetesimal and local gas velocity, used to calculate the aerodynamic drag) and density, it does not appear to significantly affect the quality of the simulation, introducing only very small deviations in the orbital elements of the planetesimals throughout the duration of the

simulation.

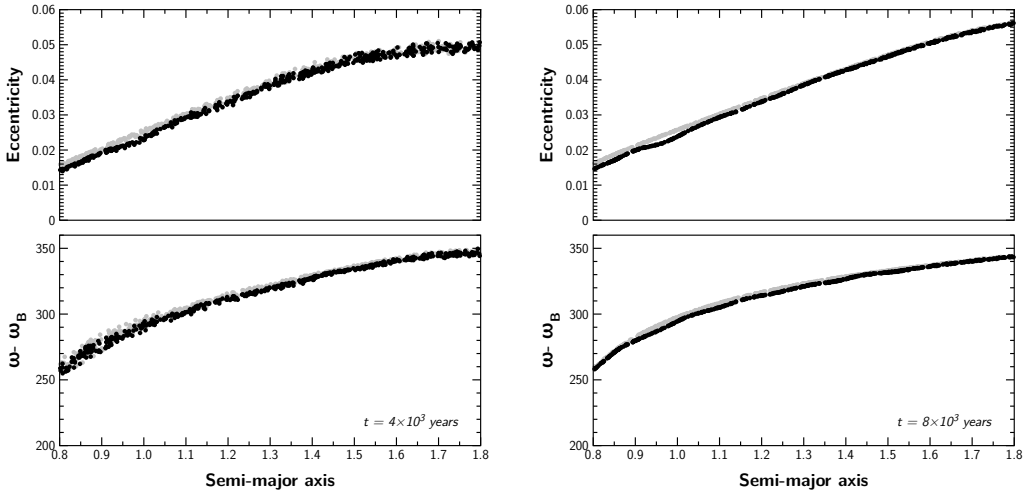

Figure 1.12: Snapshots comparing the eccentricity (*top panel*) and longitude of pericenter (*bottom panel*) of planetesimals evolved with the N-body code with analytic gas drag (grey dots) and the SPH method presented in this paper (black dots).

Chapter 2

Systemic: A Testbed for Characterizing the Detection of Extrasolar Planets

2.1 Abstract

We present the *systemic Console*, a new all-in-one, general-purpose software package for the analysis and combined multiparameter fitting of Doppler radial velocity (RV) and transit timing observations. We give an overview of the computational algorithms implemented in the Console, and describe the tools offered for streamlining the characterization of planetary systems. We illustrate the capabilities of the package by analyzing an updated radial velocity data set for the HD128311 planetary system. HD128311 harbors a pair of planets that appear to be participating in a 2:1 mean motion resonance. We show that the dynamical configuration cannot be fully determined from the current data. We find that if a planetary system like HD128311 is found to undergo transits, then self-consistent Newtonian fits to combined radial velocity data and a small number of timing measurements of transit midpoints can provide an immediate and vastly improved characterization of the planet's dynamical state.

2.2 Introduction

During the past decade, the characterization of extrasolar planets has become a major branch of Astronomy. The field is energized by a variety of ground and space-based detection programs that are meeting with increasing success. In 2009, the census of extrasolar planets has exceeded 300, and planets have now been successfully detected using a variety of techniques, including doppler radial velocity (e.g. Mayor & Queloz 1995, Udry et al. 2007), transit photometry (e.g. Henry et al. 2000, Charbonneau et al. 2000, Charbonneau et al. 2007), microlensing (Bennett 2008), astrometry (Benedict et al. 2002, Bean & Seifahrt 2009), stellar pulsations (Silvotti et al. 2007) and even direct imaging (Chauvin et al. 2005, Kalas et al. 2008, Marois et al. 2008).

The radial velocity method has been used to discover more than 75% of the known planets, and continues to be a dominant technique, both in terms of its continued productivity (e.g. Fischer et al. 2005) and its ability to accurately probe planetary architectures into the vicinity of the terrestrial mass region (e.g Rivera et al. 2005, Lovis et al. 2006, Udry et al. 2007, Mayor et al. 2009b). A number of planets that were initially detected using radial velocity (e.g. HD 209458b, HD 189733b, HD 149026b, Gl 436b, HD17156b and HD80606b) have been later shown to transit as a result of follow-up photometry, and because the parent stars of these planets are bright, follow-up characterizations with a variety of methods have been extremely valuable (e.g. Deming et al. 2005).

The planets that have been detected with the radial velocity technique comprise a complicated and non-uniform sample. Some systems such as Upsilon Andromedae (Butler et al. 1999; 2006), GJ 876 (Marcy et al. 1998; 2001, Rivera et al. 2005) and HD69830 (Lovis et al. 2006) have had multiple planets subject to very accurate orbital characterization within uniform, well-sampled data sets. Other systems, for example Epsilon Eridani (Benedict et al. 2006), draw their

support from a variety of observational sources and in some cases have orbital parameters that are significantly uncertain. Indeed, it is difficult to draw a firm boundary between detections that are secure, and those that may be subject to serious revision or even elimination.

In addition to the large amount of observational work that has gone into the detection of extrasolar planets, there is a parallel effort by theorists to explain the emerging distributions of planets within the context of theories of planetary formation and evolution. This work spans a wide variety of bases, but a unifying principle is that much of it depends on the raw data being supplied by the catalog of extrasolar planets, and therein lies a difficulty. Dynamicists have traditionally dealt with planetary orbital elements that are known to exquisite precision. As far back as the Eighteenth century, the orbital elements of the solar system planets were known with an accuracy well in excess of our current orbital determinations for extrasolar planets. Theoretical interpretations of the extrasolar planetary data is sometimes made without full account of the highly varying signal-to-noise of the datasets that make up the catalog. This problem is exacerbated by the fact that there exists no continuously up-to-date compendium of known extrasolar planets in which all of the fits are derived using the same toolset of routines. The systemic collaboration has been established as an effort to solve this problem.

The plan for this paper is as follows. In §2.3, we describe the systemic Console. In §2.5, we show some sample applications of the tools that are incorporated in the Console, with a particular emphasis on the planetary system orbiting HD128311 (Vogt et al. 2005). We show that our current radial velocity data set for this system is insufficient for characterizing the resonant relation between the planets, and we demonstrate, using synthetic datasets, how the inclusion of transit timing data (were transits to be detected) would almost immediately eliminate this degeneracy. As another example of the versatility of the code, we describe in Appendix 2.4 an automated pipeline (the systemic "backend") which runs on top of the same program to create a web application that analyses data sets and aggregates fits. In §2.6, we describe the direction

of possible future work with the tools that we have developed, and conclude.

2.3 The systemic Console

The *systemic Console* is a downloadable software package [1] that provides an intuitive graphical user interface for the fitting of planetary signatures, and an associated suite of dynamical analysis tools (Table 2.1). It can also be used as a specialized, programmable calculator and run scripts in non-interactive mode to access its library of numerical routines. The program is written in the *Java* programming language for cross-platform portability.

2.3.1 Radial Velocities

The systemic Console allows for a choice between two modeling schemes. For the majority of the known extrasolar planetary systems, the planets do not experience significant dynamical interactions during the time range spanned by a set of radial velocity observations. In these cases, the radial velocity variation of the star can be represented as a sum of N Keplerian orbits (Murray & Dermott 2000), each described by osculating orbital elements (period P, mass $\mathcal{M}$, eccentricity e, mean anomaly M, argument of periastron ϖ, inclination i and node Ω):

$$v_r(t) = \sum_{i=1}^{N} K_i[\cos(\upsilon_i + \varpi_i) + e_i \cos \varpi_i] \,, \tag{2.1}$$

where the radial velocity half-amplitude, K_i, of planet i is given by

$$K_i = \left(\frac{2\pi G}{P_i}\right)^{1/3} \frac{\mathcal{M}_i \sin i_i}{(\mathcal{M}_\star + \mathcal{M}_i)^{2/3}} \frac{1}{\sqrt{1-e_i^2}} \,, \tag{2.2}$$

and where the true anomaly, υ_i, is related to the eccentric anomaly, E_i, via

$$\tan\left[\frac{\upsilon_i}{2}\right] = \sqrt{\frac{1+e_i}{1-e_i}} \tan\left[\frac{E_i}{2}\right] . \tag{2.3}$$

[1] Freely available at http://www.oklo.org.

Fitting		
Levenberg-Marquardt	Edit → Polish	Multidimensional local optimization (2.3.3.2).
Simulated Annealing	Edit → Simulated Annealing	Multidimensional global optimization (2.3.3.3).
De-trend	Edit → Detrend	Removes linear trends from the radial velocity data.
Transit fitting	Options → Transit fitting	Adds transits to the χ^2 statistics.
Periodograms		
Lomb-Scargle Periodogram	View → Periodogram	Identifies periodicities in the full RV dataset and estimates FAPs.
Lomb-Scargle Periodogram of residuals	View → Periodogram of residuals	Identifies periodicities in the residual RV dataset and estimates FAPs.
Periodogram of sampling	View → Periodogram of sampling	Identifies spurious periodicity peaks associated with uneven sampling of the radial velocities.
Uncertainty estimation		
Bootstrap	View → Bootstrap	Estimates uncertainties using the bootstrap routine; plot and export marginal distributions of orbital parameters (2.3.4.1).
Markov Chain Monte Carlo	View → Markov Chain Monte Carlo	Estimates uncertainties using the MCMC routine; check chain convergence; plot and export marginal distributions of orbital parameters (2.3.4.2).
F-test	View → F-test / F-test significance	
Dynamical analysis		
Dynamical evolution	View → Orbital evolution and stability	Tracks the fully integrated evolution of the orbital elements and the stability of the system.
Transits prediction	View → Transits prediction	Calculates the distribution of central transit times for a given observational window.

Table 2.1: List of tools

The eccentric anomaly, E_i, in turn, can be expressed in terms of the mean anomaly $M_i = 2\pi/P_i(t - T_{\rm peri,i})$, which increases linearly in a clock-hand fashion, through Kepler's equation

$$M_i = E_i - e_i \sin E_i \tag{2.4}$$

Summed Keplerians provide an adequate model for nearly all of the planetary systems that have been discovered to date. Kepler's equation is rapidly solved using a simple iterative scheme, and hence models can be quickly evaluated (see e.g. Ford 2009; for a discussion of the current state-of-the-art).

There are, however, several exceptions, notably GJ 876 (Rivera et al. 2005), HD202206 (Correia et al. 2005) and HD60532 (Laskar & Correia 2009) in which a *self-consistent*, or Newtonian fit is required. In these cases, planetary interactions are taken into account in the fit, and the Console adopts an N-body model of the system

$$\frac{d^2\mathbf{x_i}}{dt^2} = -\sum_{j\neq i} \frac{G\mathcal{M}_j(\mathbf{x_i} - \mathbf{x_j})}{|\mathbf{x_i} - \mathbf{x_j}|^3}\,, \tag{2.5}$$

with the integrations carried out using either 4th/5th order Runge-Kutta with adaptive timestep control or Hermite 4th-order integration (Press et al. 1992, Hut et al. 1995). When an integrated model is adopted, a system is defined by the osculating orbital elements of the planets at the epoch of the first observation expressed in Jacobi coordinates (Lee & Peale 2002). The user also has the option of providing an integration routine.

Finally, the Console allows the velocity offsets between different data sources to be additional free parameters; this allows sources with different zero-point offsets (e.g. radial velocity surveys using different templates) to be combined in the fitting procedure.

The Console carries out parameter minimization of the so-called reduced chi-square

statistic

$$\chi^2_{red,RV} = \frac{1}{N_{RV} - M_{fit}} \sum_{i=1}^{N} \left[\frac{v_i - v(x_i\,;\, a_1 \ldots a_M)}{\sigma_i} \right]^2 \tag{2.6}$$

of a fit; in the above expression, N is the number of radial velocity data points, and M_{fit} is the number of activated parameters, $a_1 \ldots a_M$. As a rule of thumb, a reduced Chi-square value near unity is indicative of a "good" fit to the data, suggesting that the model is a reasonable explanation of the data within the observational errors. Typically, larger values usually signal an insufficient modeling of the data, whereas smaller values imply that the data has been over-fit. However, this rule is not exact, and should hence be applied with caution.

2.3.2 Transits

A rapidly growing number of planets (58 as of writing) with a favorably inclined orbital plane are being further characterized with transit timing data [2]. Transits enable direct estimations of planetary masses, radii and mean densities, together with period and phase of the transiting planet (Charbonneau et al. 2007). Considerable current interest is focused on detection of transit timing variations (TTVs) which can point to the presence of additional perturbing bodies in a given system.

When supplied to the Console, transits data (central primary and secondary transits timing) is included with the RV data in the following way. The Console searches for the best-fit orbital parameters by minimizing over the joint reduced χ^2 statistic

$$\chi^2_{red} = \frac{1}{N_{RV} + N_{tr} - M_{fit}} \left[\chi^2_{RV} + \chi^2_{tr} \right] \tag{2.7}$$

where χ^2_{RV} represents the goodness-of-fit for the radial velocity component of the model, as described above, and χ^2_{tr} is representative of the transit component. Ideally, one would fit together all of the radial velocity and transit photometry data with a single model to jointly

[2] Gary, B. 2009; http://brucegary.net/AXA/x.html, accessed 13 March 2009

invert for the parameters that describe all available data. In the future, these capabilities will be incorporated into the Console. Much progress can still be made, however, by restricting our analysis to observed times of central transit with error-bars obtained from separate light curve analyses. These transit time data can then act as separate constraints on the observed behavior of the system. To ease implementation, we compare the predicted and observed *location* of the planet at the observed time of central transit, rather than comparing transit times. Since the orbital velocities are not changing significantly with respect to the duration of the eclipse, the difference between these approaches is negligible. We thus use the following equation to define the goodness-of-fit statistic for the transit component of the model:

$$\chi^2_{tr} = \sum_{i=1}^{N} \left[\frac{\delta x_i}{\sigma_{\delta x,i}} \right]^2 \tag{2.8}$$

where δx_i is the predicted separation perpendicular to the line of sight at the observed central transits t_i, such that

$$\delta x_i = |x_*(t_i) - x_P(t_i)|, \quad i = 1..N \tag{2.9}$$

The error on δx_i is estimated from the error on t_i as $\sigma_{\delta x,i} = v_{x,P}\sigma_{t_i}$. While we do not explore it here, it is important to recognize that regularization of the fit may be warranted in this type of analysis (Press et al. 1992). [3]

Since it is routinely possible to achieve small error bars on the central primary transits (100s for ground-based observations down to 10s for HST observations), a best fit found by the Console that includes transit timing may yield extremely precise determinations of the period and mean anomaly at epoch of the transiting planet (e.g. Wittenmyer et al. 2005, Bean et al. 2008).

[3]Regularization is a formal statistical method of compromising between two distinct sources of information. This is accomplished by adding a relative weighting factor λ in front of one of the components of the overall χ^2 metric, where the value of λ determines the relative importance of the two components of the goodness-of-fit. There are many different methods that can be used to choose an appropriate value for the weighting factor. In this work, we have implicitly chosen the value $\lambda = 1$, corresponding to an equal weighting.

Detection of central secondary eclipses (Deming et al. 2007) also places tight bounds on the eccentricity and argument of periastron of the planet. This additional constraint can break degeneracies present when RVs alone are used; for instance, it can discriminate between eccentric single-planet systems and two-planet systems in a 2:1 resonance with circular orbits (Anglada-Escudé et al. 2010).

As we will address later, it can be possible to measure transit timing variations (TTV) in a dynamically interacting planetary configuration and infer the orbital elements of a perturbing, non-transiting body (Holman & Murray 2005, Agol et al. 2005, Agol & Steffen 2007).

2.3.3 Best-fit model estimation

2.3.3.1 Periodograms and False Alarm Probabilities

The Lomb-Scargle (LS) periodogram is an algorithm for time series analysis of unevenly spaced data (Scargle 1982, Horne & Baliunas 1986, Press et al. 1992). The LS periodogram is useful for rapidly identifying periodic signals in the observed data, and to residuals to a given fit, without having to fit for the other orbital parameters. The formula for an error-weighted periodogram $P_x(\omega)$ as implemented in the Console is given in Gilliland & Baliunas (1987); the individual weights are taken to be $w_j = 1/\sigma_j^2$.

An advantage of this method is that its statistical properties are well known and are conducive to the definition of an analytic *false alarm probability* (FAP) associated with each periodic signal. When the periodogram is normalized by the total variance $p_0(\omega) = P_x(\omega)/\sigma^2$, the estimated probability that a peak as high or higher would occur by chance is given by $\Pr(p_0, N_f) = 1 - [1 - \exp(-p_0)]^{N_f}$, where N_f is the effective number of frequencies.

Finally, since the unequal spacing of the data can be a source of spurious periodicities (e.g. those associated with the synodic lunar month or yearly observational schedules), the

Console also supports plotting of the power spectral window (Deeming 1975) overlaid over the standard (non-error weighted) periodogram.

2.3.3.2 Levenberg-Marquardt (local minimization)

Given the observations and associated errors, the goal is to obtain a model configuration $\mathbf{y}_{bf}$ (a $7N$ vector of orbital parameters) such that $\chi^2(\mathbf{y}_{bf}) = \min_y \chi^2$; this is usually reported as the "best-fit" solution. Typically, the Lomb-Scargle periodogram is used to comb through periodicities in the data; periodicities are removed in order of decreasing half-amplitude K and optimized using line-minimization. This procedure leads to a set of orbital parameters $\mathbf{y}_0$ which is a rough approximation to the best-fit solution, and can be improved with simultaneous multiparameter minimization. For a discussion of the intricacies of the Keplerian fitting process, see Cumming et al. (2008).

Multidimensional parameter minimization can be carried out using the Levenberg-Marquardt algorithm (LM; Press et al. 1992). Given the initial guess $\mathbf{y}_0$, the LM algorithm can quickly converge to a local minimum $\mathbf{y}'$. Good convergence of the LM algorithm is conditional on the choice of the initial guess and a favorable geometry of the $\chi^2(\mathbf{y})$ surface: in particular, the algorithm is sensitive to rugged χ^2 surfaces and can be prone to converging to non-optimal minima.

2.3.3.3 Simulated Annealing (global minimization)

So-called "global" minimization techniques attempt to avoid getting trapped in local minima by adding a degree of randomness at each iteration step, although at a much greater computational cost. Simulated annealing (SA; Press et al. 1992), by analogy to several thermodynamic processes in nature, defines an "energy" E as the objective function to minimize and allows for temperature fluctuations between states at different energies as dictated by the

current temperature T_n; the temperature T_n is lowered with a (problem-dependent) scheduler. This algorithm is particularly appropriate for rugged χ^2 surfaces, or when the initial guess is sufficiently distant from the best-fit solution.

In our problem, the objective function is clearly $\chi^2(\mathbf{y})$. Given a state $\mathbf{y}_n$, the algorithm selects a new configuration $\mathbf{y}_{n+1}$; the new configuration is accepted and kept with a probability $P(n \to n+1) \sim \exp(-\Delta E/T_n)$ if $E_{n+1} > E_n$, and is always accepted if $E_{n+1} < E_n$ (a downhill step). The temperature is subsequently updated according to the input scheduler, and the process is repeated until a target number of steps N is reached. The fact that uphill steps are *sometimes* accepted (according to the current temperature) lets the algorithm explore a larger portion of the parameter space and makes it less likely to get stuck in a narrow local minimum. The trial configuration $\mathbf{y}_n$+1 is selected using a *proposal distribution*, which is an easy-to-evaluate generator of trial configurations that picks a new set of parameters given the current set of parameters. The default function is a multivariate Gaussian distribution centered on the current step $\mathbf{y}_n$; the variance β_μ can be chosen independently for each parameter.

The algorithm requires that the following are configured from the user:

1. *temperature scheduler:* the default scheduler decreases T according to $T_n = T_0(1-n/N)^\alpha$, where T_0 and α are input parameters that dictate the initial temperature and cooling rate. The optimal values of T_0 and α are problem-dependent and quite often may determine whether the routine successfully recovers the true global minimum.

2. *generator of trial configurations:* the default generator is a Gaussian function centered around the current configuration, with the scale parameter vector β_μ given by the user (an initial value is suggested).

Since the correct recovery of $\mathbf{y}_{bf}$ depends on appropriate choices of T_0, α, N and β_μ that are not known a-priori, the Console allows several SA jobs to run in parallel, improving

the chance of convergence to the best-fit model. Reconfigurations, in the form of occasionally jump-starting the routine with the best-ever solution, can also be beneficial to the success of the algorithm.

Other global minimization schemes, such as Genetic Algorithms (e.g. Charbonneau 1995, Laughlin & Chambers 2001), are being considered for inclusion in the Console's built-in array of tools. They can be easily implemented by the user using the routine library offered by the Console.

Finally, we note that certain planetary systems such as HD80606 (Laughlin et al. 2009, Gillon 2009, Pont et al. 2009) include both photometric and spectroscopic data, and contain planets with high orbital eccentricities. In these cases, the connection between observable quantities and the orbital and physical parameters is highly nonlinear, and a modeling framework that relies purely on χ^2 minimization may have a difficult time recovering the correct system configuration. Future releases of the console will therefore incorporate the option of using a fully Bayesian approach to the fitting problem.

2.3.4 Error estimation

Radial-velocity searches are constantly pushing the envelope towards lower and lower masses, frequently at the threshold of detection, with low signal-to-noise ratios. For this reason, once the best-fit parameters have been identified, it is vital to rigorously characterize their uncertainty. The Console offers two independent methods for estimating uncertainty: synthetic datasets refitting (*bootstrap*) and Markov Chain Monte Carlo (MCMC).

2.3.4.1 Bootstrap

The bootstrap procedure consists of drawing with replacement from the observed data points (RV and central transits) and creating a number of synthetic data sets $A^S_{i=1..N}$. The

Levenberg-Marquardt fitting procedure is then applied to each dataset, using the best-fit solution for the real dataset as the initial guess. The distribution of the obtained fitted parameters $\mathbf{y}^S_{i=1..N}$ yield an estimated σ for the scatter of the orbital elements around the true intrinsic orbital parameters.

The bootstrap algorithm is well known (Press et al. 1992) and in common use for estimating planetary elements uncertainties, but presents a number of disadvantages; namely, that it drives a local minimization routine (and is thus subject to the same pitfalls), and that it has a large computational burden. To partially improve on the first weakness, bootstrap can optionally be preceded by a burn-in phase. The burn-in phase obtains a rough estimate of the scatter in the parameters by running a short bootstrap phase. The error estimate is then used in the actual bootstrap run to perturb the best fit a set number of times (e.g. 10 times) per each synthetic dataset fitting; only the best-fitting final configuration is retained. This helps improving the reliability of the bootstrap routine in some cases.

2.3.4.2 Markov Chain Monte Carlo

Markov Chain Monte Carlo (see, e.g., Ford 2005, Gregory 2005; for exoplanet related implementations) is an alternative method for estimating uncertainties that does not rely on minimization schemes. The MCMC method generates a sequence (*chain*) of configurations $\mathbf{y}_i$ that is sampled from the (unknown) probability distribution $f(\mathbf{y})$. The transition probability between two subsequent configurations $\mathbf{y}_n$ and $\mathbf{y}_{n+1}$ is

$$\alpha(\mathbf{y}_{n+1}|\mathbf{y}_n) = \min\left(\exp\left[\frac{\chi'^2_n - \chi'^2_{n+1}}{2}\right], 1\right) \tag{2.10}$$

Assuming that the observational errors are accurately estimated and approximately Gaussian, this transition function assures that, after discarding an initial burn-in phase, the distribution of generated configurations will be sampled from the unknown probability distribution f.

The algorithm consists of looping over the following steps, given an initial state $\mathbf{y}_0$:

1. given a state $\mathbf{y}_n$ and a Gaussian generator of trial states with scale parameters β_μ (see 2.3.3.3), generate a trial state $\mathbf{y}'$;

2. accept the trial state $\mathbf{y}'$ with a probability $\alpha(\mathbf{y}'|\mathbf{y}_n)$ and set $\mathbf{y}_{n+1} = \mathbf{y}'$, otherwise discard it (downhill steps are again always accepted);

3. set $n = n + 1$;

until some convergence criterion of the chain is satisfied. The MCMC algorithm guarantees convergence to the true distribution $f(\mathbf{y})$, but can explore the parameter space inefficiently depending on the choice of β_μ, or may not achieve satisfactory convergence within the chosen N steps. The convergence can be visually monitored by interactive plotting of the marginal distribution of the parameters. The acceptance rate of the MCMC algorithm can be interactively monitored as well; an optimal acceptance rate is ~ 0.25 (Gelman et al. 2003).

As with simulated annealing, multiple MCMC chains can be generated in parallel to provide comparison between the results obtained with different choices of β_μ and chain length, which yield similar results within statistical uncertainties if all chains have converged. More sophisticated Bayesian algorithms, such as parallel tempering MCMC (Gregory 2005), may be implemented by the user by exploiting the programmable interface of the Console.

2.4 The Systemic Backend

The *systemic backend* is a web application that showcases the power of the Console as an automated engine for data analysis. It consists of a database of catalog information (stellar properties as well as RV and transit measurements) as published in the astronomical literature, and a catalog of model planetary fits for each star. For this purpose, it uses the Console as

its main engine to perform a number of automatic data explorations, whereas the user-facing part uses standard "Web 2.0" tools (PHP, MySQL, Javascript and *wikis*) to present a coherent overview of the data. A public backend is available as a proof-of-concept to foster collaboration within the broader community of exoplanet researchers and enthusiasts, and to present and maintain the catalog of fits to radial velocity and transit timing data for known planet-bearing stars. Each user has a personal data page and fit catalog, the possibility of commenting on other team member's fits, and can interact with other team members within a private and secure environment. A more powerful and customizable version is also available on request for use by planet hunter teams, and can be useful to maintain an integrated database of datasets and models in face of the increasing flux of RV and transit data.

The fit catalog is scanned by a number of Console components, which continually sift through the uploaded fits in non-interactive mode. One component implements a bootstrap routine to calculate uncertainties on the orbital parameters of each fit; data from the bootstrap routine is stored in a database for creating scatter plots. Two other components check for dynamical instability over periods of 1,000 and 10,000 years, with stability defined by the rough criterion of requiring a smaller than 1% fractional change in semi-major axis with respect to the average semi-major axis observed during a full N-body integration. This step flags highly unstable planetary systems that experience ejections or collisions. Data from the integration is retained for plotting of orbital evolution and for future additional investigations. Dynamical data (orbital parameters, radial velocity data, fit parameters, stability, integrations, bootstrap results) is then transparently presented to the user as a set of web pages and can be aggregated and sliced using a web-based query system.

2.5 Applications

2.5.1 Resonance characterization in the HD128311 system

A high fraction of the detected extrasolar systems with multiple planet are involved in near low-order mean motion resonances (MMRs), with at least four of them (GJ876, HD82943, HD73526 and HD128311) being reported to engage in strong 2:1 resonances. Two planets are in a mean-motion resonance when the periods are in a ratio of small integers, and at least one of the resonant angles librates (i.e. it spans a range smaller than 2π). Resonant angles are linear combinations of ϖ (argument of periastron) and $\lambda = M + \varpi$ (coplanarity is assumed). The relevant resonant angles for a 2:1 resonance are $\theta_1 = 2\lambda_2 - \lambda_1 - \varpi_2$ and $\Delta\varpi = \varpi_2 - \varpi_1$ (Murray & Dermott 2000).

Radial velocity measurements for HD128311 (Vogt et al. 2005) (hereafter V05) indicated that the system is locked in a 2:1 MMR, which ensures the long-term stability of the two giant planets. The best-fitting model was indefinitely stable, with the resonant argument θ_1 librating with an half-amplitude of about 60 degrees; a naive fit using Keplerian ellipses instead of the full N-body model is catastrophically unstable within about 2,000 years. Orbital fits for the systems generated using a Monte Carlo procedure (similar to Section 2.3.4.1) yielded a proportion of about 60% stable systems with θ_1 librating and $\Delta\varpi$ circulating to about 40% with both arguments librating (*apsidal co-rotation*). The large stellar jitter ($\sim$ 9 m/s) and the relatively long periods of the two planets implies that models with different resonant configuration are equally likely given the radial velocity dataset.

However, whether or not the system is in apsidal co-rotation is a crucial piece of information, since it can provide fundamental clues to the migration and interaction history of the system. Scenarios of slow migration and resonant capture into a 2:1 MMR (e.g. Nelson & Papaloizou 2002, Lee & Peale 2002, Beaugé et al. 2006) consistently result in systems that

	Fit A	Fit B	Fit C
Period (d)	466.6 [7.5]	469.1 [3.3]	464.84
	909.5 [21.0]	893.5 [6.2]	901.63
Mass (M_J)	1.59 [0.22]	1.79 [0.17]	1.72
	3.19 [0.11]	3.19 [0.08]	3.13
Mean anomaly (deg)	270.6 [31.9]	282.2 [16.8]	263.10
	192.0 [23.3]	190.0 [13.7]	193.33
Eccentricity	0.36 [0.07]	0.33 [0.05]	0.32
	0.20 [0.09]	0.23 [0.05]	0.20
Long. of periastron (deg)	73.8 [24.8]	58.98 [19.6]	78.04
	11.7 [20.0]	4.54 [14.4]	6.59

Table 2.2: Orbital fit parameters. Fit A: integrated best-fit to the V05 Keck RV data. Fit B: integrated best-fit to the updated RV data reported in this paper and the HET09 data. Fit C: orbital elements used to generate the synthetic datasets. All elements are defined at epoch JD = 2450983.8269. Uncertainties are reported in brackets.

are librating in both resonant arguments. Sándor & Kley (2006), analyzing the specific case of HD128311, showed that after adiabatic migration and capture into MMR, the two planets are in apsidal co-rotation and have very small libration amplitudes. If a definitive prevalence of model fits *not* in apsidal co-rotation were ascertained, then the discrepancy has to be explained in terms of subsequent perturbative events (such as sudden termination of migration or planet-planet scattering) that happen after an adiabatic migration process. Analogous studies have been conducted for GJ876 (Kley et al. 2005) and HD73526 (Sándor et al. 2007).

It is therefore important to distinguish between the two resonant configurations (ideally, at the 90% confidence level or better); this requires a more precise determination of the orbital parameters, which might be achieved, for instance, with additional RV measurements.

For this purpose, we present a set of additional Doppler measurements taken between June 2005 and May 2008 using the HIRES spectrometer (Vogt et al. 1994). Doppler measurements are taken using the standard iodine cell technique (see Vogt et al. 1994; for more details). Table A.1 lists the updated Keck dataset, giving the time of each observation, the radial velocity and the internal uncertainties.

2.5.2 Best fit

We update the analysis of Vogt et al. (2005) using the tools built in the Console for both the original data and the updated RVs presented in this paper. The Console is well suited to this task, since it can easily derive self-consistent fits (interactively) and do batch Monte-Carlo dynamical analyses on large sets of orbital parameters (non-interactively).

The two prominent periodicities in the V05 dataset were found using the integrated Lomb-Scargle periodogram. A self-consistent (Newtonian) best-fit was then derived using the Levenberg-Marquardt minimization routine; one of the built-in N-body integrators (Hermite) was used to derive the radial velocity curve for each choice of orbital parameters. The final best-fit orbital parameters are listed as Fit A (Table 2.2). The uncertainties for each orbital parameter are found using the bootstrap routine on 10,000 synthetic dataset realizations.

Subsequently, we derived the best-fit for the full updated Keck data (Table A.1), together with the observations taken with the Hobby-Eberly Telescope (HET) and reported in Wittenmyer et al. (2009). The Lomb-Scargle periodogram and the associated analytic FAP estimates are shown in Figure 2.1. The Console can account for the zero-point offset and the velocity offset between the two datasets as two additional free parameters. The Newtonian best-fit orbital parameters derived, however, result in a system that is unstable within 1000 years. Therefore, we generated a pool of alternative 5000 bootstrap-generated trial fits, checked each of them for stability within 10000 years and selected the best-fitting stable solution. Its orbital parameters and corresponding uncertainties are listed as Fit B (Table 2.2). This model is protected by a 2:1 MMR, in which θ_1 librates with amplitude $\sim 60\,\mathrm{deg}$ and $\Delta\varpi$ circulates. The radial velocity measurements and the star radial velocity curve are shown in Figure 2.2.

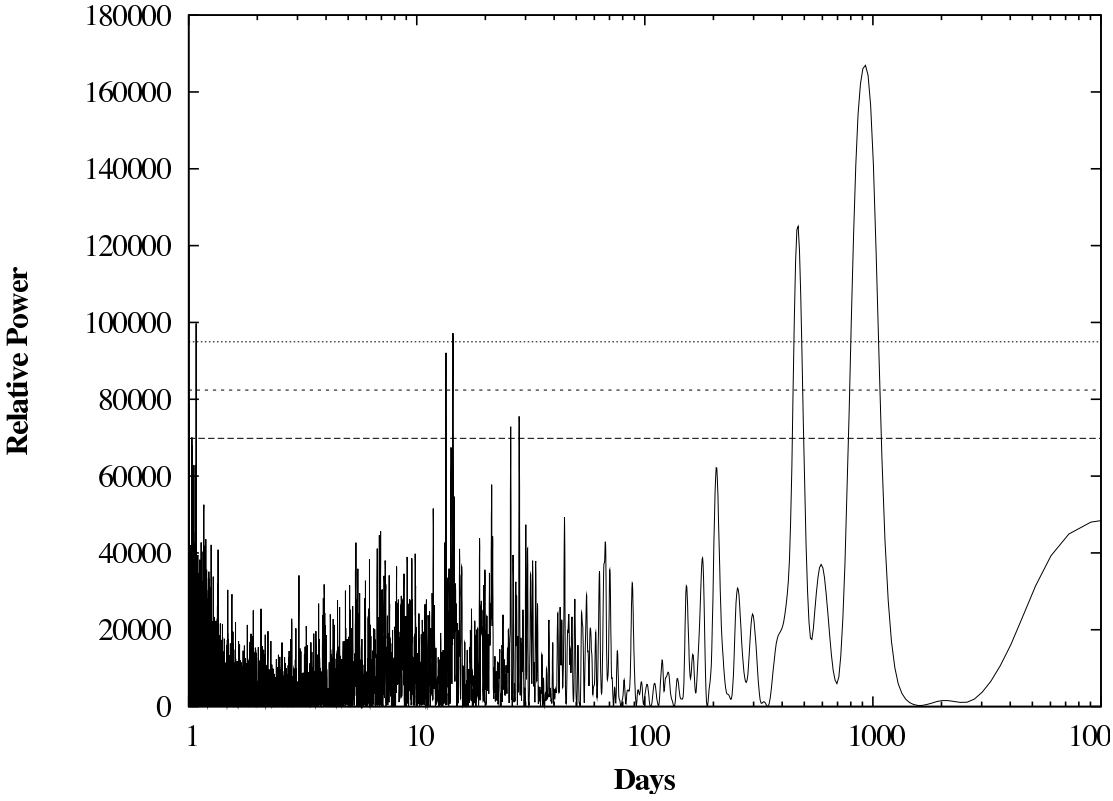

Figure 2.1: Lomb-Scargle periodogram for the combined Keck and HET datasets, as plotted by the Console. Analytical FAPs at levels 10^{-1} (long dashed), 10^{-2} (short dashed) and 10^{-3} (dotted) are overlaid.

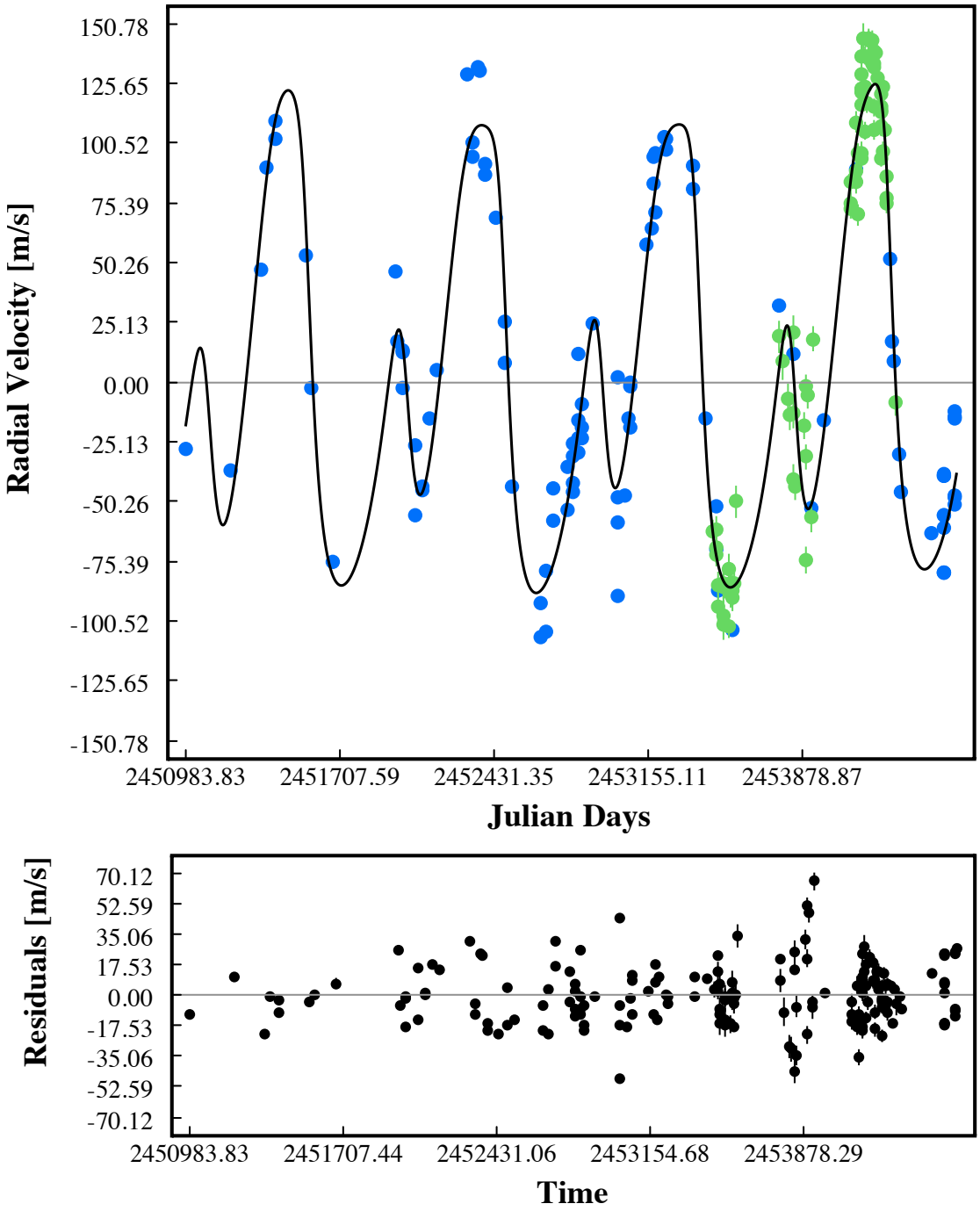

Figure 2.2: Best-fit integrated solution to the RV data presented in this paper (blue) and the HET data (green) reported by Wittenmyer (orbital parameters listed as Fit B in Table 2.2).

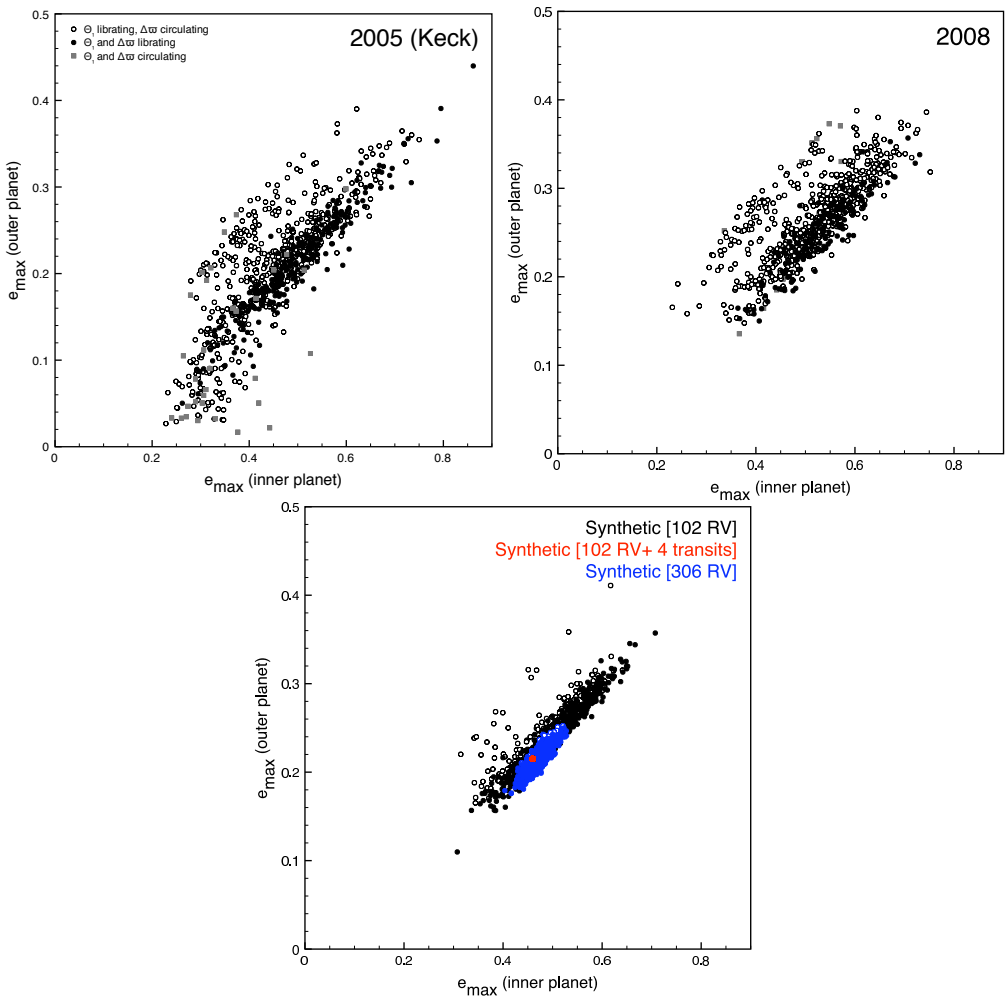

Figure 2.3: Maximum eccentricities observed during 10^4 yr integrations of self-consistent fits obtained using the bootstrap routine for data from V05 (*top*), data presented in this paper (*middle*) and synthetic data (*bottom*). Filled circles: scenarios in which both arguments librate. Open circles: scenarios in which θ_1 librates and $\Delta\varpi$ circulates. Gray squares: scenarios in which both arguments circulate. In the bottom panel, black and blue symbols are for models derived considering RV data only, whereas red symbols are for models considering RV and transits.

Data	R2	R1	NR
2005 (76 Keck RVs)	281 [35%]	489 [61%]	30
2008 (102 Keck RVs)	160 [20%]	618 [77%]	22
2008 (102 Keck + 78 HET RVs)	180 [22%]	615 [77%]	5
Fit C, 102 RVs	603 [75%]	197 [25%]	0
Fit C, 102 RVs + 4 transits	800 [100%]	0	0
Fit C, 306 RVs	743 [93%]	52 [7%]	5

Table 2.3: Monte-Carlo analysis results. R2: resonant fits with both arguments librating. R1: resonant fits with θ_1 librating and $\Delta\varpi$ circulating. NR: fits have both arguments circulating.

2.5.3 Dynamical interactions

Following the procedure detailed in Vogt et al. (2005), we took the two self-consistent two-planets fits (Fit A and Fit B) and applied a Monte-Carlo bootstrap procedure, in which new fits are derived by resampling with replacements the radial velocity datasets. We created two Monte-Carlo generated libraries of 5000 self-consistent models for two radial velocities datasets: the radial velocities listed in V05 and the updated Keck data reported in Table A.1. For each of the two groups, 800 fits, stable for at least 10^4 years[4], were selected and integrated forward, recording the maximum eccentricity for both planets and the amplitude of libration of both resonant angles. The results of this analysis are shown in Figure 2.3.

With the new radial velocity data, the percentage of model fits that are stable and in apsidal co-rotation using the additional RVs falls slightly to 20%. A different run considering 1600 models also yields a similar percentage, confirming that the result is robust. The inclusion of the HET data also does not change our result significantly (Table A.1). Therefore, while we have strengthened the case for models of HD128311 that only librate in θ_1, a secure determination of the libration amplitude of $\Delta\varpi$ might be obtained either by a transit monitoring campaign or yet additional RV measurements.

[4]For longer-term integrations, the builtin integration schemes (RK45 and 4th order Hermite) might not be sufficiently accurate and can be substituted by integration schemes supplied by the user. Alternatively, the Console can be set up to drive packages such as SWIFT [5]) or Mercury (Chambers & Migliorini 1997).

2.5.4 Constraints by transits

Although the a-priori geometric probability for transits P_{tr}

$$P_{tr} = 0.0045 \left(\frac{1\mathrm{AU}}{a}\right) \left(\frac{R_* + R_{pl}}{R_\odot}\right) \left[\frac{1 - e\cos(\frac{\pi}{2} - \varpi)}{1 - e^2}\right] \tag{2.11}$$

(Bodenheimer et al. 2003) is very low for HD128311b ($P_{tr} \approx 0.0032$), given the high precision that can be achieved by the addition of transits to the χ^2 budget, it is a worthwhile exercise as a proof of concept. Moreover, other resonant systems have higher transiting probabilities; for instance, planets GJ876b and c have a-priori transit probabilities $\sim 1\%$, though the inclination of the system is unfavorable and no transits have been observed (Shankland et al. 2006).

We selected the best-fitting solution in apsidal corotation from the ensemble of systems generated by Monte-Carlo bootstrapping of the RVs presented in Table A.1 (Fit C). The orbital elements are listed in Table 2.2. Subsequently, we created a synthetic dataset of RVs and transits by integrating forward in time, using the N-body routines offered by the Console. The RVs are generated by sampling the radial velocity curve at the times listed in Table A.1; the tabulated uncertainties and a jitter of 9 m/s are added to the measurement. The central transit times dataset comprises four points, to which we added a Gaussian noise with amplitude 10^{-4} d (comparable to the uncertainties that can be achieved by ground-based transit observations; e.g. Alonso et al. 2008).

We repeated the analysis detailed in the previous section by bootstrapping exclusively the RV data (Table 2.3); this yields similar ratios, shifted to favor systems in apsidal corotation (similarly to the generating fit).

As expected, the inclusion of the four central transit times largely reduces the parameter space that can be spanned by Monte-Carlo explorations. The large excursions in χ^2 and the increased ruggedness of the χ^2 space makes the simple bootstrap algorithm, driving a Levenberg-Marquardt scheme, somewhat inefficient in fully exploring the allowed space of or-

bital parameters (as anticipated in Section 2.3.4.1). We therefore used the Markov-Chain Monte Carlo routine supplied with the Console. A long chain of systems (5×10^5) was generated; the first 50000 systems were discarded and only 1 every 100 systems were retained, to minimize the correlation between subsequent chain elements.

The tightness of the orbital parameter uncertainties thus generated ($\Delta P_1/P_1 = 2.1 \times 10^{-6}$; $\Delta P_2/P_2 = 3 \times 10^{-6}$ d; $\Delta M_1/M_1 = 1.4 \times 10^{-3}$; $\Delta M_2/M_2 = 4.2 \times 10^{-4}$; $\Delta \varpi_1 = 2.4 \times 10^{-3}$; $\Delta \varpi_2 = 1.3 \times 10^{-3}$) anticipates that the ratio of correctly recovered resonant configuration will be very high. In fact, with the addition of the four primary transits, all of the systems are correctly identified in apsidal corotation (Table 2.3). The maximum eccentricities achieved by the two planets (Figure 2.3) are determined within 10^{-3}.

As a comparison, we ran the same procedure against 204 additional RVs (a 30-year observation stretch), derived by sampling the integrated stellar radial velocity with the same schedule used for the Keck dataset. This large amount of additional RVs is required to identify the generating planetary system as apsidally corotating with a fraction >90% of models (Table 2.3).

2.6 Discussion

In this paper, we have described the features of the systemic software package. This software has been written with extensibility, portability and clarity as guiding principles, and is fully adequate for all but the most demanding exoplanet-related analysis tasks. The Console provides a uniform method for analyzing data stemming from a variety of sources (radial velocities surveys and transits) and allows the efficient recovery of the best-fitting stable planetary configuration, even in presence of strong mutual perturbations. It is provided for free to the scientific community.

As an example application, we have analyzed an updated radial velocity dataset for the pair of resonating planets harbored by HD128311. As first noted in V05, the orbital solution to this system is degenerate between apsidally corotating and non-apsidally corotating fits; the additional data sets do not break the degeneracy, owing to the large stellar jitter and long orbital periods. We have used an analysis of synthetic data sets to demonstrate that the detection of a transiting extrasolar planet system with planets participating in a low-order mean motion resonance, such as HD128311, would lead to a rapid determination of the libration widths of the resonant arguments and an attendant understanding in how such systems form and evolve. Additionally, our analysis shows that the parameters of non-transiting planets can be very well constrained through transit timing variations in presence of strong mutual interactions. As noted in Section (2.3.2), however, a more detailed analysis may be warranted (in particular regarding the issues of fit regularization and full photometry fitting) and will be the object of a follow-up paper. Finally, we showed that breaking the degeneracy at a comparable level with radial velocities would require a prolonged observation campaign, of 30 years or more.

We plan to improve the current feature set of the Console by (1) adding facilities for fully fitting the raw light curve data of a transit detection, (2) implementing more sophisticated routines for best-fit parameter and uncertainty estimation, and (3) allowing non-coplanar, inclined fits. We note that to date, nearly all of the planetary systems that have been detected with the Doppler radial velocity technique can be satisfactorily modeled (to the precision of the observations) using co-planar models with the inclinations assumed to be 90°. The Console's integration routines and internal system representations are fully three-dimensional, however, and so a forthcoming version will enable non-coplanar fits and will accept astrometric measurements (e.g. Bean & Seifahrt 2009). With the advent of space missions such as SIM Lite and Gaia, there will be numerous opportunities to accurately discern the three-dimensional orbital configurations of many nearby planetary systems (Unwin et al. 2008). Finally, signatures of

less obvious effects in the spectroscopic and photometric data sets, such as those expected from general relativity (Wu & Goldreich 2002) or the excitation of tidal modes in the host star (Wu & Murray 2003), will require more sophisticated modelling to be properly taken into account.

Chapter 3

Numerical Approaches to the Transit Timing Inverse Problem

3.1 Abstract

Transit timing variations – deviations from strict periodicity between successive passages of a transiting planet – can be used to probe the structure and dynamics of multiple-planet systems. In this paper, we examine prospects for numerically solving the so-called inverse problem, the determination of the orbital elements of a perturbing body from the transit timing variations it induces. We assume that the planetary systems under examination have a limited number of Doppler velocity measurements, and show that a more extensive radial velocity characterization with precision comparable to the semiamplitude of the perturber may remove degeneracies in the solution. We examine several configurations of interest, including (1) a prototypical non-resonant system, modeled after HD40307 b and c, which contains multiple super-Earth mass planets, (2) a hypothetical system containing a transiting giant planet with a terrestrial-mass companion trapped in low-order mean motion resonance, and (3) the HAT-P-13

system, in which forced precession by an outer perturbing body that is well characterized by Doppler radial velocity measurements can give insight into the interior structure of a perturbing planet, and for which the determination of mutual inclination between the transiting planet and its perturber is a key issue.

3.2 Introduction

While the overall census of extrasolar planets continues to climb steadily (453 as of this writing[1]), the emerging population of Earth and Super-Earth sized ($\mathcal{M} \sin i \leq 10 \mathcal{M}_{\oplus}$) planetary companions that has been uncovered by high-precision radial velocity (RV) surveys (e.g. Rivera et al. 2005, Udry et al. 2007, Mayor et al. 2009a, Vogt et al. 2010) is shifting the interest of many planet search programs towards terrestrial planets. Future refinements in ground-based RV programs will likely continue to further push the detection capabilities towards the low-mass end of the planetary population (Mayor et al. 2009b, Howard et al. 2011).

On the other hand, the availability of ground and space-based surveys dedicated to photometric monitoring of large samples of host stars is affording constraints on the true mass and bulk composition of the Super-Earth planetary population (Léger et al. 2009, Queloz et al. 2009, Charbonneau et al. 2009). In particular, the *Kepler* mission (e.g. Koch et al. 2004, Koch et al. 2010) is expected to yield transiting Earth-mass planets in the Habitable Zone (HZ) as part of its mission objectives, through continuous and simultaneous photometric sampling of more than 100,000 dwarf stars. However, this class of objects will likely represent a small percentage of the detections (given the constraints of the mission design), and a large number of Neptune-mass and giant planets will be detected as well (e.g. Borucki et al. 2010a;b).

The exquisite precision and sheer size of the *Kepler* transit timing datasets of giant

[1] exoplanet.eu, retrieved on May 12, 2010

planets, as observed during the projected four years to six year mission duration, opens up an alternative route to the detection of low-mass planetary companions. Indeed, transit timing variations (TTV) will be caused by gravitational perturbations exerted by additional planets, causing deviations from strictly periodic Keplerian orbits (Miralda-Escudé 2002, Holman & Murray 2005). These can be used to infer the orbital elements of the perturbing planet (Agol et al. 2005), or at least place limits on the presence of additional planets (e.g. Alonso et al. 2008, Miller-Ricci et al. 2008). An approximate analytic estimate for TTV amplitude for a transiting planet and an external perturber is given by (Holman & Murray 2005)

$$\delta t \approx \frac{45\pi}{16} \left(\frac{\mathcal{M}_{pert}}{\mathcal{M}_*} \right) P_{trans} \, \alpha_e^3 \left(1 - \sqrt{2}\alpha_e^{3/2} \right)^{-2} \tag{3.1}$$

(where we use the symbols $\mathcal{M}$ for mass, P for period, e for eccentricity and a for semi-major axis; $\alpha_e = a_{trans}/\left[a_{pert}(1 - e_{pert})\right]$).

The amplitude of these variations can be quite large and amenable to detection, either in the presence of high-eccentricity perturbers (e.g. Steffen & Agol 2005) or when the two planets lie near a low-order mean motion resonance (MMR). Indeed, MMRs are an entirely plausible outcome of core-accretion models of planetary formation, whereby planets can be captured and locked into an MMR during the migration stage (e.g. Nelson & Papaloizou 2002, Papaloizou & Szuszkiewicz 2005, Beaugé et al. 2006). Observationally, several of the detected extrasolar systems with multiple planets may be locked in low-order MMRs. Three such systems (HD82943, HD73526 and HD128311) are engaging in deep 2:1 resonances well characterized by the observations, and GJ876 has recently been reported as a Laplace-type resonance chain (4:2:1; Rivera et al. 2010). For instance, the TTV amplitude induced by an Earth-mass perturber in a 2:1 resonance with a 3-day Jupiter-mass planet, both in circular orbits, is of order of minutes (Agol et al. 2005). This is a large signal compared to an accuracy in the measurement of the

central transit time of order (Ford & Gaudi 2006)

$$\sigma_T \approx \left(\frac{t_e}{2\Gamma}\right)^{1/2} \sigma_{ph} \left(\frac{R_{pl}}{R_*}\right)^{-2} \tag{3.2}$$

(where t_e is the duration of the transit ingress/egress, Γ is the observation rate, σ_{ph} is the photometric precision, R_{pl} and R_* are the radius of the planet and the radius of the star, respectively), amounting to 10s of seconds for milli-mag photometric accuracy. The recently published *Kepler* central times (Latham et al. 2010, Borucki et al. 2010b, Jenkins et al. 2010, Dunham et al. 2010, Koch et al. 2010) are in rough accordance with this estimate. Furthermore, with respect to the *Kepler* project, we note that once a transit is detected with sufficient signal-to-noise ratio, the star will be switched from the long-cadence (30 minute) to short-cadence (1 minute) sampling rate (Borucki et al. 2008), improving the temporal resolution of the transit even further. We take $\sigma_{tr,K} = 2 \times 10^{-4}$ d ($\approx$ 15 s) as a conservative estimate of accuracy on the central transits.

Given a large dataset comprising 1 year or more of continuous transit monitoring, is it possible to infer the mass and elements of the perturbing planet? Reconstructing the properties of the perturber from a noisy TTV signal is a complex, and possibly highly degenerate (Nesvorný & Morbidelli 2008), inverse problem. In this paper, we present a series of simulations aimed at detecting low-mass perturbers from realistic central transit and follow-up RV data. To this end, we produce a large sample of *Kepler*-like observations and attempt to characterize the perturber using the algorithm toolset offered by a revised version of the Systemic Console (Meschiari et al. 2009; hereafter Paper I). A number of different planetary realizations were used, in an attempt to fully capture the complexity of TTV fitting, drawing the orbital elements from observed planetary systems. For the sake of simplicity, we focus on two-planet systems, but the method is fully general within the constraints of CPU time and measurement errors.

The plan of the paper is as follows. In §3.3, we briefly review describe the algorithms

used to derive best-fit models and accompanying error estimates. In §3.4, we examine the characterization of planets similar to HD40307c and d, which lie close but not quite in a 2:1 MMR. Our analysis makes use of the HARPS dataset (Mayor et al. 2009a) and a simulated transit timing dataset. In §3.5 we fit the synthetic realization of a planetary system deep in a 2:1 MMR, with an external perturber (using HAT-P-7 as our model system). Finally, in §3.6 we analyze constraints placed by TTVs on the three-dimensional configuration of planetary systems, using HAT-P-13 as a test case, and conclude in §3.7.

3.3 Numerical setup

The transit timing variation signal is defined as the difference between the observed central transit times and the predicted times from a linear regression (corresponding to a single-planet Keplerian fit with period P_1):

$$\delta t_k = t_k - kP_1 \tag{3.3}$$

The variations originate by the mutual gravitational interactions with an additional body, chiefly causing short-term oscillations wherein the true anomaly f_1 trails or leads the Keplerian value and long-term effects such as pericenter precession (Heyl & Gladman 2007). In principle, since the signal will depend on the Newtonian evolution of the planetary system, TTVs can provide a sensitive probe for the three-dimensional orbit of the second planet, in combination with the tight constraints on the eclipsing planet's period and the time of pericenter passage provided by the central transits themselves.

However, solving the inverse problem of deriving a best-model fit to the TTV observations can be daunting. The computation of the predicted TTV signal requires precise N-body integrations (with $N \geq 3$). In the general case, the dependence of the signal on the set of orbital parameters is not directly clear; unlike, e.g. the RV technique, deviations from the Keplerian

signal – as opposed to the Keplerian signal itself – constitute the bulk of the information. The use of Fourier analysis to sort out periodicities in the data is generally hampered by the sparseness of the transit observations. Furthermore, given the extreme sensitivity of δt to the model parameters, local minimization routines can easily get stuck in narrow χ^2 minima, or fail due to steep gradients in the landscape. Finally, as shown in the later sections, there is a degree of non-uniqueness as multiple models can fit the transit timing observations when measurement errors are taken into account (see also e.g. Nesvorný & Morbidelli 2008); these degenerate solutions are characterized by comparable $\chi^2 \sim 1$, and must be taken into account when deriving parameter uncertainties.

Direct searches of the parameter space (e.g. Steffen & Agol 2007) can be extremely expensive in terms of CPU time. A more appealing alternative is represented by the TTV Inversion Method (TTVIM; Nesvorný & Beaugé 2010; and related papers). TTVIM combines a fast algorithm for computing the 2-planet transit timing based on perturbation methods with a downhill simplex method to obtain good convergence towards the perturbing planet's parameters. However, some issues remain in addressing systems lying close to a MMR.

In this paper, we adopt the approach of finding best-fit models to joint TTV and Doppler velocity data sets by driving an efficient Bulirsch-Stoer integrator with the Simulated Annealing algorithm integrated in the Systemic Console (Paper I)[2]. SA-type algorithms are well-suited to exploring the orbital parameter space (period P, mass $\mathcal{M}$, eccentricity e, inclination i, mean anomaly at epoch M_0, longitude of pericenter ϖ and node Ω for each planet) and converging, in principle, to global minima (subject to appropriate choices of scheduling algorithm and scale parameters). Several minimizers can be run in parallel with different initial temperatures and initial conditions, exploiting modern multi-core CPUs capabilities. The step size vector is

[2]The new version of the Systemic Console, including a Bulirsch-Stoer integrator, AMOEBA and fully non-coplanar fitting is available for download at www.oklo.org

automatically adjusted to attain an acceptance rate of $\sim 25\%$; we have found empirically that this value is an optimal compromise. After a fixed number of steps, we invoke a downhill simplex algorithm (AMOEBA; Press et al. 1992) in an attempt to home in on nearby deep minima. This avoids missing promising solutions when the SA step size is too large to properly resolve them. In practice, this scheme permits the derivation of the full set of degenerate solutions compatible with the observational errors.

Although we recognize that this approach can be computationally inefficient compared to perturbation methods, the implementation is trivial and can use existing integration techniques. Furthermore, it permits the characterization of arbitrary planetary configurations (including $N_{pl} > 2$, resonant, high-eccentricity and inclined bodies) and the inclusion of additional dynamics (such as tidal evolution) self-consistently, owing to the fully general N-body integration. Finally, we remark that in this work the parameters of the transiting planet are *not* fixed, but derived simultaneously from the available data. This mimics follow-ups of transiting planets, whereby the mass of the transiting planet is determined by a small number of RV measurements.

We use the combined χ^2 statistic detailed in Paper I to simultaneously fit the transit timing and follow-up RV datasets. While there is a degree of ambiguity in the choice of the weighing factor λ, this is not a concern in the vicinity of a solution, where the contribution from RVs and transits is approximately equal for $\lambda = 1$. Far from the solution, the contribution from transits to the χ^2 budget is extremely large; however, this is not an issue in practice because we first fit for a one-planet solution, reducing the initial χ^2 to $\chi^2 \sim \delta t/\sigma_{TR}$.

3.4 HD40307

Mayor et al. (2009a) recently announced a three Super-Earth planetary system orbiting

the nearby metal-deficient dwarf HD40307. Interestingly, while this system lies close to a 4:2:1 Laplace resonance chain, such a configuration is ruled out by the observations. The a-priori transit probability for the innermost 4.3d planet is high enough to warrant a transit follow-up; unfortunately, no transit was detected using *Spitzer* (Gillon et al. 2010), preventing the placement of desirable constraints on the bulk composition of the three planets.

We derived the orbital parameters for the system using the publicly available HARPS dataset, obtaining best-fit and error estimations in good accordance with the published configuration. As can be seen by Figure 3.1, the difference in RV signal between a fully integrated model (using Bulirsch-Stoer) versus simple superposition of Keplerian orbits is negligible compared to the HARPS error bars and the RV residuals.

As a comparison, we derived synthetic TTV computed comparing a simple linear fit to synthetic transits computed with the fully integrated solution above; we assumed, respectively, planets b and c to be transiting and computed the primary transit timings for the HARPS observation window. To each transit timing observation, we added a Gaussian white noise of amplitude $\sigma = 2 \times 10^{-4}$ d (0.3 minutes), as a simple, conservative model for *Kepler* timing uncertainties. The TTV dataset is shown in Figure 3.2. The amplitude of the TTV signal for planet c is approximately 5σ, making it a far more sensitive probe of the mutual gravitational perturbations than the highest-precision RV measurements available.

Although no transits have been so far detected for planet b, the transit probability for planet c is a tantalizing 5% and the transit depth is of order 400 ppm, fully within the capabilities of *Kepler*. Therefore, it is an interesting illustrative test-case problem to use the known orbital elements of the HD40307 system and analyze the constraints imposed by TTV on the perturbing planet, in absence of high-precision radial velocities. Given that the bulk of the signal originates from the mutual perturbation between planets c and d, we hereafter solve the simpler two-planet inverse problem and neglect the contribution from planet b. The orbital

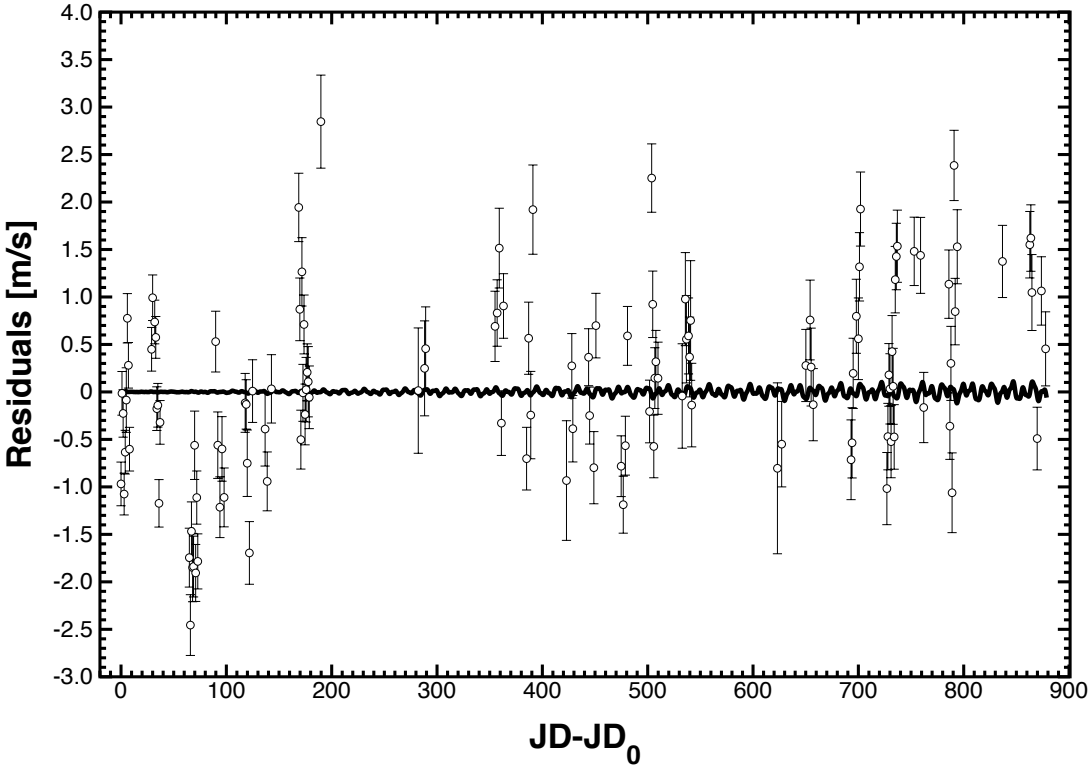

Figure 3.1: Sensitivity of the RV method to the mutual gravitational perturbations: Keplerian model subtracted from the integrated model (thick curve) compared to the HARPS residuals (empty circles).

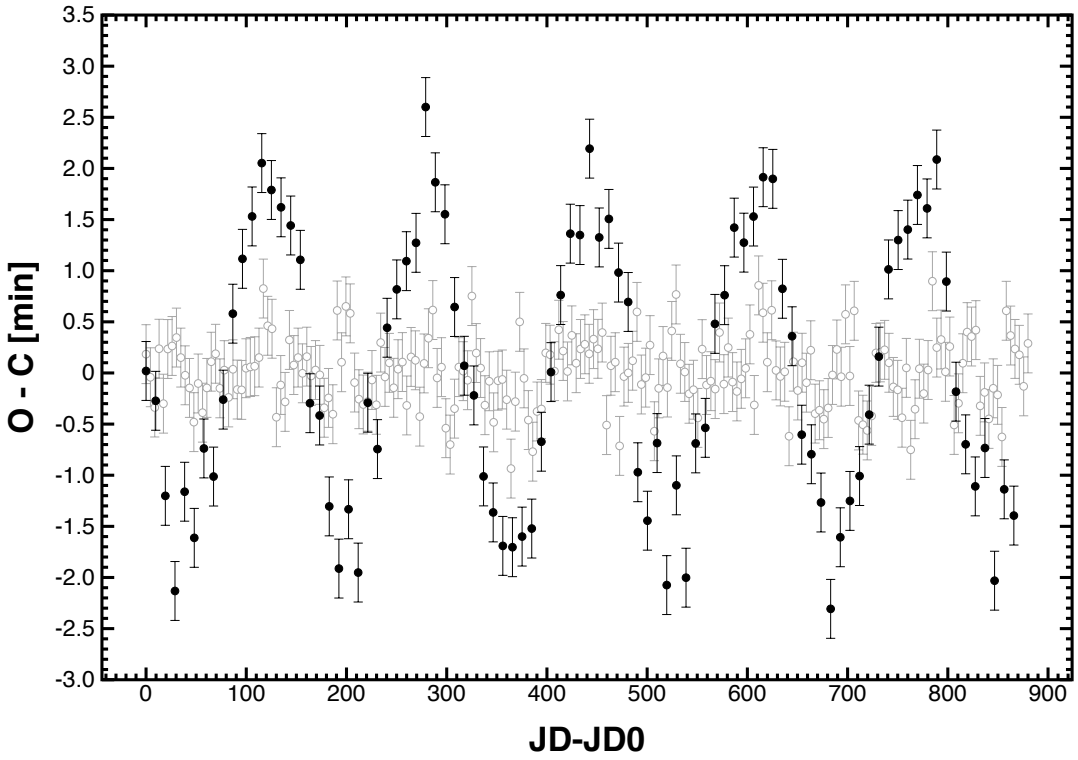

Figure 3.2: Predicted transit timing variations for planets b (empty circles) and c (black circles), over the HARPS observation window.

	Best fit (HARPS)	Best fit (100d)	Best fit (365d)
P (days)	9.621 (1)	9.6214 (4)	9.62114 (5)
	20.439 (5)	20.2 (2)	20.45 (1)
$\mathcal{M}$ ($\mathcal{M}_J$)	0.0218 (6)	0.021 (5)	0.02 (1)
	0.0290 (8)	0.025 (4)	0.025 (2)
e	0.06 (3)	0.036 (3)	0.034 (4)
	0.12 (2)	0.06 (3)	0.01 (2)
ϖ (°)	284 (6)	358 (4)	358.2 (1)
	12 (7)	78 (23)	71 (4)
χ^2	10.49	1.29	1.15
RMS (m s^{-1})	1.04	1.17	1.25
χ^2_{TR}	–	0.4	0.75

Table 3.1: Best-fit solutions for the HD40307 system. The error on the least significant digit is indicated in parentheses.

elements of the generating fit are reported in Table 3.1.

We generated two sets of central transit observations spanning 100 days (11 transits) and 365 (38 transits); we assumed every transit is detected with $\sigma_{tr} = 2 \times 10^{-4}$ d. We also computed a small set of "follow-up" synthetic radial velocity observations (10 points), which set the scale for the mass and the eccentricity of the transiting planet (period and mean anomaly at epoch being primarily determined by the transit timing). We draw the measurement errors to mimic mid-range precision observations; the average measurement error is ~ 1.5 m/s. As a comparison, we also computed a third synthetic RV dataset drawing from the HARPS schedule and measurement errors for the two planets alone; we assumed a small jitter of ~ 0.7 m/s. We point out that this jitter is excellent, and depending on the properties of the parent star, a realistic case might require more RVs.

Eight SA simulations were launched (one per core on a Mac Pro Xeon workstation), with initial temperature and step size regulated to achieve 25% acceptance rate in each orbital parameter. The initial configuration used the parameters from a single planet best-fit for the transiting planet, and random elements for the perturbing planet (period, mass, eccentricity, mean anomaly and longitude of pericenter), avoiding orbit-crossing configurations. For the sake

of efficiency, we constrained the period of the second planet between 1.5 and 5 times the period of the inner planet, the masses between 0.3 and 32 $\mathcal{M}_{\oplus}$ and the eccentricity between circular and 0.5. This parameter range approximately spans the region where the transit timings are sensitive to the perturbations, but the reflex stellar semiamplitude K is not so large to be readily picked up by RV observations. Finally, every 2,000 steps the current configuration was submitted to the AMOEBA routine to attempt direct convergence to a solution. The minimization routine is considered to be converged and the solution is retained if $\chi^2_{TR} < 1.1$ and the radial velocity $RMS < \overline{\sigma}_{RV}$, corresponding to a combined $\chi^2 \sim 1.3$. After a predetermined number of steps (10,000), if no improvement in the total χ^2 has been reached, the suboptimal solution is discarded and a new set of initial conditions is chosen. A sample of 20 candidate solutions was derived for each dataset; each solution representing a local minimum. The lowest χ^2 solution was chosen as the representative best-fit.

An estimation of the uncertainties on the orbital parameters of the best-fit solutions was derived using the Markov Chain Monte Carlo algorithm (MCMC; Ford 2005). While the synthetic HARPS dataset is amenable to a bootstrap resampling technique, the rugged χ^2 landscape for the TTV dataset turned out to be excessively complicated for an efficient exploration, yielding artificially low parameter uncertainties. The simple MCMC algorithm presented in Paper I derived error bars in accordance with bootstrap estimates for the RV dataset. We use uniform priors in $\{\log P,\, \log \mathcal{M},\, M_0,\, e,\, \varpi\}$; while more sophisticated approaches are available (e.g. incorporating information from Eqn. 3.2 as a constraints), the size and precision of the synthetic datasets provide strong constraints on the model parameters and the choice of the priors should not affect our results (Ford 2006). We construct MCMC chains of 50,000 states, each state consisting of 200 iterations. The initial 10% portion of the chain is considered "burn-in" and discarded.

The best-fit solutions to the three datasets (synthetic HARPS, 100-d and 365d TTVs

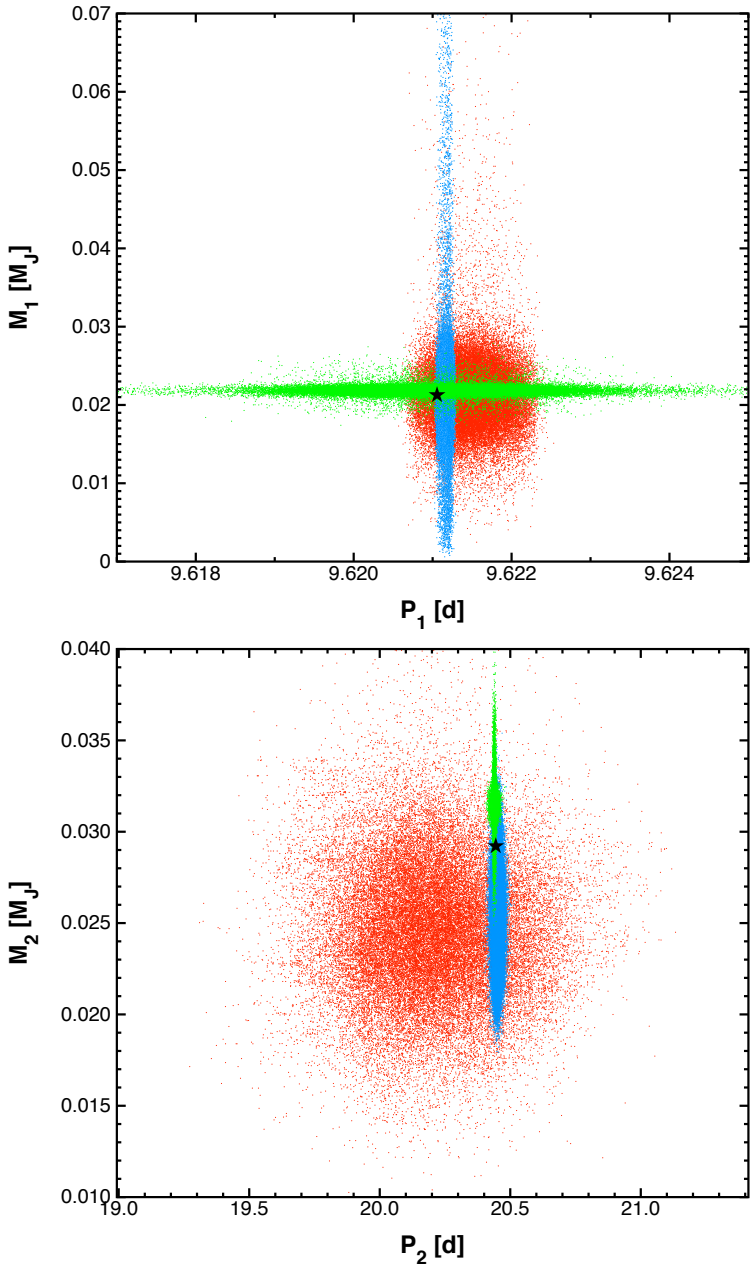

Figure 3.3: Results of a MCMC simulation consisting of 50,000 states computed from the HARPS dataset (green points), 100 days of transit timing observations + 10 follow-up RVs (red points), 365 days of transit observations + 10 follow-up RVs (blue points). The parameters of the originating system are marked with a star symbol.

+ RV followup) and respective uncertainties are compared in Table 3.1. To our knowledge, this is the first attempt to fully fit and derive error estimates on a large TTV dataset. We show the parameter scatter for the second planet in Figure 3.3.

The computed parameter uncertainties show a number of interesting properties. Firstly, the period and mass of the second planet are derived to an accuracy comparable to that of the full HARPS dataset, which spans 4.5 years. The detection of a low-mass planet at this level of accuracy showcases the potential of scanning the future *Kepler* datasets for TTV detection candidates. Once again, we stress that our estimate of the central transit timing noise is likely conservative and that stars on the short-cadence list will be observed with an even higher accuracy. While the period of the transiting planet is constrained by the transits timing themselves, the mass is not well constrained because, to a good approximation, the amplitude of the TTVs does not depend on the mass of the transiting planet itself (Equation 3.2) in the non-resonant regime.

Finally, we remark that although the χ^2 landscape allowed for several, well-separated local minima, both the SA and the MCMC algorithms were able to efficiently sample the parameter space. Therefore, it is likely that global minimization routines will be part of the standard toolset to analyze the future *Kepler* transit datasets.

3.5 HAT-P-7

The bright nearby dwarf HAT-P-7 hosts a transiting hot Jupiter, first characterized by the HATNet project (Pál et al. 2008). The star is in the field of view of one of the *Kepler* detectors; ten days of photometric data, as processed by the *Kepler* pipeline, were obtained during the commissioning phase (Borucki et al. 2009). Additional primary transits and a number of secondary eclipses were observed using *EPOXI* and *Spitzer* (Christiansen et al. 2010), with

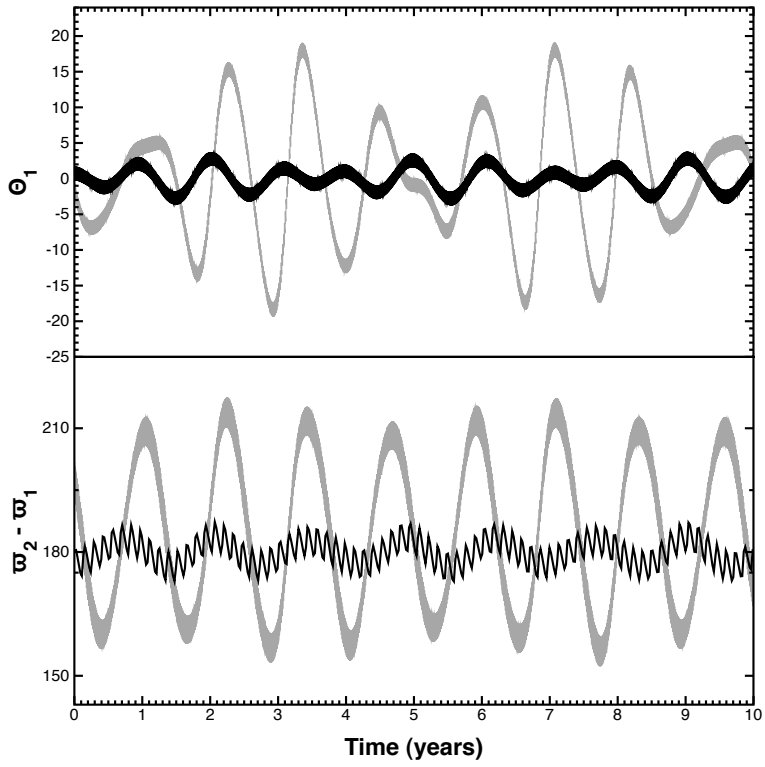

Figure 3.4: Libration (in degrees) of the resonant arguments Θ_1 and $\Delta\varpi$ for the reference configuration (black line) and the best-fit configuration (grey line).

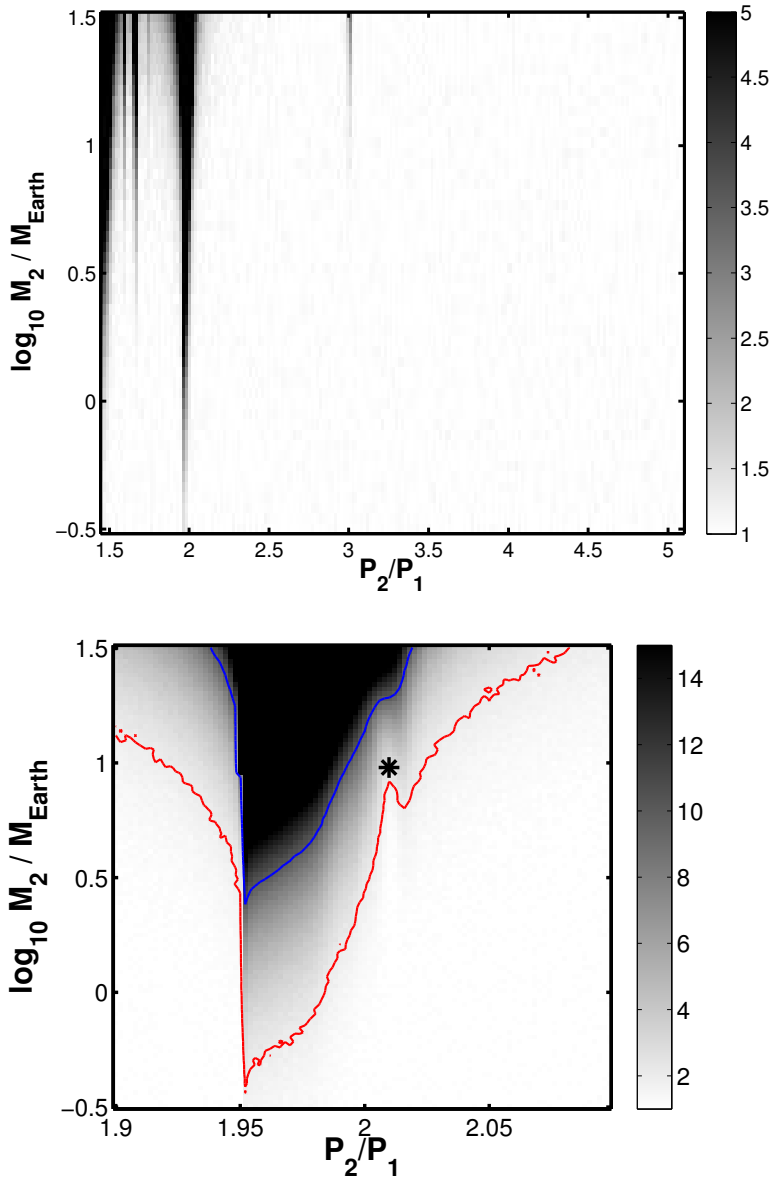

Figure 3.5: *(Top)* Grayscale map of δt (in units of $\sigma_{tr,K} \approx 15$ s) for 10,000 realizations spanning a range of perturber periods and masses, using the reference configuration for the other elements. *(Below)* As above, in the region near the 2:1 resonance. The contours show the parameter space where $\delta t > 2\sigma_{tr}$, assuming $\sigma_{tr} = 2 \times 10^{-4}$ d (*Kepler*, red contour) and $\sigma_{tr} = 10^{-3}$ d (*EPOXI*, blue contour) respectively. The star symbol represents the reference configuration.

the intent of studying the atmospheric properties of the planet. The EPOXI best-fit central times achieved an accuracy of $\sigma_{tr} \approx 10^{-3}$ d (≈ 1.5 minutes).

Given its extensive and diverse coverage, and the inclusion of this planet in the *Kepler* star list, we chose this system as a prototype of the class of massive transiting planets that will be monitored by the *Kepler* mission and may reveal TTVs. In particular, we are interested in assessing the secure detection of a low-mass planet in a 2:1 MMR with the transiting gas giant (we consider only the case of an external perturber in the present analysis).

We generated a realistic resonant configuration self-consistently with the following procedure. We placed the two planets (denoted as 1 and 2, respectively the transiting planet and the external perturber) on originally widely separated orbits; following Lee & Peale (2002), we added a forced migration ($\dot{a}/a = -3 \times 10^{-4}$ yr^{-1}) and an eccentricity damping ($\dot{e}/e = 100\ \dot{a}/a$) term of the outer planet to the equations of motion until resonant capture is achieved. In this reference configuration, the outer planet was captured into an antialigned configuration with $\Theta_1 = 2\lambda_2 - \lambda_1 - \varpi_2$ librating around 0° and $\Delta\varpi = \varpi_2 - \varpi_1$ librating around 180°, with an amplitude of $\approx 5°$(Figure 3.4). The final eccentricities for this choice of forced migration terms are low ($e_1 = 0.002$, $e_2 = 0.027$).

To illustrate the process, we chose a mass for the second planet of $10M_{\oplus}$, since this can yield a TTV signal larger than 1 minute, easily detectable with *Kepler*. Figure 3.5 shows the amplitude of the TTV signal for a choice of periods and masses, at fixed eccentricies and phases; as expected, the TTVs are largest in the proximity of resonances. In particular, 3:2, 2:1 and 3:1 MMRs yield a sizable TTV signal for our range of perturber masses.

We created a TTV dataset spanning 1 year (166 observations) following the procedure in Section 3.4, using the reference configuration as our generating system and Gaussian noise at the level of 2×10^{-4} d. We drew from the schedule and uncertainties of the Keck/HIRES follow-up observations (Pál et al. 2008) to generate the accompanying RV dataset. We note that

given the small semi-amplitude K_2 (≈ 2.8 m/s, larger than the typical error in the Keck dataset but smaller than the stellar jitter ≈ 3.8 m/s) and the few RV points available, the RV dataset places only a weak constraint on the parameters of the perturbing planet.

We launched a number of SA chains and allowed the parameters of the perturbing planet to float freely. We found that the best-fitting solutions comprised a set of degenerate configurations, shown in Figure 3.6. The fitting routine found two groups of solutions: configurations lying near a 2:1 MMR and configurations lying near a 3:1 MMR can fit the TTV signal equally well. Additionally, the degeneracy between mass and eccentricity of the perturbing planet makes it impossible to place a strong constraint on the mass of the second planet.

This non-uniqueness of the inverse problem was already noted in Nesvorný & Morbidelli (2008); the measurement errors filter out some of the TTV harmonics. The authors also pointed out that the non-uniqueness threshold (the measurement uncertainty that leads to a unique solution) of the number of transits detected; accordingly, we verified that a transit dataset covering 2 years of observations still yielded the two groups of solutions. Reducing the error on the transit measurement to 5×10^{-5} d (4 seconds), while not breaking the resonance degeneracies, reduced the range of possible masses somewhat (Figure 3.6). Finally, only a fraction of the solutions (about 10%) have librating resonant arguments; the ones that do show a much larger amplitude of libration than the reference system ($\Theta_1 \sim 20-40°$, $\Delta\varpi \sim 30-70°$; see Figure 3.4). This suggests that the TTV signal alone is not enough to constrain the resonant angles.

Our result is particularly remarkable in that the best-fitting solutions cluster around two different MMRs, preventing a precise characterization of the resonance. Since the two solutions yield a different RV semi-amplitude K_2, this degeneracy may be broken with RV observations. Even a small RV dataset, where uncertainty and jitter do not completely wash out the planetary signal, can help constrain the parameters of the perturbing planet to a reasonable level. Indeed, we verified that a second RV dataset comprising 20 measurements with lower jitter

($\sim$ 1 m/s) sufficed to constrain the best-fit solutions to the neighborhood of the 2:1 MMR. We conclude that while TTVs can be usefully exploited to infer the presence of low-mass perturbing planets, a small number of RV measurements with a precision comparable to K_2 is crucial in recognizing the nature of the planetary companion. This fact makes it much more desirable to find configurations orbiting bright parent stars.

3.6 HAT-P-13

HAT-P-13 was the first system known to contain a transiting planet, b, and an eccentric outer planet, c, well characterized through RVs (Bakos et al. 2009). No transits of planets c have been detected thus far. A complete characterization of the three-dimensional configuration of the system can establish the internal structure of planet b (Batygin et al. 2009) and possibly the formation and scattering history of the system, with certain ranges of inclination being favored on theoretical grounds (Mardling 2010).

Transit timing variations can provide the required constraints on the mutual inclination (I) and the nodal line marking the intersection of the two orbital planes (Ω), should transits of c not be detected. The amplitude and shape of the TTV signal depend significantly on the two parameters (Payne et al. 2010), although this dependence is not trivial.

Figure 3.7 shows the TTV signal for a number of inclinations. We centered our dataset around $T_{peri,\ c}$ since the different solutions can be best distinguished by the sharp feature in the neighborhood of the pericenter passage of c. While the discovery paper predicted a TTV amplitude of order 15-20 seconds, the updated configuration presented in Winn et al. (2010) reduces the expected δt near the pericenter passage by a factor ~ 2, to about 7 seconds for $I \approx 0$. Winn et al. (2010) also measured a prograde Rossiter-McLaughlin effect, suggesting that both orbits are prograde.

We produced several transit datasets for mutual inclinations in the range $0 < I < 90°$and $\Omega = 0$, assuming that all transits between $T_{peri,\ c} - 100$ d and $T_{peri,c} + 100$ d are detected; the other elements were drawn using the published uncertainties (Winn et al. 2010). We added white noise to the TTV signal at the 4×10^{-5} d = 3.5 s level (in order to have $\delta t/\sigma_{tr} > 2$). The RV measurements were generated drawing from the schedule and uncertainties of the Keck/HIRES dataset as reported in the discovery paper.

We used our usual fitting procedure (Bulirsch-Stoer as our integration scheme and Simulated Annealing and AMOEBA in tandem to pinpoint the solution), with the published fit as our starting configuration. When a solution was found, we estimated the uncertainty by running our MCMC algorithm. We generated 4×10^6 trial models; of those, the first 10% was discarded and only one model every 50 was retained in order to minimize correlations between successive elements of the Markov chain. Figure 3.8 shows the marginal distribution of the fitted relative inclinations for systems with various degrees of inclination ($I = 0°, 5°, 15°, 45°$ and 75°). The inclination is well constrained for polar and near-polar configurations of the outer planet, where the TTV signal is sizable; on the other hand, for low inclinations there is a large range of allowed configurations. However, it is clear that while the inclination distributions are broad, they are consistent with the originating configuration and can discriminate between low-inclination and high-inclination configurations.

3.7 Discussion

In this paper we outlined a procedure to solve the inverse problem of deriving best-fitting model parameters and associated uncertainties using synthetic radial velocity and transit timing variations datasets simultaneously. The procedure exploits a number of numerical algorithms that are made available to the community through the Systemic Console package.

We tested our fitting method against a number of synthetic realizations of different planetary configurations, including a system of non-resonating coplanar super-Earths, a system in a deep 2:1 resonance and a non-coplanar system. The transit timing datasets were derived assuming continuous photometric coverage as provided by *Kepler*, and thus are fully realistic to the extent that the transit timing error can be modeled as white noise with a constant amplitude. Our analysis shows that combined RV and TTV datasets carry enough dynamical information to characterize a system in its full three-dimensional configuration.

Inverse problems have a storied place in astronomy, with the discovery of Neptune providing a canonical example. In that case, a fortunate orbital geometry allowed Neptune's sky position to be pinpointed with sufficient accuracy that the "prediction" of a new planet could credibly be claimed. It is worth pointing out, however, that the accurate ephemeris for Neptune in 1846 was something of a lucky accident. Both Adams' and Le Verrier's masses and semi-major axes were badly off (Grant 1852). The correct position of the planet that emerged from the calculations stems from a degeneracy of solutions during the period surrounding the conjunction of Uranus and Neptune.

We have found that a similar state of affairs might apply to the transit timing measurement scenarios that will emerge from *Kepler*. While departure from strict periodicity can be readily measurable, it is generally difficult to work out the complete system configuration from transit timing measurement alone. We confirmed that the suppression of TTV harmonics by the transit timing noise can lead to severe degeneracies in the model parameters, as first pointed out by Nesvorný & Morbidelli (2008), even when very low levels of timing error is added to the synthetic data. In presence of such degenerate set of solutions, however, we have verified that adequate RV data can single out the correct orbital configuration. We note that other constraints derived by extracting more observables from the photometry, such as the the duration of the transits and their variations (TDV – Kipping et al. 2009, Kipping 2010), may also

help remove the degeneracies in the solution. Including these contributions will require more sophisticated modelling approaches.

Finally, we note that our work did not investigate other competing effects that contribute to the TTV signal, chiefly including, but not limited to, light travel time, excitation of tidal modes in the host star, general relativity and the presence of additional planets. Furthermore, the investigation of planetary systems with $N_{pl} > 2$ with the methods presented here might be computationally costly due to the large parameter space.

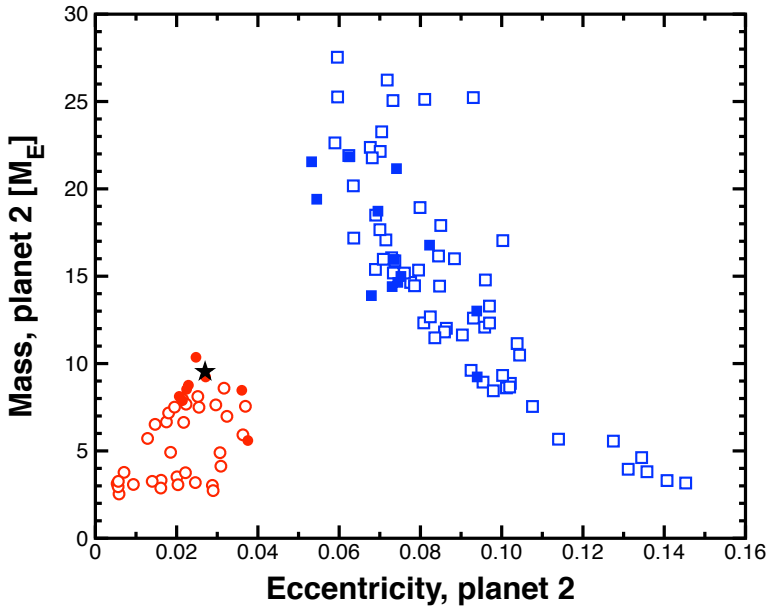

Figure 3.6: Best-fit solutions for the HAT-P-7 dataset lying near the 2:1 resonance (circles) and the 3:1 resonance (squares), for two different levels of noise in the TTV measurements: 2×10^{-4} (empty symbols) and 5×10^{-5} (filled symbols).

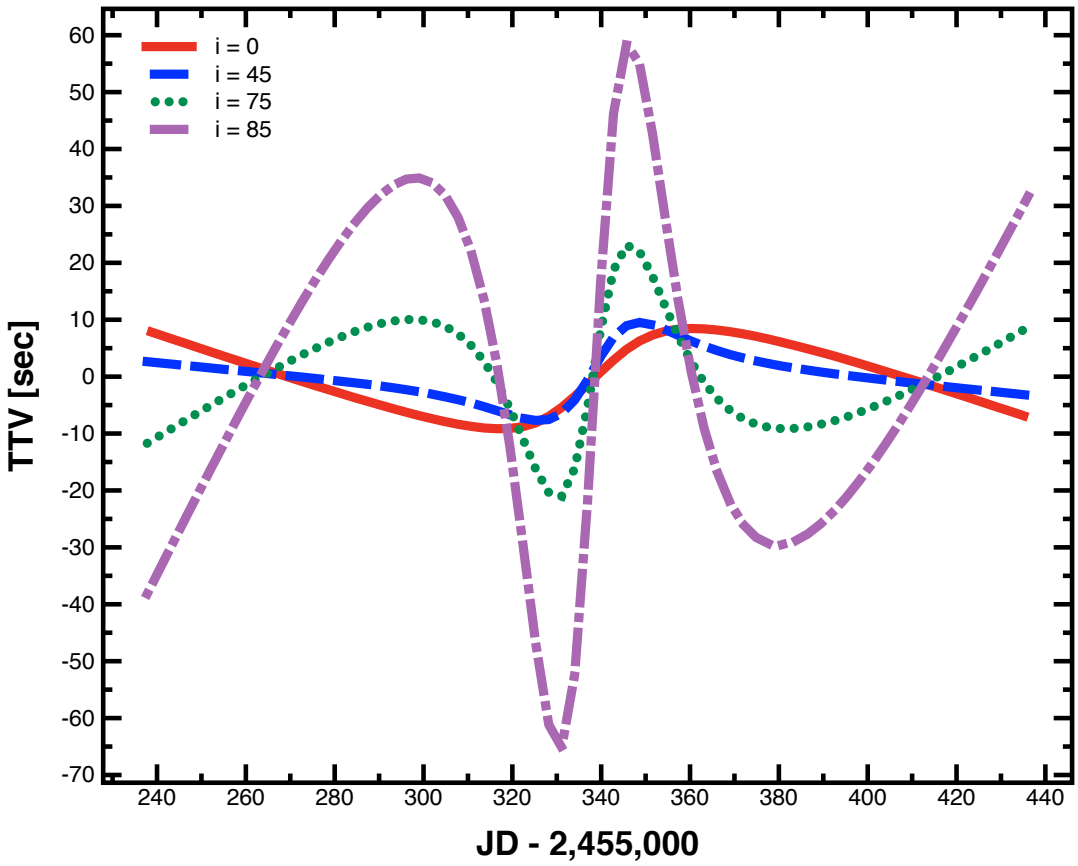

Figure 3.7: Sample TTV signals for four different inclinations of HAT-P-13 c. Orbits close to perpendicular give rise to large TTV signals.

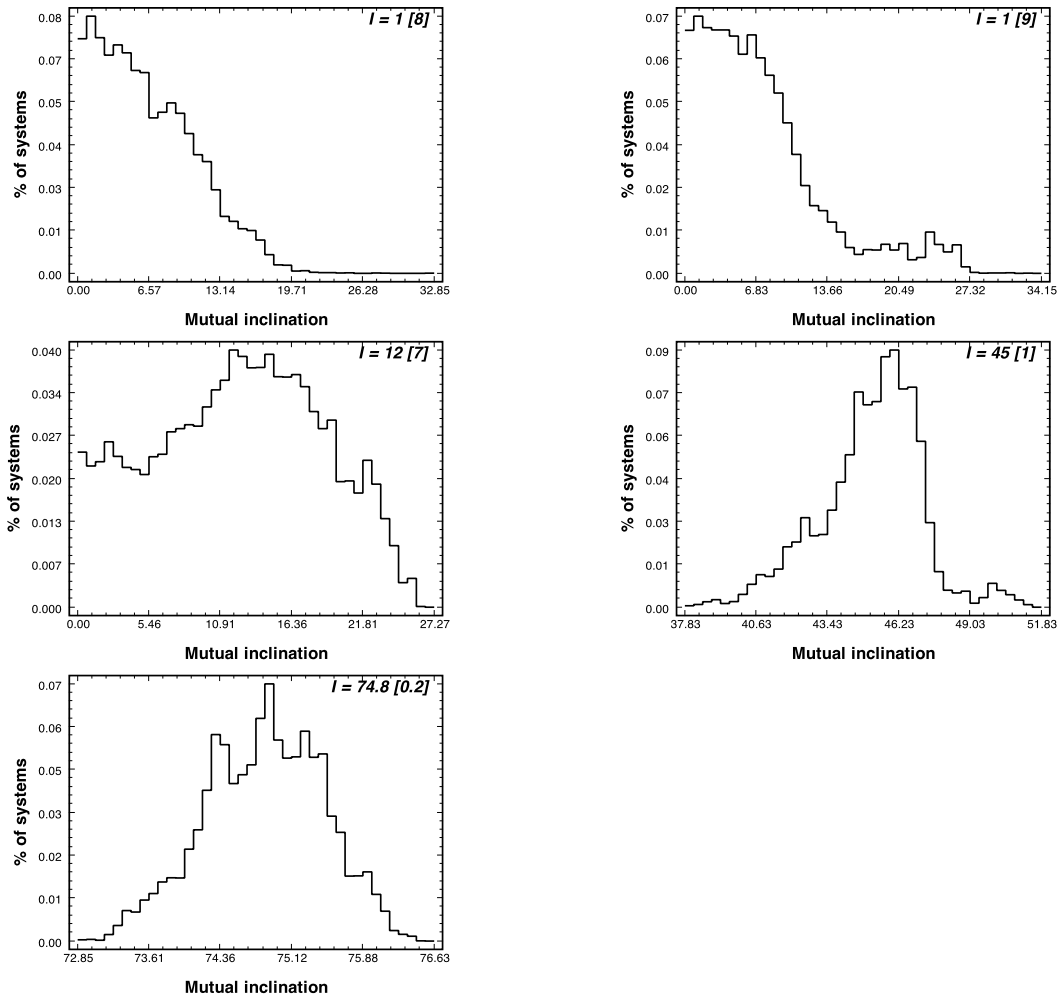

Figure 3.8: Relative inclination distribution for synthetic HAT-P-13 realizations with $I = 0, 5, 15, 45$ and 75 degrees respectively. The median inclination and standard deviation are given inside each plot.

Chapter 4

The Lick-Carnegie Survey: Four New Exoplanets

4.1 Abstract

We present new precise HIRES radial velocity (RV) data sets of five nearby stars obtained at Keck Observatory. HD 31253, HD 218566, HD 177830, HD 99492 and HD 74156 are host stars of spectral classes F through K and show radial velocity variations consistent with new or additional planetary companions in Keplerian motion. The orbital parameters of the candidate planets in the five planetary systems span minimum masses of $\mathcal{M} \sin i = 27\mathcal{M}_{\oplus}$ to $8\mathcal{M}_J$, periods of 17 to 4696 days and eccentricities ranging from circular to extremely eccentric ($e \approx 0.63$).

The 5th star, HD 74156, was known to have both a 52-day and a 2500-day planet, and was claimed to also harbor a 3rd planet at 336d, in apparent support of the "Packed Planetary System" hypothesis. Our greatly expanded data set for HD 74156 provides strong confirmation of both the 52-day and 2500-d planets, but strongly contradicts the existence of a 336-day planet,

and offers no significant evidence for any other planets in the system.

4.2 Introduction

The planetary census has reached an impressive 496 extrasolar planets. Planetary companions have been successfully detected using a variety of techniques, primarily radial velocities (463; see e.g. Mayor & Queloz 1995, Butler et al. 2006, Udry et al. 2007) and transit photometry (106; see e.g. Henry et al. 2000, Charbonneau et al. 2000, Charbonneau et al. 2007). Other techniques employed include microlensing (Bennett 2008), astrometry (Benedict et al. 2002, Bean & Seifahrt 2009), stellar pulsations (Silvotti et al. 2007) and even direct imaging (Chauvin et al. 2005, Kalas et al. 2008, Marois et al. 2008) [1].

The radial velocity method has been used to either detect or characterize more than 90% of all currently known planets, and continues to be a very important technique. Both its continued productivity (e.g. Valenti & Fischer 2005) and its ability to accurately probe planetary architectures into the vicinity of the terrestrial mass region (e.g Rivera et al. 2005, Mayor et al. 2009b, Vogt et al. 2010) are a testament to the rapid technological advances.

We have been monitoring a large set of nearby stars under precise radial velocity survey with the High Resolution Echelle Spectrometer (HIRES) at Keck for the past 17 years. In this paper, we present new radial velocity (RV) observations for five of our target stars: HD 31253, HD 218566, HD 177830, HD 99492 and HD 74156.

The plan of this paper is as follows. In Section 4.3, we discuss the procedure followed to obtain and reduce the RV dataset. In Sections 4.4 through 4.8 we describe the main stellar properties, derive model Keplerian fits with associated parameter uncertainties and discuss the planetary systems they imply. Finally, we discuss the new planetary companions in Section 6.6.

[1] Source: http://www.exoplanet.eu, retrieved on 06/14/2010

4.3 Radial Velocity observations and target stars

The HIRES spectrometer (Vogt et al. 1994) of the Keck-I telescope was used for all the new RVs presented in this paper. Doppler shifts were measured in the usual manner (Butler et al. 1996) by placing an Iodine absorption cell just ahead of the spectrometer slit in the converging beam from the telescope. This gaseous Iodine absorption cell superimposes a rich forest of Iodine lines on the stellar spectrum, providing a wavelength calibration and proxy for the point spread function (PSF) of the spectrometer. The Iodine cell is sealed and temperature-controlled to 50 $\pm$ 0.1 C such that the column density of Iodine remains constant. For the Keck planet search program, we operate the HIRES spectrometer at a spectral resolving power R $\approx$ 70,000 and wavelength range of 3700-8000 Å, though only the region 5000-6200 Å (with Iodine lines) is used in the present Doppler analysis. A block of the spectrum containing the Iodine region is divided into $\sim$700 chunks of 2 Å each. Each chunk produces an independent measure of the wavelength, PSF, and Doppler shift. The final measured velocity is the weighted mean of the velocities of the individual chunks. All radial velocities have been corrected to the solar system barycenter, but are not tied to any absolute radial velocity system. As such, they are "relative" radial velocities, with a zero point that is usually set simply to the mean of each set.

The internal uncertainties quoted for all the RV's in this paper reflect only one term in the overall error budget, and results from a host of systematic errors from characterizing and determining the PSF, detector imperfections, optical aberrations, effects of under-sampling the Iodine lines, etc. Two additional major sources of error are photon statistics and stellar jitter. The latter varies widely from star to star, and can be mitigated to some degree by selecting magnetically-inactive older stars and by time-averaging over the star's unresolved low-degree surface p-modes. All observations have been further binned on 2-hour timescales.

We present in Table 4.1 a few basic parameters (and uncertainties, where available) for

all the host stars considered in this paper. Unless otherwise noted, the data are mostly as listed in the SPOCS database (Valenti & Fischer 2005) and the NASA NStED database[2].

Table 4.2 summarizes all the Keplerian fits for the target stars in this paper; they will be discussed in more detail in the following sections. The orbital fits were derived using the Systemic Console (Meschiari et al. 2009). The errors on each parameter are estimated using the bootstrap technique with 5000 scrambled realizations of the RV datasets. For each planet, we list best-fit period (P), eccentricity (e), semi-amplitude (K), time of periastron passage (T_{peri}), longitude of pericenter (ϖ), minimum mass ($\mathcal{M}\ \sin i$) and semi-major axis (a). Additionally, we report approximate estimates of the transit probability calculated as part of the Monte-Carlo modeling, assuming a putative radius $\mathcal{R} = \mathcal{R}_{JUP}$.

4.4 HD 31253 (HIP 22826)

4.4.1 Stellar properties

HD 31253 is a V = 7.133 magnitude star of spectral class F8. Relative to the Sun, HD 31253 is modestly metal-rich ([Fe/H] = 0.16).

This $1.23\mathcal{M}_{\odot}$ star has a reported $V \sin i$ of 3.8 m s^{-1} which, in conjunction with its derived radius, implies a maximum rotation period of about 23 days. Our measurement of $\log R'_{hk}$= -5.13 agrees well with that listed on the NASA NStED site, and leads to an estimate of $\sim$2.3 for the expected radial velocity jitter due to stellar surface activity (Wright 2005).

4.4.2 Keplerian solution

Table A.1 shows the complete set of 39 relative radial velocity observations for HD 31253. The radial velocity coverage spans approximately 13 years of RV monitoring. The

[2]http://nsted.ipac.caltech.edu/

Parameter	HD 31253	HD 218566	HD 177830	HD 99492	HD 74156
Spec. Type	F8	K3V	K0IV	K2V	G1V
M_v	3.48 [a]	6.21 [b]	3.3	6.3	3.56 [c]
$B-V$	0.58	1.013	1.091	1.053	0.581
V	7.133	8.628	7.177	7.383	7.614
Mass ($\mathcal{M}_\odot$)	1.23 [0.05]	0.85 [0.03] [d]	1.47	0.83 [d]	1.24
Radius ($\mathcal{R}_\odot$)	1.71 [0.17]	0.86 [0.08]	2.62 [0.06]	0.96 [0.11]	1.64 [0.19]
Luminosity ($L_\odot$)	3.286 [0.446]	0.353 [0.032]	4.842 [1.003]	0.418 [0.057]	3.037 [0.485]
Distance (pc)	53.82 [3.45]	29.94 [1.11]	59.03 [2.77]	17.99 [1.14]	64.56 [4.93]
$V \sin i$ (km s^{-1})	3.8	0.0	2.5	1.4	4.3
S_{hk}	0.141 [0.018]	0.297	0.125 [0.016]	0.254 [0.033]	0.144
$\log R_{hk}$	-5.11	-4.88	-5.37	-4.84	-5.08
Age (Gyr)	3	8.5	2.2 - 6.6	4	3.7 [0.4] [d]
$[Fe/H]$	0.16	0.38	0.545 [0.03]	0.36	0.13
T_{eff} (K)	5960.0	4820.0	4949	4740.0	5960.0 [100.0]
$\log g$	4.1	4.81	3.65	4.77	4.4 [0.15] [c]
P_{rot}	23	-	65 [f]	45 [e]	-

[a] Nordström et al. (2004)

[b] Wright et al. (2004)

[c] Naef et al. (2004)

[d] Takeda et al. (2007)

[e] Marcy et al. (2005)

[f] Barnes (2001)

Table 4.1: Stellar parameters

Parameter	HD 31253	HD 218566	HD 177830	HD 99492	HD 74156
P (d)	466 [3] †	225.7 [0.4] †	406.6 [0.4]	17.054 [0.003]	2520 [15]
			110.9 [0.1] †	4970 [744] †	51.638 [0.004]
e	0.3 [0.2]	0.3 [0.1]	0.009 [0.004]	0.13 [0.07]	0.38 [0.02]
			0.3 [0.1]	0.1 [0.2]	0.63 [0.01]
K (m s^{-1})	12 [2]	8.3 [0.7]	31.6 [0.6]	7.9 [0.6]	115 [3]
			5.1 [0.8]	4.9 [0.7]	108 [4]
T_{peri} - 2,440,000 (JD)	10660 [19]	10360 [154]	10154 [35]	10449 [2]	8416 [33]
			10179 [7]	9636 [2210]	10793.3 [0.2]
ϖ (deg)	244 [23]	36 [24]	85 [31]	196 [32]	268 [4]
			110 [29]	38 [64]	174 [2]
$M \sin i$ ($\mathcal{M}_J$)	0.50 [0.07]	0.21 [0.02]	1.49 [0.03]	0.087 [0.006]	8.2 [0.2]
			0.15 [0.02]	0.36 [0.06]	1.78 [0.04]
a (AU)	1.260 [0.006]	0.6873 [0.0008]	1.2218 [0.0008]	0.12186 [0.00002]	3.90 [0.02]
			0.5137 [0.0003]	5.4 [0.5]	0.29169 [0.00001]
P_{tr}	0.004	0.007	0.004	0.04	0.001
			0.010	0.0008	0.03
N_{obs} [Median uncertainty]	KECK: 39 [1.59]	KECK: 56 [1.27]	KECK: 88 [1.06]	KECK: 93 [1.36]	CORALIE04: 44 [7]
					ELODIE04: 51 [12]
					HET09: 82 [8]
					KECK: 29 [1.98]
Epoch (JD)	2450838.7519	2450366.8550	2450276.0239	2450462.1140	2450823.5570
χ^2	8.87	8.41	15.31	7.17	3.09
RMS (m s^{-1})	4.23	3.48	3.85	3.22	12.80
Jitter (m s^{-1})	3.92	3.23	3.71	2.94	8.59

Table 4.2: Keplerian orbital solutions. † indicates a new planet candidate.

median internal uncertainty for our observations is 1.59 m s^{-1}, and the peak-to-peak velocity variation is 36.37 m s^{-1}. The velocity scatter around the average RV in our measurements is 8.92 m s^{-1}.

The top panel of Figure 4.1 shows the individual RV observations for HD 31253 . The middle panel shows the error-weighted Lomb-Scargle (LS) periodogram of the full RV dataset (Gilliland & Baliunas 1987). The three horizontal lines in this figure and other comparable plots represent, from top to bottom, the 0.1%, 1.0%, and 10.0% analytic False Alarm Probability (FAP) levels, respectively. The analytic FAPs are computed using a straightforward approach, where we estimate the number of independent frequencies by analyzing a set of 1,000 gaussian deviates with the same timestamps as the original dataset (Press et al. 1992).

For the highest peak, the quoted FAP is estimated using a more robust Monte Carlo approach, which consists of generating sets of scrambled realizations of the dataset and determining the maximum periodogram power for each (e.g. Marcy et al. 2005). For all the datasets presented in this paper, we analyze 3×10^5 scrambled datasets.

The computed FAP for the strong Keplerian signal at $P = 460.32$ days in the RV dataset indicates an estimated FAP $\approx 4 \times 10^{-5}$. Finally, the lower panel of Figure 4.1 shows the spectral window. A peak at frequency, f_s in the spectral window function can be associated with aliases occurring at $|f_p \pm f_s|$, where f_p is a true periodicity of the input signal. For more details, see Dawson & Fabrycky (2010). Peaks in the spectral window function are often associated with relatively immutable periodicities in the observational cadence, such as those arising from the sidereal and solar day, the lunar synodic month and the solar year. The strongest peak in the periodogram is well-fit by a Keplerian orbit of period 465.54 days and semi-amplitude $K = 12.22$ m s^{-1}. Together with the assumed stellar mass of 1.23 $\mathcal{M}_\odot$, this amplitude implies a minimum mass of $\mathcal{M} \sin i = 0.50 \mathcal{M}_J$. The best-fit orbit for the planet is mildly eccentric ($e \approx 0.34$). This 1-planet fit achieves a reduced $\chi^2 = 8.87$, with an RMS of 4.23 m s^{-1}. The expected jitter of

HD 31253 (that is, the amount of jitter required to bring the reduced χ^2 of the best-fit solution to 1.0) is 3.92 m s^{-1}.

The top panel of Figure 4.2 shows the phased stellar reflex velocity of HD 31253 compared to the RV dataset. The middle panel shows the residuals to the 1-planet solution. Finally, the bottom panel shows the periodogram of the residuals of the best-fit solution. No interesting peaks are evident, indicating that the present data set provides no strong support for additional planets in the system.

We do not have photometry of HD 31253 that might conclusively rule out stellar rotation signatures as a cause of the RV variations. But this star does have a measured $V \sin i$ of 3.8 m s^{-1} which implies a maximum rotation period of about 23 days, much shorter than the 466-d Keplerian period. The semi-amplitude of the observed variations is 12 m s^{-1}, whereas a 466-d rotation period, combined with a stellar radius of 1.71 $\mathcal{R}_\odot$, would not produce radial velocity effects above a few tenths of a m s^{-1}. Therefore, stellar rotation can sensibly be ruled out as being responsible for the observed RV variations.

4.5 HD 218566 (HIP 114322)

4.5.1 Stellar properties

HD 218566 is a V = 8.628 magnitude star of spectral class K3V. In comparison to the Sun, HD 218566 is quite metal-rich ([Fe/H] = 0.38). Table 4.1 reports some of the salient stellar properties, as reported by NStEd, Wright et al. (2004) and Takeda et al. (2007).

4.5.2 Keplerian solution

Table A.1 shows the 56 relative radial velocity observations for HD 218566. The radial velocity coverage spans approximately 14 years of RV monitoring. The median internal uncer-

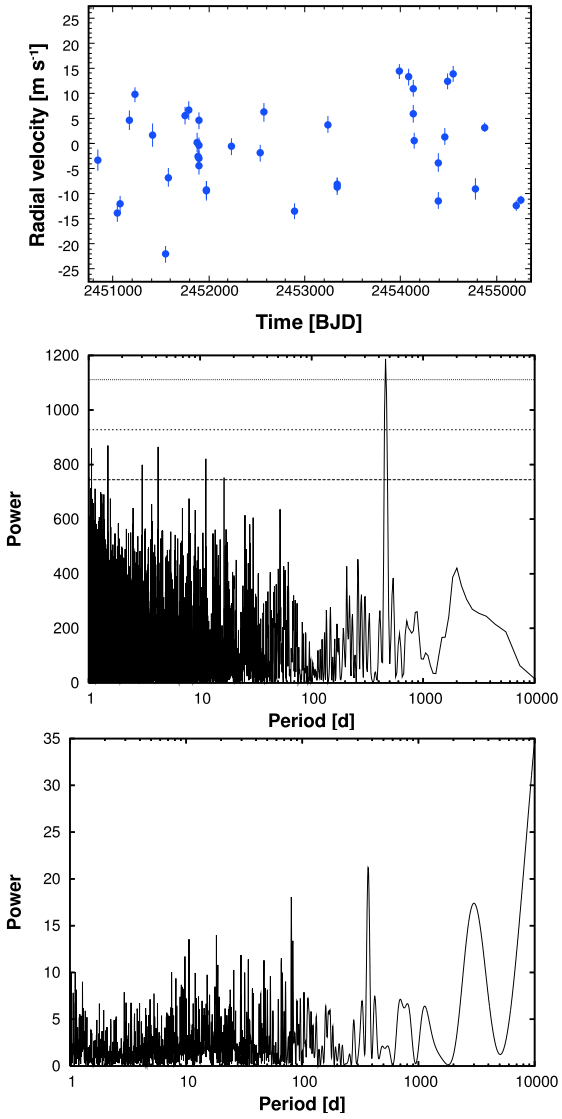

Figure 4.1: Radial velocity data and periodograms for HD 31253. *Top panel:* Relative radial velocity data obtained by KECK. *Middle panel:* Error-weighted Lomb-Scargle periodogram of the radial velocity data. *Bottom panel:* Power spectral window.

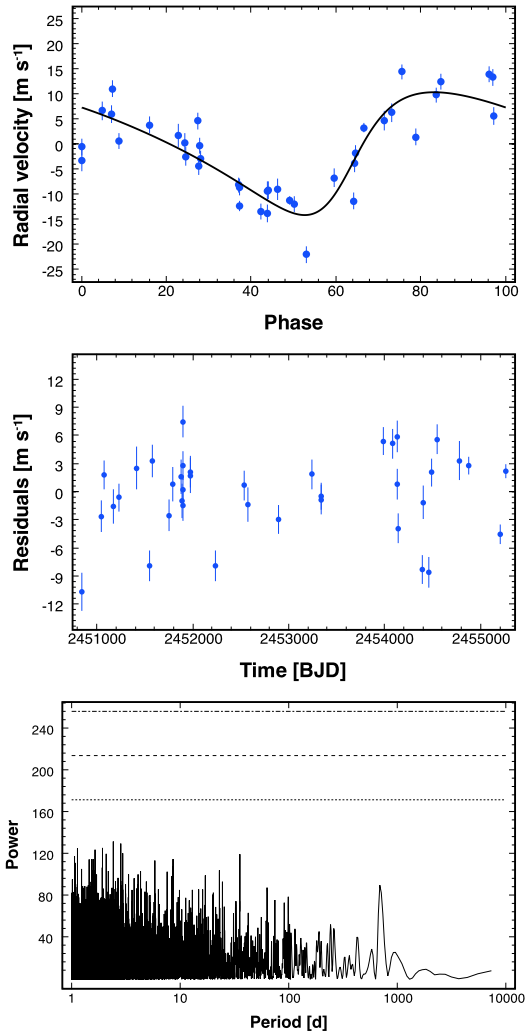

Figure 4.2: Keplerian solution and residuals periodogram for HD 31253. *Top panel:* Phased Keplerian fit. *Middle panel:* Residuals to the 1-planet Keplerian fit. *Bottom panel:* Periodogram of the residuals to the 1-planet best-fit solution.

tainty for our observations is 1.27 m s^{-1}, and the peak-to-peak velocity variation is 28.46 m s^{-1}. The velocity scatter around the mean RV in our measurements is 7.18 m s^{-1}.

The top panel of Figure 4.3 shows the individual RV observations for HD 218566. The middle panel shows the error-weighted Lomb-Scargle (LS) periodogram of the full RV data set, while the bottom figure shows the spectral window. The FAP calculation for the strong Keplerian signal at $P = 225.06$ days in the RV dataset indicates an estimated FAP $\approx< 4 \times 10^{-6}$. The dominant peak in the periodogram can be explained by a Keplerian orbit of period 225.73 days and semi-amplitude $K = 8.34$ m s^{-1}. This amplitude suggests a minimum mass of $\mathcal{M} \sin i = 0.21 \mathcal{M}_J$ (assuming a stellar mass of 0.88 $\mathcal{M}_\odot$). The best-fit orbit for the planet is moderately eccentric ($e \approx 0.37$). This fit achieves a reduced $\chi^2 = 8.41$, with an RMS of 3.48 m s^{-1}. The expected jitter of HD 218566 (that is, the amount of jitter required to bring the reduced χ^2 of the best-fit solution to 1.0) is 3.23 m s^{-1}.

The top panel of Figure 4.4 shows the phased stellar reflex velocity of HD 218566 compared to the RV dataset. The middle panel shows the residuals to the 1-planet solution. The periodogram of the residuals to the best-fit solution, shown in the bottom panel, displays no strong peaks that would support the evidence for additional planets in the system.

4.6 HD 177830 (HIP 93746)

4.6.1 Stellar properties

HD 177830 is a V = 7.177 magnitude star of spectral class K0IV. Relative to the Sun, HD 177830 is quite metal-rich ([Fe/H] = 0.55).

HD 177830 is a subgiant with $M_v = 3.32$, close to giant status. The star has a known early M stellar companion with a projected separation of 97 AU (Eggenberger et al. 2007). It was first reported by Vogt et al. (2000) to host a 392-day Jovian-mass planet in an eccentric

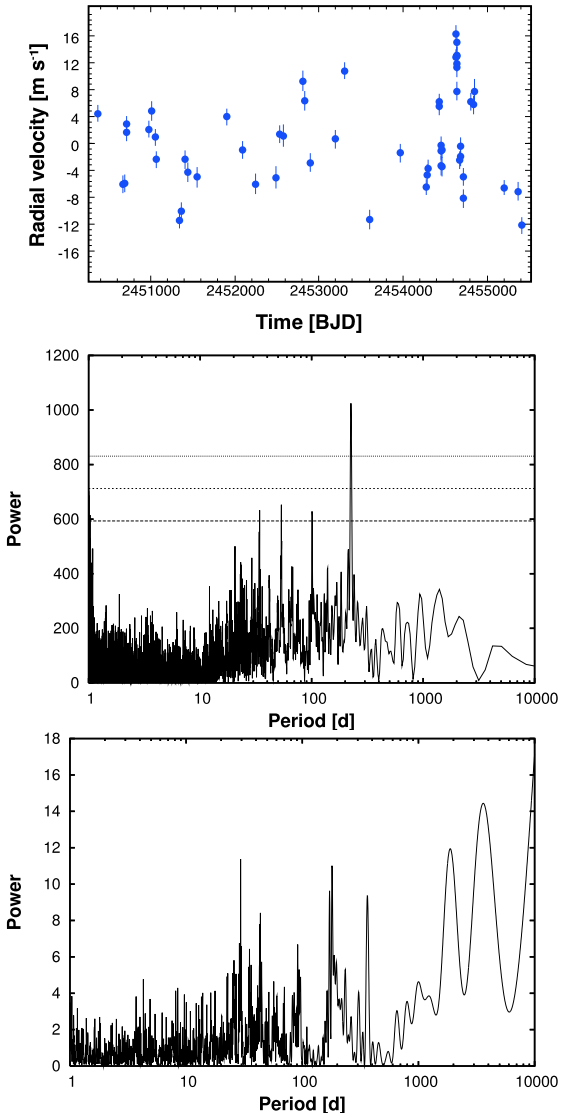

Figure 4.3: Radial velocity data and periodograms for HD 218566. *Top panel:* Relative radial velocity data obtained by KECK. *Middle panel:* Error-weighted Lomb-Scargle periodogram of the radial velocity data. *Bottom panel:* Power spectral window.

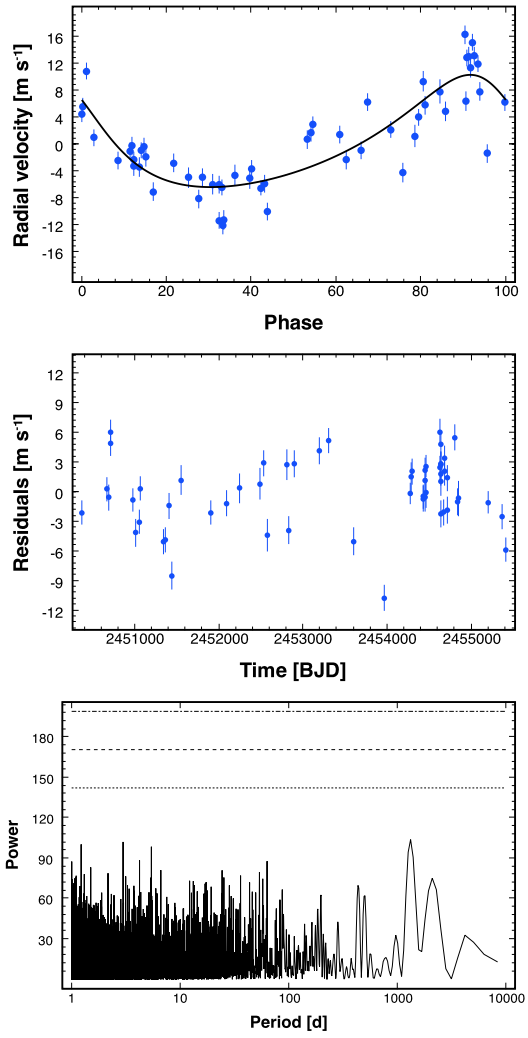

Figure 4.4: Keplerian solution and residuals periodogram for HD 218566. *Top panel:* Phased Keplerian fit. *Middle panel:* Residuals to the 1-planet Keplerian fit. *Bottom panel:* Periodogram of the residuals to the 1-planet best-fit solution.

(e=0.42) orbit. Updates to the orbit were provided by Butler et al. (2006). Wright et al. (2007) noted a possible 111-day or 46.8-day signal but suggested that it could be correlated noise. Tanner et al. (2009) studied the star using *Spitzer* to place limits on the amount of dust in the system, and concluded that no significant excess emission at 160 μm was detected (see also Trilling et al. 2008, Bryden et al. 2009).

The stellar parameters for this star listed in Table 4.1 are a compilation of various results, mostly from the SPOCS database Valenti & Fischer (2005) with additions from the NStED database. The values for the stellar mass in Table 4.1 are the lower and upper limits of the isochrone mass listed in the SPOCS database. We find a current $\log R'_{hk}$value of -5.37. HD 177830 has a derived rotation period of 65 days (Barnes 2001).

4.6.2 Keplerian solution

We show the 88 Keck radial velocity measurements in Table A.1, spanning approximately 15 years of RV monitoring. The median internal uncertainty for our observations is 1.05 m s^{-1}, and the peak-to-peak velocity variation is 87.15 m s^{-1}. The velocity scatter around the average RV in our observations is 24.68 m s^{-1}.

The individual RV observations for HD 177830 are shown in the top panel of Figure 4.5. The middle panel shows the error-weighted Lomb-Scargle (LS) periodogram of the full RV dataset. Finally, the lower panel of Figure 4.5 shows the spectral window. The strongest peak in the periodogram is well-fit with a Keplerian model with period 407.31 days, semi-amplitude $K = 31.17$ m s^{-1} and estimated FAP $< 3 \times 10^{-6}$. Together with the assumed stellar mass of 1.48 $\mathcal{M}_{\odot}$, this amplitude corresponds to a minimum mass of $\mathcal{M} \sin i = 1.48 \mathcal{M}_J$. The best-fit orbit for the planet is essentially circular. This 1-planet fit achieves a reduced $\chi^2 = 27.53$, with an RMS of 5.24 m s^{-1}. The top panel of Figure 4.6 shows the phased Keplerian fit for the 407-d planet.

The bottom panel of Figure 4.6 shows the periodogram of the residuals to the single-planet fit and the corresponding FAPs. The dominant peak at P = 110.98 with a FAP $\approx 5 \times 10^{-5}$ indicates the rather secure presence of an additional planet. Our best combined 2-planet fit indicates a new planet with $P = 110.91$ days, $K = 5.11$ m s^{-1} and a minimum mass of $\mathcal{M} \sin i = 0.15 \mathcal{M}_J$. The orbit of the second planet is moderately eccentric ($e \approx 0.36$). With this revised fit, we obtain a reduced $\chi^2 = 15.31$ and an RMS of the residuals of approximately 3.85 m s^{-1}. The expected jitter of HD 177830 (that is, the amount of jitter required to bring the reduced χ^2 of the best-fit solution to 1.0) is 3.71 m s^{-1}.

The top and 2nd panels of Figure 4.7 show the phased stellar reflex velocity of HD 177830 due to each companion as compared to the RV dataset. The 3rd panel shows the residuals to the 2-planet solution, while the bottom panel shows the periodogram of the residuals of the best-fit solution. No compelling peaks are evident in the current Keck dataset, indicating that the present data offers no strong support for additional planets in the system.

The 2-planet fit shows a very slight amount of dynamical interaction between planets b and c, which we accounted for in the modeling using the Bulirsch-Stoer integration scheme in the Systemic console (Meschiari & Laughlin 2010); we verified that the best-fit orbital model is stable for at least 10^6 years. The time evolution of the eccentricity is shown in Figure 4.8.

4.7 HD 99492 (HIP 55848)

4.7.1 Stellar properties

HD 99492 is a V = 7.383 magnitude star of spectral type K2V. A recent determination of many of its fundamental stellar parameters was given by Marcy et al. (2005) and is included in Table 4.1, supplemented with additional values from the NStED database. Marcy et al. (2005) found this star to be a middle-aged star of average chromospheric activity, with an age of 2-6

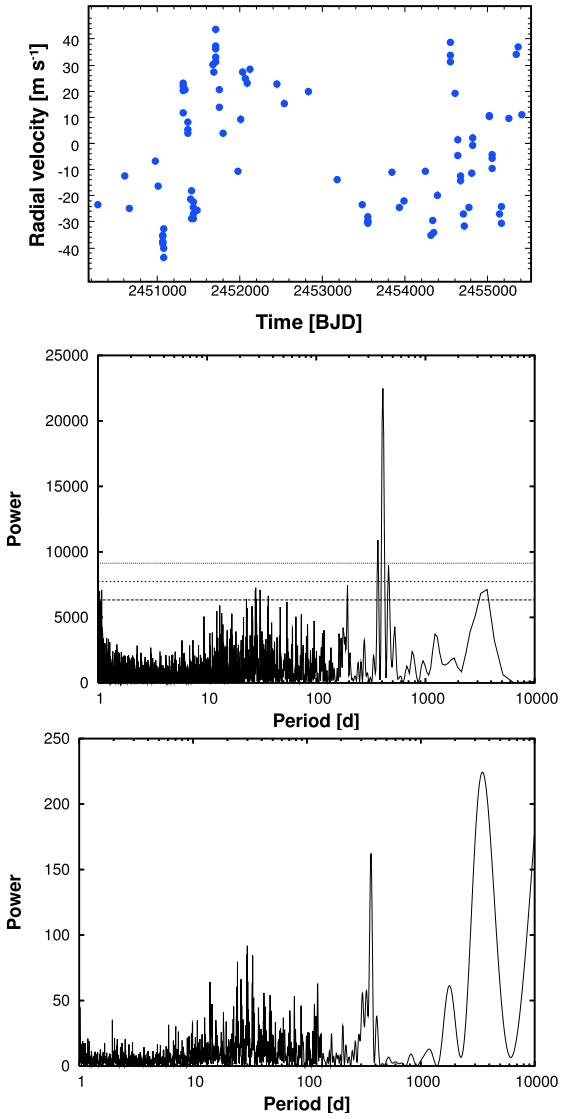

Figure 4.5: Radial velocity data and periodograms for HD 177830. *Top panel:* Relative radial velocity data obtained by KECK. *Middle panel:* Error-weighted Lomb-Scargle periodogram of the radial velocity data. *Bottom panel:* Power spectral window.

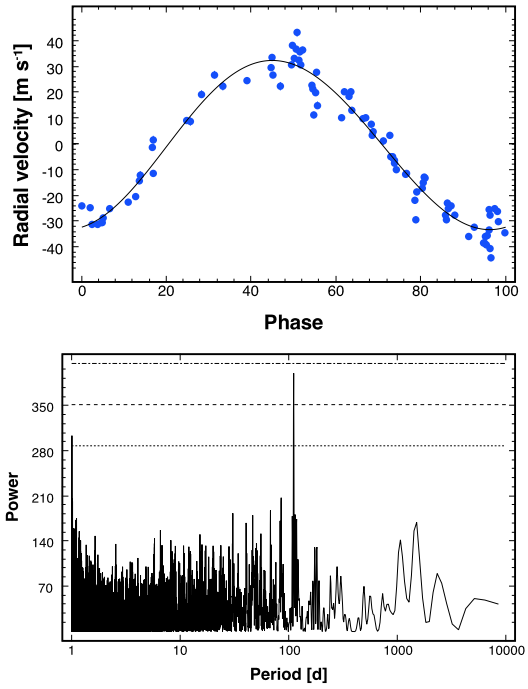

Figure 4.6: One-planet Keplerian solution and residuals periodogram for HD 177830. *Top panel:* Phased Keplerian fit. *Bottom panel:* Periodogram of the residuals to the 1-planet best-fit solution.

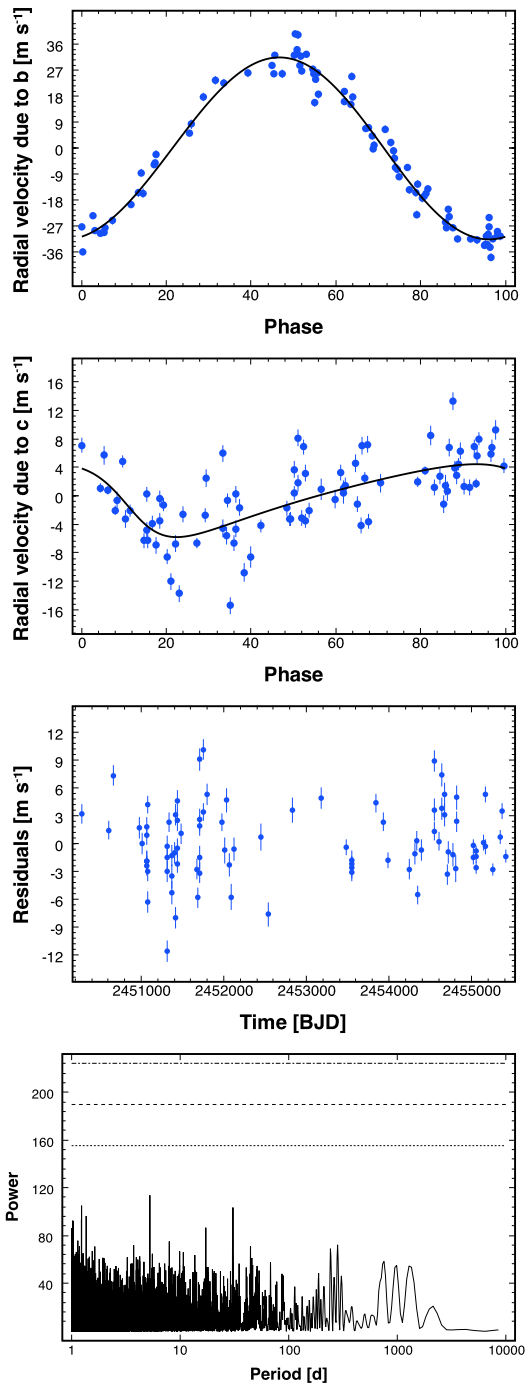

Figure 4.7: Keplerian solution and residuals periodogram for HD 177830. *1st panel:* Phased Keplerian fit of the 407-d component b. *2nd panel:* Phased Keplerian fit of the 111-d component c. *3rd panel:* Residuals to the 2-planet fit. *4th panel:* Periodogram of the residuals to the 2-planet best fit solution.

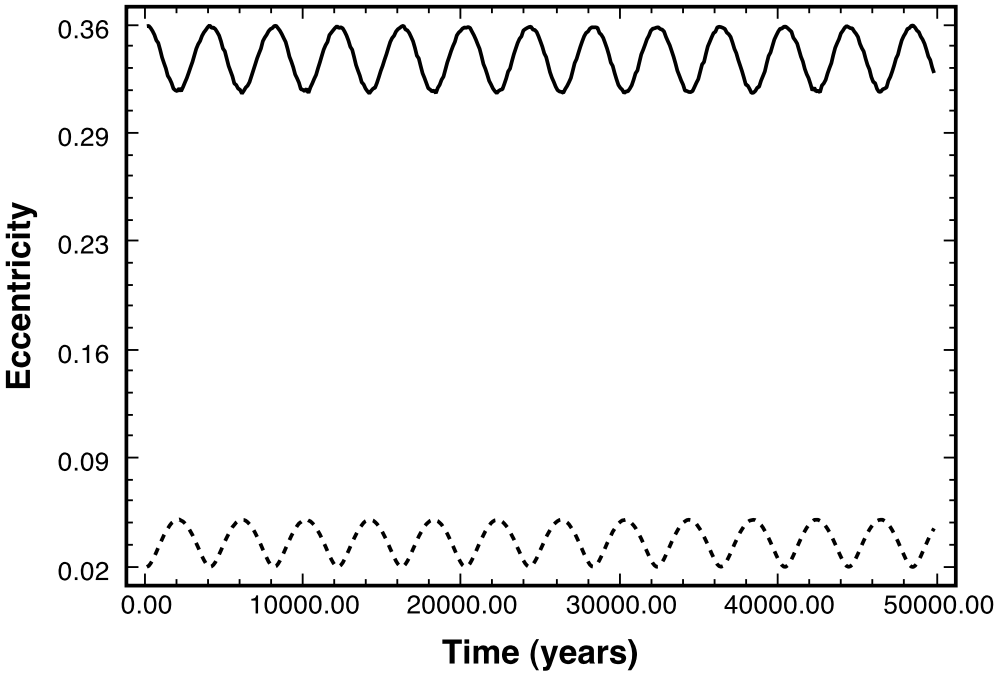

Figure 4.8: Eccentricity evolution of planets HD177830 b (dashed line) and c (solid line) within 5×10^4 years.

Gyr. They report an implied stellar rotation period of about 45 days (± 30%) based on the star's chromospheric activity index. Marcy et al. (2005) also reported a 17.1-day 36 $\mathcal{M}_{\oplus}$planet orbiting this star. Compared to the Sun, HD 99492 is quite metal-rich ([Fe/H] = 0.36).

4.7.2 Keplerian solution

Table A.1 shows the 93 relative radial velocity measurements for HD 99492. The radial velocity coverage spans almost 14 years of RV monitoring. The median internal uncertainty for our observations is 1.36 m s^{-1}, and the peak-to-peak velocity variation is 28.32 m s^{-1}. The velocity scatter around the average RV in our observations is 6.39 m s^{-1}.

The top panel of Figure 4.9 shows the individual RV observations for HD 99492. The middle panel shows the error-weighted Lomb-Scargle (LS) periodogram of the full RV dataset, while the bottom panel shows the spectral window. The FAP calculation for the strong Keplerian signal at $P = 17.06$ days in the RV dataset indicates an estimated FAP $< 3\times10^{-6}$. The dominant peak in the periodogram is well-fit by a Keplerian fit of period 17.05 days and semi-amplitude $K = 7.86$ m s^{-1}. Together with the assumed stellar mass of 0.83 $\mathcal{M}_{\odot}$, this amplitude suggests a minimum mass of $\mathcal{M} \sin i = 27.76\mathcal{M}_{\oplus}$. The best-fit orbit for the planet shows a small amount of eccentricity ($e \approx 0.13$). This 1-planet fit achieves a reduced $\chi^2 = 12.71$, with an RMS of 4.39 m s^{-1}. The top panel of Figure 4.10 shows the phased Keplerian fit for the 17-d planet, while the bottom panel shows the periodogram of the residuals to the single-planet fit and the corresponding FAPs.

The additional peak in the periodogram of residuals with P = 4908.67 reveals the secure detection of an additional planet, with a FAP $\approx 4 \times 10^{-4}$. Our best combined 2-planet fit suggests a new planet with $P = 4969.73$ days, $K = 4.88$ m s^{-1} and a minimum mass of $\mathcal{M} \sin i = 0.36\mathcal{M}_J$; the orbit of the second planet is somewhat eccentric ($e \approx 0.11$). Using this revised fit, we obtain a reduced $\chi^2 = 7.17$ and an RMS of the residuals of approximately 3.22

m s^{-1}. The expected jitter of HD 99492 (that is, the amount of jitter required to bring the reduced χ^2 of the best-fit solution to 1.0) is 2.94 m s^{-1}.

The top and 2nd panels of Figure 4.11 show the phased stellar reflex velocity of HD 99492 from each planet compared to the RV dataset. The 3rd panel shows the residuals to the 2-planet solution, while the bottom panel shows the periodogram of the residuals of the best-fit solution. No significant peaks are evident, indicating that the present data set offers no strong support for additional planets in the system.

4.8 HD 74156 (HIP 42723)

4.8.1 Stellar properties

HD 74156 is a V = 7.614 magnitude star of spectral type G1V. In comparison to the Sun, HD 74156 is modestly metal-rich ([Fe/H] = 0.13).

HD 74156 is a well-studied star, known already to have both a 52-day and a 2500-day planet (Naef et al. 2004). The star was claimed by Bean et al. (2008) to also harbor a 3rd planet ("d") at 336 days, in apparent support of the so-called "Packed Planetary Systems" hypothesis (PPS; Barnes & Raymond 2004). Indeed, Barnes & Greenberg (2007) cited the discovery of d as a successful prediction of the PPS hypothesis. However, the reality of HD 74516d was called into question by Baluev (2009) as a false detection made due to annual systematic errors in the HET RV data. Wittenmyer et al. (2009) also found no evidence of HD 74156 d in their follow-up study.

We have had HD 74156 under precise radial velocity monitoring at Keck for the past 8.9 years and here add 21 new velocities to the mix, combined with previously published data from CORALIE, ELODIE, and HET, bringing the total number of observations to 198. We re-analyzed the compound dataset from scratch, looking for evidence of further planetary com-

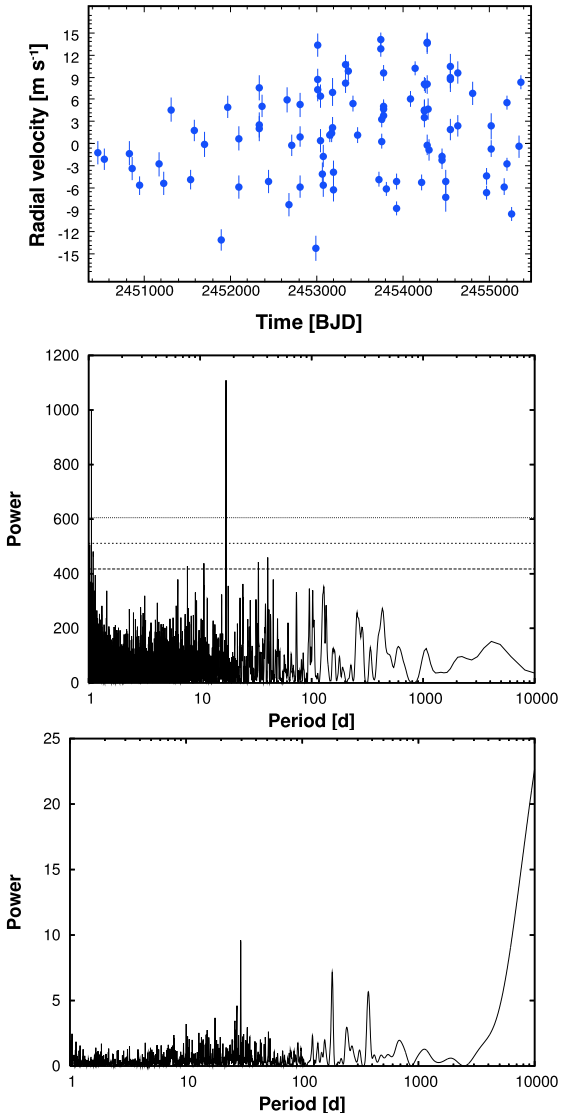

Figure 4.9: Radial velocity data and periodograms for HD 99492. *Top panel:* Relative radial velocity data obtained by KECK. *Middle panel:* Error-weighted Lomb-Scargle periodogram of the radial velocity data. *Bottom panel:* Power spectral window.

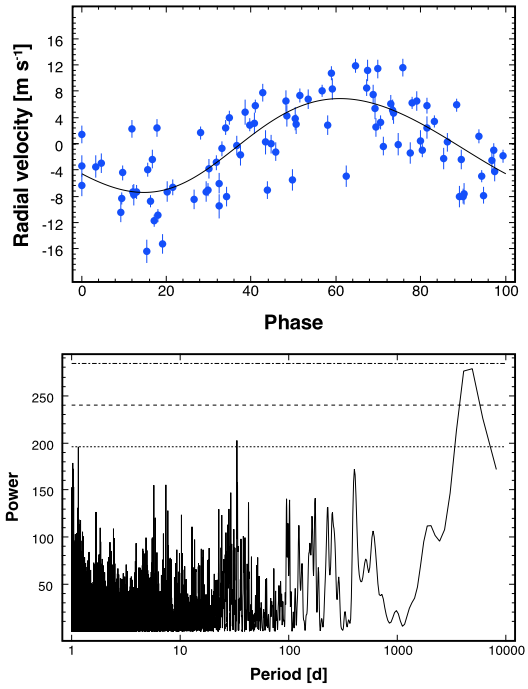

Figure 4.10: One-planet Keplerian solution and residuals periodogram for HD 99492. *Top panel:* Phased Keplerian fit. *Bottom panel:* Periodogram of the residuals to the 1-planet best-fit solution.

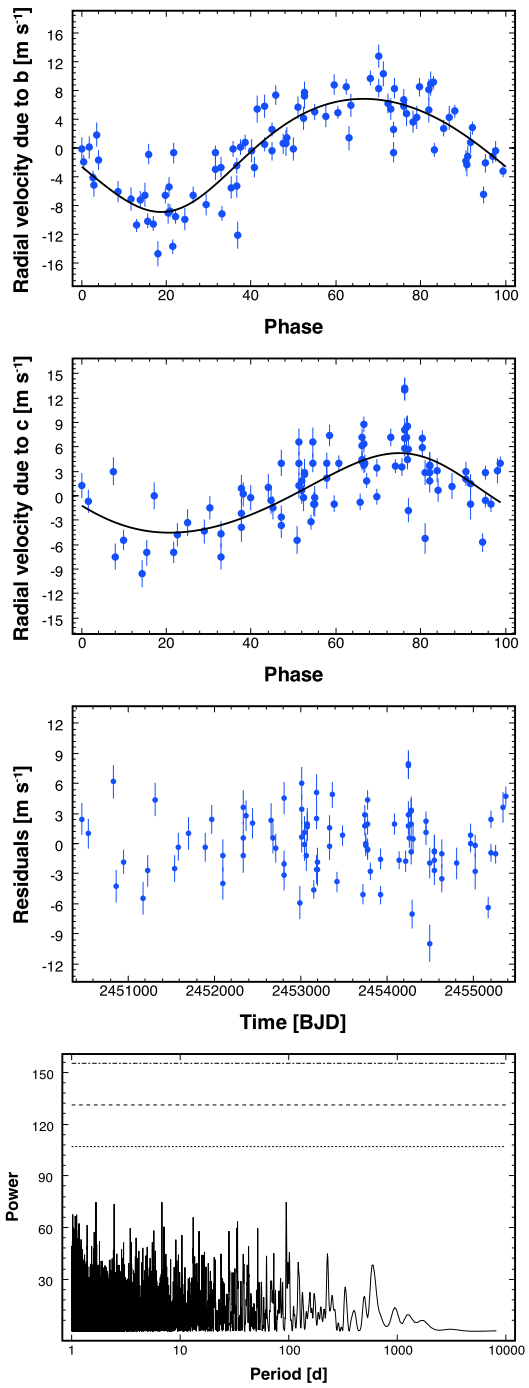

Figure 4.11: Keplerian solution and residuals periodogram for HD 99492. *1st panel:* Phased Keplerian fit of the 17-d component b. *2nd panel:* Phased Keplerian fit of the 4697-d component c. *3rd panel:* Residuals to the 2-planet fit. *4th panel:* Periodogram of the residuals to the 2-planet best fit solution.

panions. As usual, we allowed a floating offset between each data set in the Keplerian fitting process to compensate for the different zero-points of each observatory.

4.8.2 Keplerian solution

Table A.1 shows Keck/HIRES relative radial velocity observations for HD 74156. The radial velocity coverage spans almost 13 years of RV monitoring. The top panel of Figure 4.12 shows the individual RV observations for HD 74156 (CORALIE04, ELODIE04 Naef et al. (2004), HET09 Wittenmyer et al. (2009) and KECK; each RV dataset has been offset to yield the best-fit solution). The middle panel shows the error-weighted Lomb-Scargle (LS) periodogram of the full RV dataset. Figures 4.13 and 4.14 show the best 1-planet and 2-planet fits, respectively. The best 2-planet fit (derived using the full set of RV observations) obtains a reduced $\chi^2 = 3.09$, an RMS of the residuals of approximately 12.80 m s^{-1} and an expected jitter of 8.59 m s^{-1}. The value of the estimated jitter from this best-fit is considerably higher than the 2.2 m s^{-1} expected from its $\log R'_{hk}$ activity index. However, in this case the RMS is dominated by the CORALIE and ELODIE data, with a considerable contribution also from the HET data. The RMS of the fit using only the 29 Keck points is 3.5 m s^{-1} with jitter of 2.9 m s^{-1}, in much closer accord with the expected stellar jitter of 2.2 m s^{-1}.

The periodogram shown in the bottom panel of Figure 4.14, shows no compelling peaks in the residuals, indicating that the present data set offers no significant support for additional planets in the system. Our results confirm the conclusions of Wittenmyer et al. (2009). The expanded dataset presented in this paper does not support the theoretical and observational evidence for a third planetary companion claimed by Bean et al. (2008).

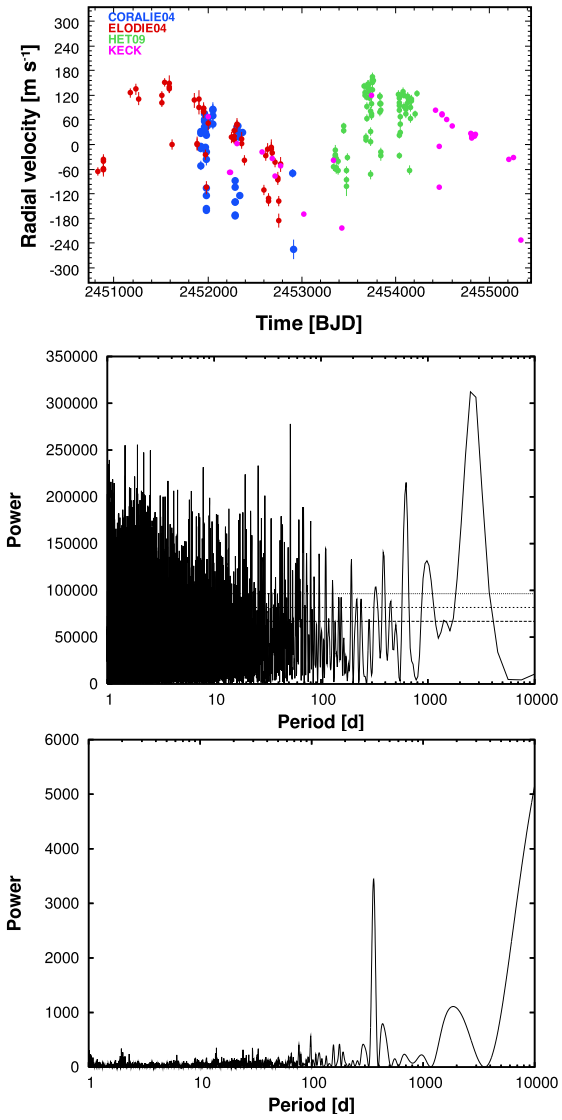

Figure 4.12: Radial velocity data and periodograms for HD 74156. *Top panel:* Relative radial velocity data obtained by CORALIE04, ELODIE04, HET09 and KECK. *Middle panel:* Error-weighted Lomb-Scargle periodogram of the radial velocity data. *Bottom panel:* Power spectral window.

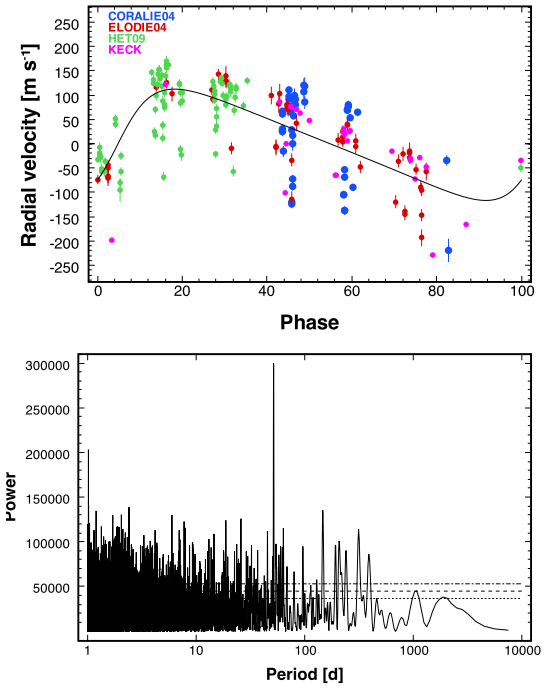

Figure 4.13: One-planet Keplerian solution and residuals periodogram for HD 74156. *Top panel:* Phased Keplerian fit. *Bottom panel:* Periodogram of the residuals to the 1-planet best-fit solution.

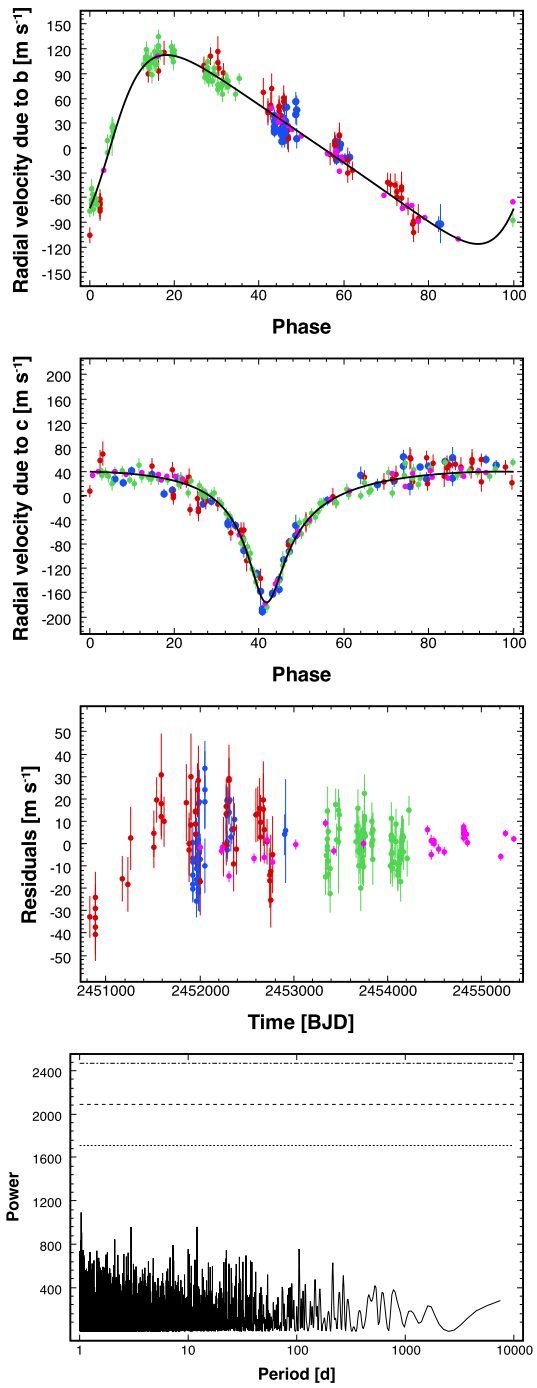

Figure 4.14: Keplerian solution and residuals periodogram for HD 74156. *1st panel:* Phased Keplerian fit of the 52-d component b. *2nd panel:* Phased Keplerian fit of the 2514-d component c. *3rd panel:* Residuals to the 2-planet fit. *4th panel:* Periodogram of the residuals to the 2-planet best fit solution.

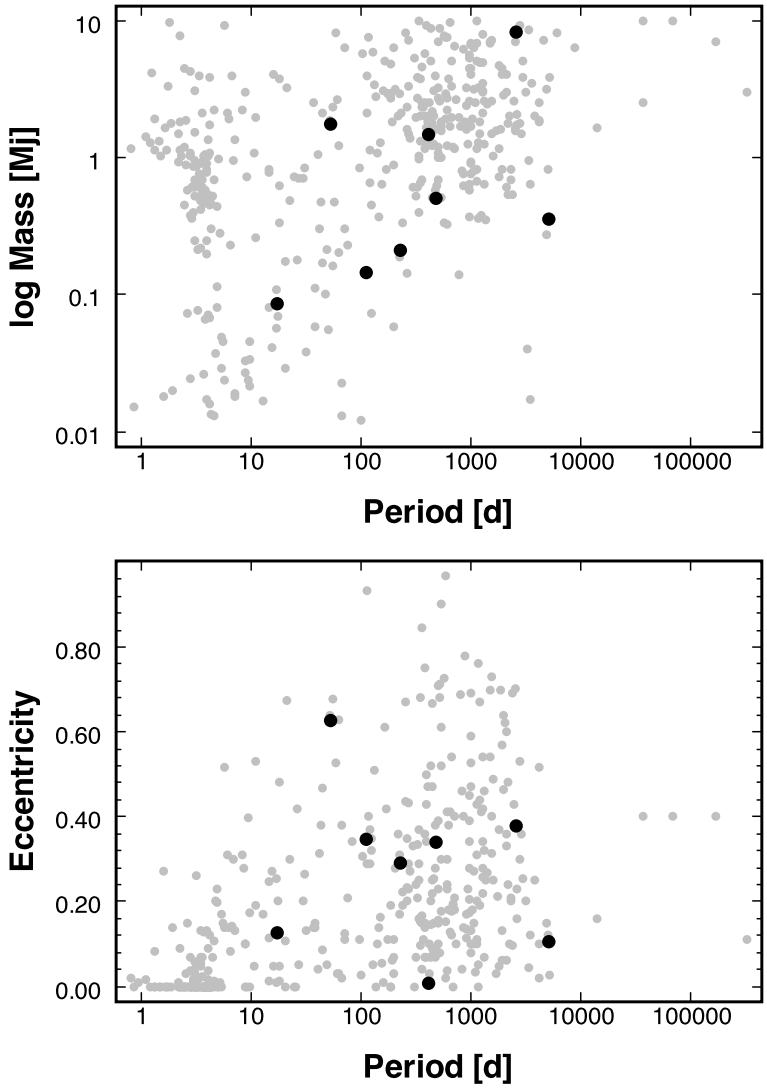

Figure 4.15: Plot of all known extrasolar planets (gray dots) and the orbital elements of all the planets orbiting the host stars presented in this paper (black points).

4.9 Conclusions

The five systems presented in this paper add to the ever-growing list of single and multiple-components exoplanetary systems.

Two of the systems, namely, HD 31253 and HD 218566, are well-characterized Saturn-mass planets in $\approx$ 1-year orbits. For both systems, the data presented in this paper do not show prominent peaks in the periodogram of residuals, even at a 10% FAP level. While several single-planet systems with similar properties have later been characterized with an additional outer, long-period companion (e.g. Jones et al. 2010), the absence of any significant linear trend in the current data seem to rule out the presence of additional Jupiter-mass planets with $P <$ 40,000 days.

HD 99492 and HD 177830 each gain a new planetary companion, adding to the previously known planets (Vogt et al. 2000, Marcy et al. 2005). The known linear trend in the residuals to HD 99492 b is now fully characterized thanks to the longer phase coverage, indicating the presence of a Saturn-mass planet on a $\sim$5,000-day orbit.

The RV data we collected for HD 177830 support the existence of an additional inner planet, presenting an interesting case. The planets in this system are within a binary with a separation of approximately 97 AU (Eggenberger et al. 2007). Simulations of the formation and stability of planets in binary star systems imply that the perturbative effect of the secondary star will be negligible in binaries with separation larger than 100 AU. The binary system of HD 177830 is slightly below this limit. This system is also the first binary with a moderate separation in which multiple planets have been discovered. Although it is unlikely that the low-mass secondary star of this system has had significant effects on the formation of planets around the primary, it would still be interesting to study how planets in this system formed and migrated to their current stable orbits.

Finally, we analyzed an expanded dataset of Doppler observations of HD 74156, adding 21 Keck RV points to the known data. We repeated the analysis looking for evidence of a third planet, which would lend observational credence to the predictions of the PPS hypothesis (e.g. Barnes & Raymond 2004). Our dataset does not show support for the claimed HD 74156 d planetary companion. Indeed, the residuals periodogram to our best 2-planet fit do not exhibit any promising peaks for future RV follow-ups, strengthening the conclusions of Wittenmyer et al. (2009).

All the planets presented in this paper lie well within the existing exoplanet parameter envelopes (Fig. 4.15). Several of them lie in the so-called "desert" in the mass and semi-major axis distribution of extrasolar planets (Ida & Lin 2004). Monte-Carlo population synthesis models for extrasolar giant planet formation tend to suggest that planets migrate relatively rapidly through the period range between 10 and 100 days, and, in addition, often grow quickly through the mass range centered on the Saturnian mass. In the context of the overall planetary census, these four new planets help to further elucidate the various statistical properties of exoplanets. In particular, the discovery of multiple-planet systems helps in further characterizing the number of stars hosting multiple planetary companions and any correlations emerging in the distribution of orbital elements as suggested by observational clues (e.g. Wright et al. 2009).

Chapter 5

The Potential Impact of Groove Modes on Type II Planetary Migration

5.1 Abstract

In this letter, we briefly describe the evolution of a variety of self-gravitating polytropic protoplanetary disk models that contain annular *grooves* (e.g. gaps) in their surface density profiles. These grooves are inspired by the surface density gaps that are presumed to open in response to the formation of a giant planet. Our work provides an extension of the previously studied *groove modes* that are known in the context of stellar disks, in which the density response corotates approximately with the groove minimum. The emergence of nonaxisymmetric gravitational instabilities (GI) is predicted via a generalized eigenvalue code that performs a linear analysis; the instabilities are confirmed and studied with nonlinear hydrodynamical simulations. We find the presence of a groove drives a fast-growing two-armed mode in moderately massive disks, and extends the importance of self-gravitating instabilities down to lower disk masses than for which they would otherwise occur. We discuss the potential importance of this

instability in the context of planet formation, e.g. the modification of the torques driving Type II migration.

5.2 Introduction

The theory of giant planet formation has evolved very rapidly over the past decade, and the now near-paradigmatic core accretion theory (e.g. Pollack et al. 1996) has been greatly refined and endowed with a variety of physical inputs (see, e.g. Alibert et al. 2004, Hubickyj et al. 2005). It is now generally accepted that Jupiter-mass planets grow by initially accumulating 5-10 $M_{\oplus}$ cores, which then accrete large quantities of gas from the surrounding nebula. During the phase of rapid gas accretion, the growing Jovian planet opens a gap in the disk and its orbit subsequently evolves via the process of Type II migration (Lin et al. 1996, Papaloizou et al. 2007).

A competing theory (e.g. Boss 2000) holds that giant planets such as Jupiter fragmented directly from the nebula as a result of gravitational instabilities. This mechanism may account for some of the observed extrasolar planets, but it has a number of difficulties if invoked to account for the full population. In particular, it fails to explain the observationally well established planet-metallicity relation (Santos et al. 2003, Valenti & Fischer 2005). Another criticism is that gravitational instability requires the Toomre Q parameter, $Q = \kappa c_s / \pi G \sigma$, to be of order unity at some radius in the disk. This, however, generally requires rather massive disks, $M_D / M_{star} \gtrsim 0.1$, which are not often observed.

Global gravitational instability depends not just on disk mass and sound speed, but also on the density profile of the disk. As has been shown by Toomre (1981), a sharp density gradient can provide a mechanism for maintaining a wave cycle that leads to instability and subsequent destruction of steep density gradients, i.e. "edges". Analogously, Sellwood & Lin

(1989) described a family of gravitational instabilities in stellar disks dubbed *groove modes* which comprise fast-growing disturbances driven by narrowly defined structures in particle angle-action space. These features, for collisionless stellar disks, correspond to narrow surface density depressions; groove modes are thus akin to the edge mode in that they are driven by steep density gradients at corotation. Sellwood and Lin further noted that groove modes could be excited and maintained by a feedback cycle. This cycle kicks in when a slowly-growing inner edge mode carves a groove by scattering particles in a narrow range at its outer Lindblad resonance, creating a fast-growing groove mode. The appearance of a groove gives rise to further groove modes once it scatters particles at its own Lindblad resonance.

This feedback cycle relies on the wave-particle interaction at the resonances, and thus cannot be immediately realized in a gaseous disk. The groove mode may have relevance, however, in the protoplanetary context: theoretical considerations (Lin & Papaloizou 1979, Goldreich & Tremaine 1980, Lin & Papaloizou 1993), numerical simulations (e.g. Takeuchi et al. 1996, Bryden et al. 1999) and tentative observational indications (Setiawan et al. 2008) point to the fact that, under appropriate circumstances, massive planets can resonantly drive trailing waves that transport angular momentum and open a "gap" in the disk. The detailed process of opening and maintaining the gap depends on the balance between the angular momentum flux resulting from spiral waves driven by the planet and that originating from the viscosity of the disk. When the planet is sufficiently massive and the viscosity is low enough, a stable surface density groove is carved on the disk. A growing Jovian-mass planet naturally maintains a surface density gradient.

In this letter, we open an investigation into the possibility that the planet-induced presence of a surface density gap can drive a fast-growing, self-gravity induced groove mode in a massive disk, sidestepping the problems of carving a groove in the first place and providing a mechanism for maintaining the amplifier. We support our hypothesis with both a numerical

linear analysis (see, e.g. Adams et al. 1989) and a full hydrodynamical simulation (following Laughlin & Rozyczka 1996) of a disk with an imposed groove in surface density, as inspired by previous numerical investigations for stellar disks (e.g. Sellwood & Kahn 1991). We span a wide range of disk/star mass ratios to assess the relevance of this GI to the realistic disk masses observed.

5.3 Procedure

We employ a two-dimensional hydrodynamical grid code for following the evolution of a thin, self-gravitating disk. The continuity and Euler equations in polar coordinates are solved using a second-order van Leer type scheme, coupled with time stepping that is first-order accurate. The basic difference equations are given in Stone & Norman (1992). The self-gravity of the disk is obtained by applying the Fourier convolution theorem to the potential dictated by the Poisson equation (Binney & Tremaine 1987). The details of the hydrodynamical code are described in Laughlin et al. (1997) and related papers.

We adopt the following parametrization for the surface density of the disk:

$$\sigma(r) = \sigma_0 e^{\left[-(r-R_0)^2/w\right]} \times \left(1 - \frac{A\Delta^2}{(r-R_P)^2 + \Delta^2}\right), \tag{5.1}$$

which represents a Gaussian profile multiplied by a Lorentzian profile of depth A, characteristic semi-width Δ and central position R_P; for $A = 0$, this profile is the "reference disk" considered by Laughlin & Rozyczka (1996). The disk model used throughout this letter has no pretense of actually representing a protoplanetary disk faithfully, but has the advantage of possessing a single $m = 2$ mode that is very clearly identifiable both in semianalytic calculations and in the nonlinear simulations. The choice of a Lorentzian profile to represent the gap is arbitrary as well, and follows Sellwood & Kahn (1991).

We take $w = 0.03$, $R_0 = 0.25$ and an inner disk edge of 0.05. We assume a polytropic equation of state, $P = K\sigma^\gamma$ with the polytropic exponent $\gamma = 2$. Again, this model is chosen largely for illustrative purposes, and allows us to avoid an energy equation. The characteristic width Δ is meant to represent a typical gap width; the chosen value of 0.07 can be derived from the approximate scaling

$$2\Delta/r_p \sim 0.29 q^{2/3} \mathcal{R}^{1/3}, \tag{5.2}$$

(e.g. Varnière et al. 2004) with $\mathcal{R} \approx 5 \times 10^5$ and $q = 2 \times 10^{-3}$. The set of units used in the code takes the outer grid radius R_D and the gravitational constant G equal to unity and $M_* = 0.5$.

To quantify the strength, pattern speed and growth rate of each spiral mode, we compute the Fourier decomposition of the surface density, defined as

$$a_m = \frac{1}{2\pi} \int_0^{2\pi} \sigma(r, \Phi) e^{-im\Phi} \mathrm{d}\Phi, \tag{5.3}$$

for a mode number m. The local growth rate (e-folding time) of a disk mode is given by

$$\gamma_m(r) = \frac{d}{dt} \log \frac{a_m}{a_0} = \frac{d}{dt} \log c_m, \tag{5.4}$$

while the phase of a disturbance is defined as

$$\Phi_m(r) = \tan^{-1} \left[\frac{\mathrm{Im}(-a_m)}{\mathrm{Re}(a_m)} \right]. \tag{5.5}$$

The local pattern speed is then given by $\Omega_P = (1/m)\dot{\Phi}_m$. Finally, a global measure of the growth of a particular mode is given by integrating the m-th Fourier amplitude a_m over the radial range and normalizing to the azimuthal average of the surface density:

$$C_m = \left| \frac{\int_{R_i}^{R_D} a_m(r) dr}{\int_{R_i}^{R_D} a_0(r) dr} \right|. \tag{5.6}$$

The growth rate and pattern speed that emerge from the hydrodynamical simulation are checked against a linear numerical analysis code we developed, as described e. g. in Laughlin

Model	q_D	A	Q_{min}	m	γ_{lin} ($\bar{\gamma}_{nl}$)	Ω_P ($\bar{\Omega}_P$)
1	1	0	1.21	2	1.21 (0.90)	2.78 (2.69)
2	0.63	0.90	0.67	2	2.31 (2.14)	3.41 (3.37)
3	0.32	0.90	1.31	2	1.43 (1.16)	3.18 (3.05)
4	0.16	0.90	1.92	2	0.73 (0.65)	3.04 (3.00)
5	0.13	0.90	2.03	2	0.56 (0.50)	3.02 (2.89)
6	0.08	0.90	2.24	2	($0.28^{a,c}$)	(-0.14^{c}) [1]
7	0.06	0.90	2.76	2	[2]	
12	0.63	0	1.30	2	0.84 (0.70)	2.27 (2.22)
13	0.32	0	1.52	2	0.37 (0.16, 0.31)	2.03 (2.22)
14	0.16	0	1.86	2	[2]	
15	0.13	0	2.08	2	[2]	
16	0.08	0	2.26	2	[2]	
17	0.06	0	2.65	2	[2]	

Table 5.1: The table lists growth rate (γ_{lin}, $\bar{\gamma}_{nl}$) and pattern speed (Ω_P, $\bar{\Omega}_P$) as measured respectively by the linear code and the full hydrodynamical simulation for the various disk masses ($q_D = M_D/M_{star}$) and groove depths (A) considered. [1] This mode has two linear phases (a, b) and two saturation phases (c, d). During phase b the mode is counterrotating and leading; at saturation, the mode reverses its rotation. The growth rates reported are measured from the hydro simulation. [2] These models do not show appreciable mode growth in either the linear or the fluid simulation.

et al. (1997), which solves a matrix equation akin to a generalized eigenvalue problem; the solution is valid in the linear regime and yields a complex eigenvalue, which indicates the pattern speed Ω_P and growth rate γ, and a complex eigenvector, which describes the radial variation and local spiral phase angle of the mode. Comparison with the full nonlinear simulations enables us to check the consistency and accuracy of the two independent approaches.

5.4 Computer simulations

Table (5.1) lists the disk models considered in this letter. We have first set up a "base" disk with surface density given by Equation 5.1, with $A = 0$, $q_D = M_D/M_{star} = 1$ and $Q_{min} = 1.21$ (Model 1); this sets the normalization constant σ_0 and the polytropic constant K. The equilibrium was disrupted with a random density perturbation of order 0.001 $\sigma(r)$. The grid covers the polar coordinates (r, φ) with 256 logarithmically spaced zones in radius and 256

equally spaced azimuthal zones. Each model is evolved for at least 100 time units, although the reflective boundaries muddle the nonlinear evolution once the wave reaches the outer part of the disk. Figure (5.3) shows the evolution of the surface density normalized to the azimuthal average $\Sigma(r) = \log(\sigma(r)/\bar{\sigma}(r))$. In accordance with the previous investigations and with the output of our linear code, the base disk is unstable to a single two-armed ($m = 2$) "grand-design" spiral mode. The spiral mode grows in the linear regime for the first few dynamical times, and within about 10 dynamical times it visibly perturbs the outer edges of the disk. After a few more dynamical times, the spiral pattern has reflected off the boundaries and has propagated back into the densest regions of the disk. The normalized amplitude C_2 shows that the dominant two-armed mode grows at an exponential rate (linear regime) until stabilizing around a constant amplitude (mode saturation). These phases are shown in Figure 5.2. Note that for our purposes, the linear growth rate is the primary quantity of interest. The dashed linear slope is derived from the mode analysis for the same disk parameters, and agrees well with the hydrodynamical code. The small discrepancies between growth speeds can be traced to the effective softening given by the FFT-based solution scheme for the Poisson equation.

A second set of disk parameters (Model 2) including a surface density *groove* was set up, with $A = 0.90$ (a 90% dip in surface density), $\Delta = 0.07$ and $R_P = 0.4$. Maintaining the same normalizations for density and pressure as above, the disk has the same surface density profile sufficiently far from the groove, but a smaller disk-to-star mass ratio, $q_D = 0.63$. The resulting Toomre Q profile is shown in Figure (5.1). By visual inspection of Figure (5.3) and the slope of the normalized Fourier amplitude in Figure (5.4), it is clear that the presence of the groove drives a far more violently growing instability. We then repeated the experiment varying the surface normalization to yield $q_D = 0.32$, 0.16, 0.13, 0.08, and 0.06 (Models 3-11).

Measuring the pattern speed of the spiral is slightly more difficult, since the pattern rotates only approximately in a rigid fashion. We thus calculate a "global" measure $\bar{\Omega}_P$ by

weighing the local $\Omega_P(r)$ (eq. [5.3]) with the local density enhancement $|c_m|$:

$$\bar{\Omega}_P = \frac{d}{dt}\left(\frac{\int \Phi_m(r)\exp(|c_m|)dr}{\int \exp(|c_m|)dr}\right), \tag{5.7}$$

so that the densest parts of the spiral contribute the most to the pattern speed. The spiral pattern's corotation radius is found to lie within the gap.

Since the presence of the groove diminishes the q_D parameter for a given density normalization, we also set up a series of base disks (Models 12-17) with a surface density normalization chosen so that its mass would equal that of Models 2-7. The evolution of the normalized $m = 2$ mode amplitude is shown in Figure (5.4). For a given q_D, in the presence of the groove the $m = 2$ mode exponentiates about 3 times faster than the base disk. Models 14-17, despite having equal disk mass and lower Q_{min} than their groovy counterparts, do not show an exponentially growing phase during the duration of the simulation. A growing groove mode is detectable down to $q_D = 0.08$ (Model 6), but does not show a resolvable exponential phase for $q_D = 0.06$ (Model 7). The $m = 2$ groove instability in Model 6 is growing about as fast as Model 13, which is four times as massive.

Figure (5.5) shows the evolution of the azimuthally averaged density profile for the two lowest-mass unstable models (Models 5 and 6); the surface density groove is filled in by the growing spiral modes, as shown by the time evolution of the surface density at the center of the gap. An approximate estimate for the effective "alpha"-type viscosity coefficient (Shakura & Sunyaev 1973) is derived by a procedure similar to that employed in Laughlin & Rozyczka (1996), although the effective viscosity given by gravitational instability is not too well characterized by a local prescription. We solve the time evolution given by the diffusion-type equation for surface density and compare it with the surface density evolution in the hydrodynamical simulation, once the spiral pattern has established itself. This simple estimation yields $\alpha \sim 0.16$ for $q_D = 0.13$ and $\alpha \sim 0.04$ for $q_D = 0.08$, and agrees approximately with the timescale for closing the gap by

viscous diffusion.

5.5 Discussion and conclusion

In this letter, we have found that disk self-gravity may play a significant and as-yet largely unstudied role in disks in which a planet has opened and is maintaining an annular gap in the surface density profile of the disk. Gravitational torques from massive protoplanets necessarily impart a surface density gap in a disk, and the formation of a gap provides the structure needed both for a feedback amplifier (e.g. Toomre 1981) as well as for the groove mode (Sellwood & Lin 1989). In essence, a gap provides a pressure gradient which can locally reduce the effectiveness of the epicyclic frequency in stabilizing the disk against its own self gravity, thus allowing instability at low surface densities. In the absence of a perturbing planet, the nonlinear outcome of a groove instability would be to destroy the sharp density gradient that promoted the instability in the first place. In a planet-forming disk, however, the embedded Jovian planet will exert torques whose net effect is to maintain the gap. The competition between the GI-induced spiral torques and the planetary torques may thus lead to a significant modification of the criterion for gap opening, which in turn can have a significant effect on the resulting migration of the protoplanet. We have found that this effect is likely to be relevant even when the overall disk mass is lower than the $q_D > 0.1 - 0.2$ value at which significant gravitational spiral instabilities are generally thought to occur (see, e.g. Shu et al. 1990, Laughlin & Rozyczka 1996, Boss 1997). By comparison, the typical mass within 30 AU assumed for the Minimum Mass Solar Nebula yields $q_D \approx 0.01$ (this likely underestimate the actual mass of the solar nebula by at least a factor of 3). Further afield, Andrews & Williams (2005) surveyed 153 young stellar objects in the Taurus Aurigae star-forming complex, and found a median disk mass of $q_D = 0.5\%$. While these disks span a variety of ages, and show a variety of masses, it is not clear

how massive the average protoplanetary disks is at the time when a massive protoplanetary core enters the rapid gas accretion phase, and whether the mass might be enough to trigger the class of instability studied here. It must also be kept in mind that while the idealized disks in the simulations shown here display no instability for $q_D < 0.08$, the limited numerical resolution and high intrinsic numerical viscosity allows us to identify only modes with intrinsically rapid growth rates. Further work with more realistic disk models is required to find the true minimum mass for the instability. We are eager to continue this analysis by (1) including the planetary potential in both our linear analysis and in our nonlinear simulations, (2) carrying out the simulations at higher numerical resolution, and (3) adopting more realistic disk models.

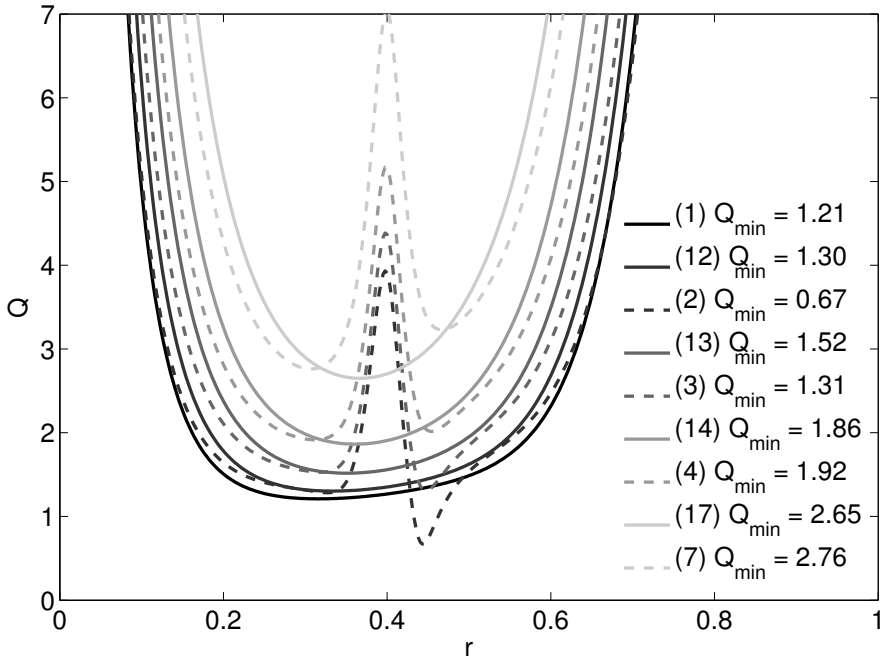

Figure 5.1: Toomre $Q = \kappa c_s / \pi G \sigma$ profiles for the disk models considered (dashed lines: models with a groove, solid: models without a groove). Like colors correspond to equal q_D.

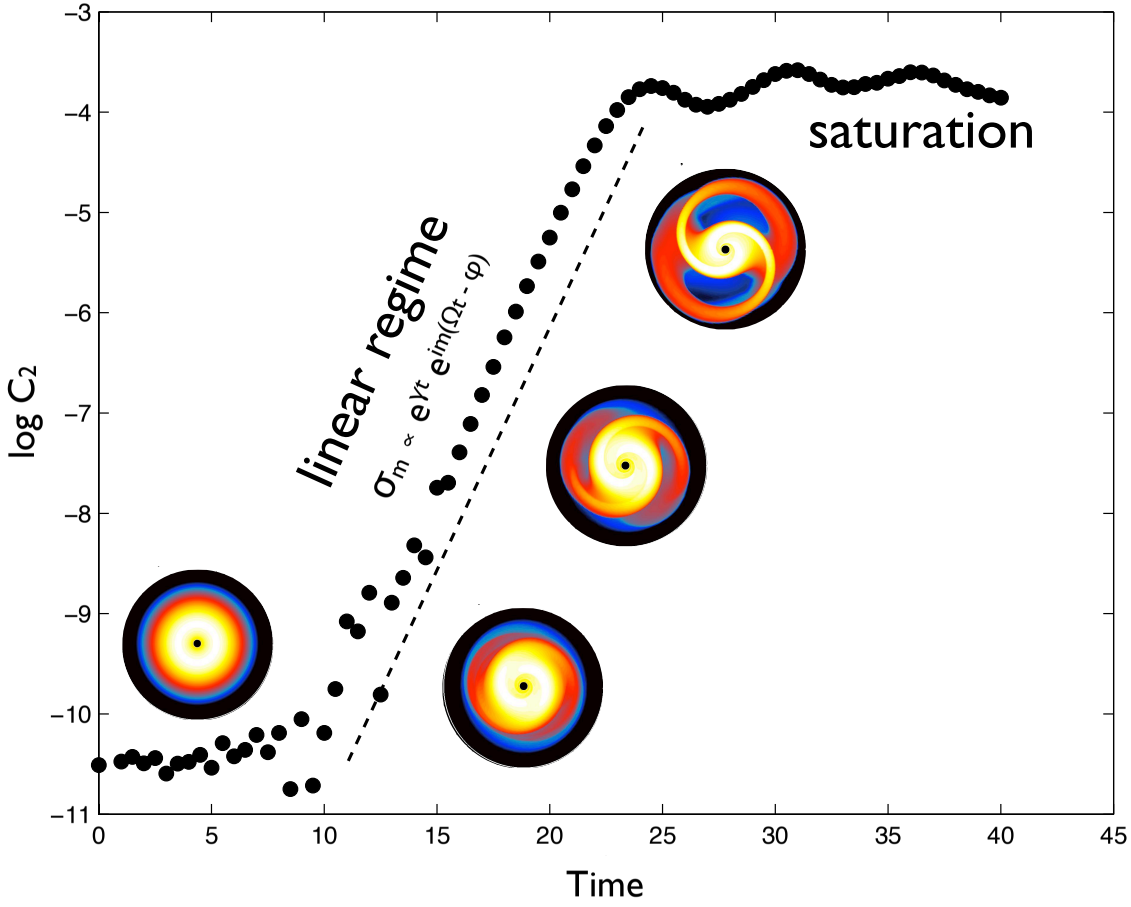

Figure 5.2: Sketch of the evolution of the disk instability.

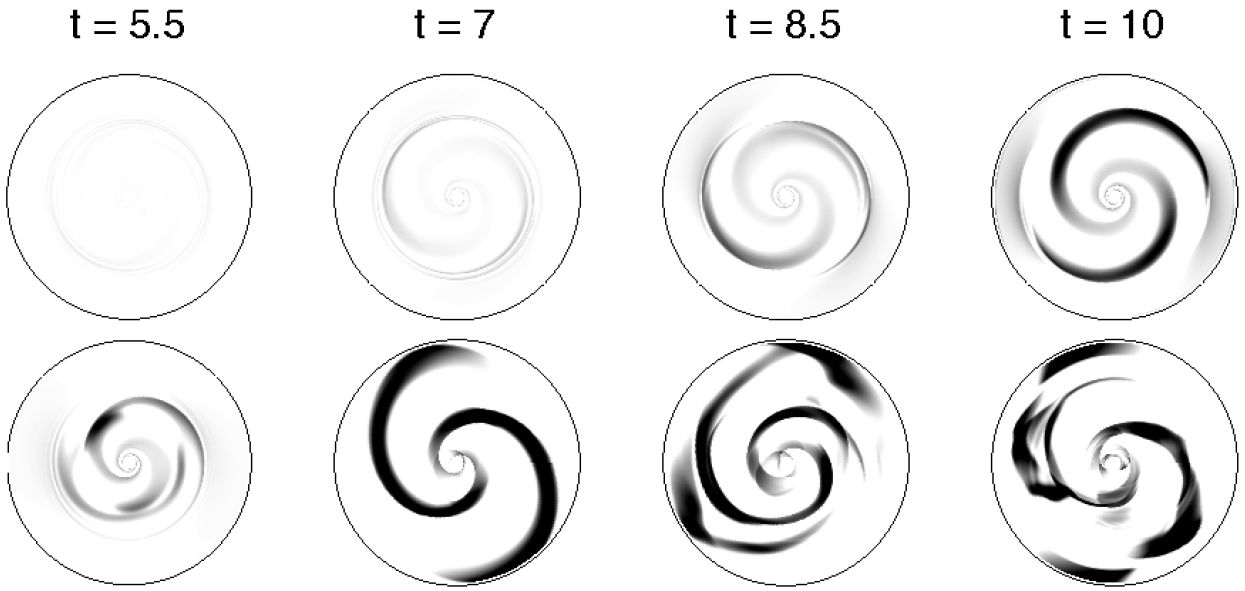

Figure 5.3: Surface overdensity Σ evolution for Models 1 and 2.

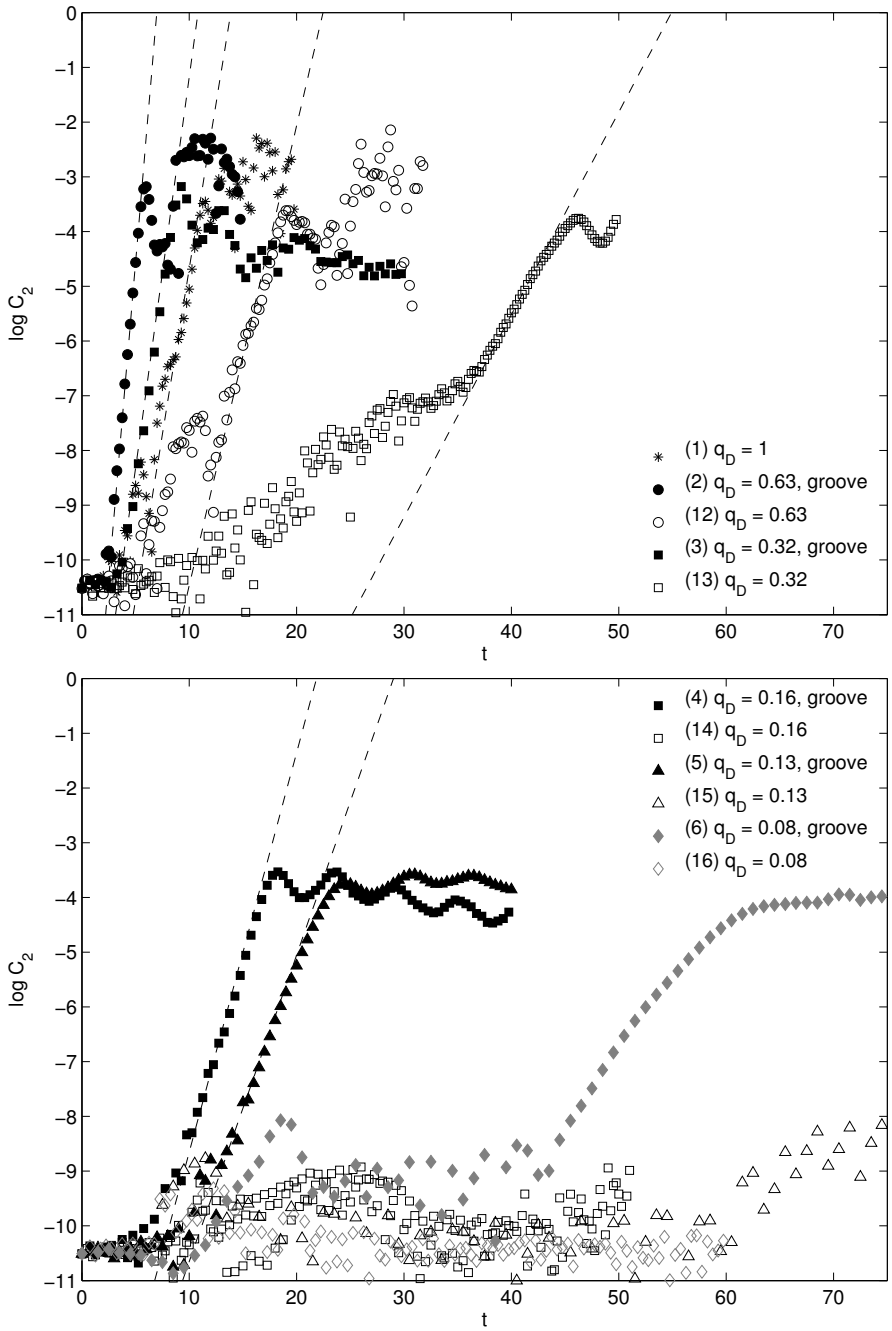

Figure 5.4: Top panel: normalized amplitudes of the $m = 2$ mode for disk models 1-3, 12, 13. Bottom panel: normalized amplitudes of the $m = 2$ mode for disk models 4-6, 14-16. The predicted growth rate of a mode, when resolved by our linear analysis code, is indicated by the slope of the dashed lines.

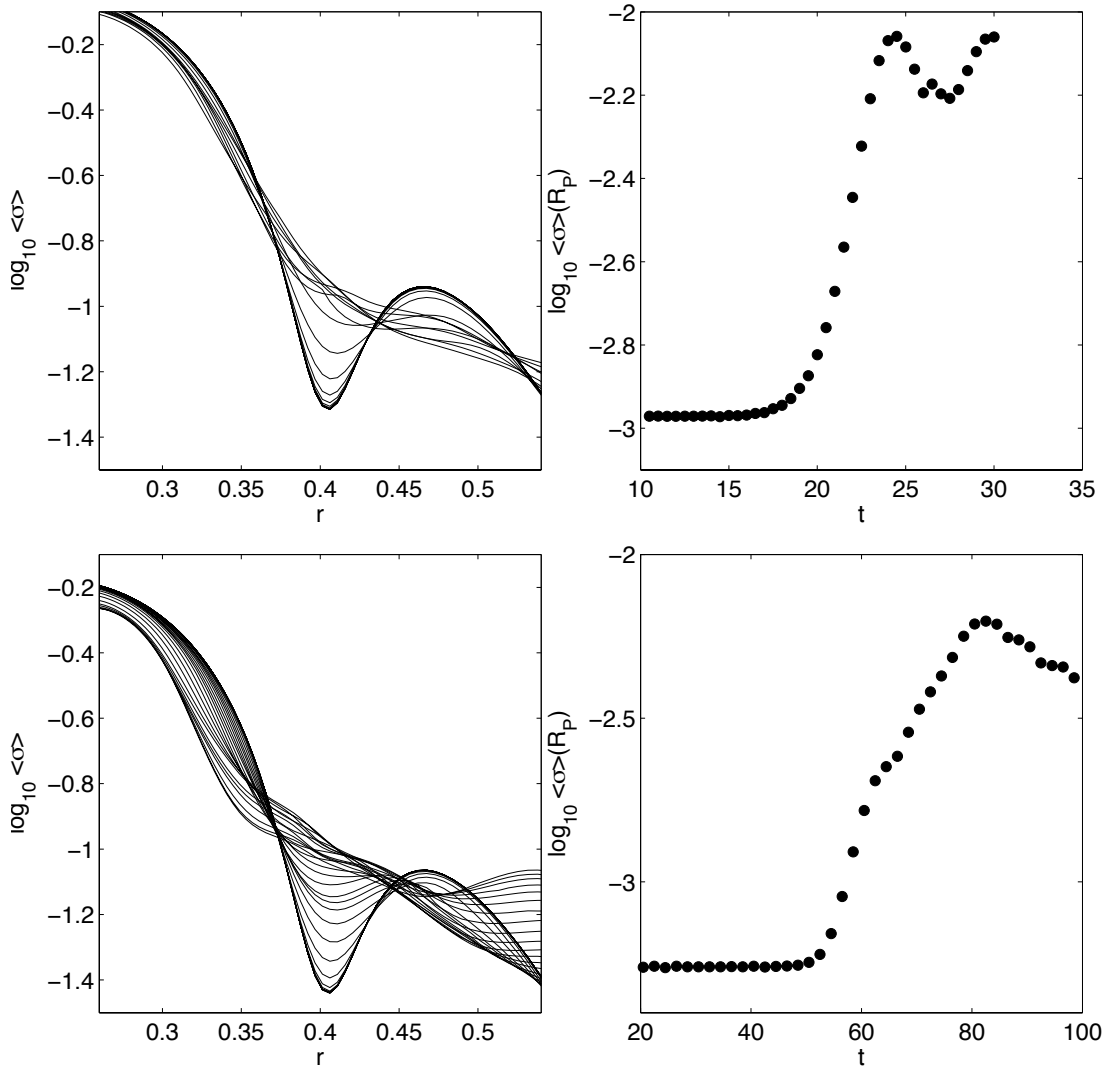

Figure 5.5: Evolution of the density at the gap for models 5 (left panel) and 6 (right panel).

Chapter 6

Planet Formation in the Kepler 16 System

6.1 Abstract

The recently discovered circumbinary planets (Kepler-16 b, Kepler 34-b, Kepler 35-b) represent the first direct evidence of the viability of planet formation in circumbinary orbits. We report on the results of N-body simulations investigating planetesimal accretion in the Kepler-16 b system, focusing on the range of impact velocities under the influence of both stars' gravitational perturbation and friction from a putative protoplanetary disk. Our results show that planet formation might be effectively inhibited for a large range in semi-major axis ($1.75 \lesssim a_P \lesssim 4$ AU), suggesting that the planetary core must have either migrated from outside 4 AU, or formed *in situ* very close to its current location.

6.2 Introduction

The discovery of extrasolar planets around main-sequence stars is one of the major observational breakthroughs of the last decade. The size of the planetary census, propelled by radial velocity (RV) surveys and dedicated missions such as *Kepler*, has grown to include planetary systems where a variety of interesting dynamical interactions can be observed. Such systems include 61 exoplanets discovered around stellar binaries[1] (including both planets orbiting one of the stellar companions and circumbinary planets). While for the majority of these planets the binarity of the system represents only a weak perturbation on the gravitational pull of the central star, a few single-planet systems have been detected in binaries with $a_{\rm bin} \lesssim 30$ AU (such as HD 41004, Gliese 86, HD196885 and γ Cephei), with each planet in a circumstellar ("S-type") orbit. Only one multiple system with $a_{\rm bin} \lesssim 100$ AU has been found (HD177830, Meschiari et al. 2011).

The existence of these systems represents a major challenge to the current paradigm of planet formation. In fact, a number of simulations attempting to model the dynamics of the growth of planetary embryos from *km*-sized planetesimals in presence of a binary companion have hit significant difficulties (among others, Marzari & Scholl 2000, Thébault et al. 2002; 2004; 2006, Thebault 2011, Paardekooper et al. 2008, Fragner et al. 2011). The most important parameter controlling planetesimal accretion is the mutual encounter velocity; indeed, runaway growth requires it to be less than the escape velocity for efficient accretion. The presence of the companion can stir up the relative velocity between planetesimals, interfering with runaway growth. Relative velocity is often excited beyond a fiducial threshold velocity at which all encounters are erosive, potentially slowing down planet formation or halting it altogether. Simulations taking into account a static background gas disk (representing an unperturbed

[1] http://www.exoplanets.org, retrieved on January 15, 2011.

protoplanetary disk at some point in time) initially posited that disk-planetesimals interaction induces a phasing of the orbits, making the environment more accretion-friendly (Marzari & Scholl 2000). Nevertheless, if the protoplanets interact with the gas disk through aerodynamic drag alone, the phasing induced by the gas disk is clearly size-dependent, and protoplanets with different sizes will collide with large encounter speeds over the majority of the range in semi-major axis sampled (Thébault et al. 2004). Finally, a misalignment between the orbital plane of the binary and the gas disk can significantly affect the dynamics of the planetesimals. Small inclinations ($i_{\rm B} < 10^{\circ}$) can favor planetesimal accretion somewhat (Xie & Zhou 2009). On the other hand, large inclinations ($30^{\circ} < i_{\rm B} < 50^{\circ}$) can significantly perturb the planetesimal disk, causing planetesimals to "jump" inwards and pile up into a smaller inner disk, where encounter velocities are more favorable to accretion (Xie et al. 2011).

Most of the works in the literature have focused on observed or plausible circumstellar configurations (e.g. a planet orbiting one of the two stellar components), in light of the lack of direct evidence of the existence of circumbinary planets orbiting main-sequence stars, outside the realm of science fiction. Therefore, only a handful of articles have considered planet formation in circumbinary orbits ("P-type"; e.g., Moriwaki & Nakagawa 2004, Quintana & Lissauer 2006, Scholl et al. 2007, Marzari et al. 2008, Pierens & Nelson 2008a;b), and they lacked a reference observed configuration.

Kepler 16-b (Doyle et al. 2011) is the first circumbinary planet that has been detected with *Kepler*. The presence of a third, planetary object came from transits on both star A (tertiary eclipse) and star B (quaternary eclipse) and the deviations of the timing of the stellar eclipses from a linear ephemeris. The planet was determined to be a Saturn-mass planet ($\mathcal{M}_{\rm P} \approx 0.33 \mathcal{M}_{\rm Jup}$) on a nearly circular 228-day orbit; long-term integrations have shown the planet to be stable, with an eccentricity oscillating between 0 and ≈ 0.08. The binary stellar system is composed of two main-sequence stars in an eccentric 41-day orbit, with a mass of 0.69 and 0.2

$\mathcal{M}_\odot$ (mass ratio $\mu \approx 0.2$), respectively. The close coplanarity of the binary and planetary orbital planes suggests that the three bodies were formed in a common disk. This was bolstered by the measurement of the Rossiter-McLaughlin doppler shift by Winn et al. (2011), which indicated that the spin of the primary is aligned as well.

Recently, Welsh et al. (2012) reported the discovery of two additional circumbinary gas giants (Kepler-34 b and Kepler-35 b). The relative abundance of these systems among the more than 2,000 eclipsing binaries monitored by Kepler (Slawson et al. 2011) implies a lower limit of $\approx 1\%$ in the frequency of circumbinary planets with comparable transit probabilities. Interestingly, all three planets lie just outside the stability boundary for test particles. Their pericenter distance is, respectively, only $\approx 6\%$ (Kepler-34 b), 9% (Kepler-16 b) and 20% (Kepler 35-b) larger than the critical semi-major axis, as estimated by the empirical fit in Holman & Wiegert (1999). This represents an important constraint for the formation of the planetary core. Indeed, a natural scenario would entail the planetary core migrating inwards until near the edge of the disk cavity (which will be comparable in extent to the stability boundary for test particles), where the steep gradient of the disk surface density can halt migration (Pierens & Nelson 2007). Pierens & Nelson (2008b) simulated the evolution of a 20 $\mathcal{M}_\oplus$ core, initially placed at the edge of the cavity and free to accrete gas to become a Saturn-mass planet. They found that once the planet depletes the gas in the coorbital region, it will resume a slow inward migration, until its eccentricity is excited and a phase of runaway outward migration is experienced. This runaway migration appeared to stop once the planet crossed the 5:1 resonance with the binary, at which point slow migration is resumed. The ultimate fate of the planet in these simulations is uncertain, due to the long timescales involved. However, it is expected that disk dispersal will ultimately strand the planet on a circular orbit around the binary. Tantalizingly, Kepler-16b lies somewhat close (and outside of) the 5:1 period ratio with the binary.

In this paper, we investigate the conditions for the formation of planetary cores in

circumbinary orbits around the Kepler-16 binary system, using a simplified numerical model. We consider the evolution of a disk of km-sized planetesimals and determine the impact velocities among planetesimals over 10^5 years, the typical timescale for runaway and oligarchic accretion (Kokubo & Ida 2000). These preliminary N-body simulations will be used to assess the viability of core accretion as a function of the barycentric semi-major axis.

The plan of the paper is as follows. In §6.3, we briefly discuss our numerical model and limitations of our current approach. In §6.4 and §6.5 we discuss the results of our simulations in the context of planet formation, and conclude in §6.6.

6.3 Numerical setup

To conduct our simulations, we use a new hybrid code, SPHIGA (Meschiari et al., 2012, in preparation). SPHIGA is an N-body code that evolves a system of non-interacting test particles (e.g. the planetesimals) subjected to the sum of gravitational forces of massive bodies (e.g. the binary system). In addition, it calculates the frictional force acting on the test particles caused by a putative protoplanetary disk. By default, this is accomplished by following the complete hydrodynamical evolution of the disk with the Smoothed Particle Hydrodynamics scheme (SPH; see, e.g., Rosswog 2009, Price 2012; for recent reviews) in two and three dimensions. The same algorithm used to interpolate the hydrodynamical quantities can be used to interpolate the local gas density and flow and locate possible planetesimal impactors in the same loop, leading to significant computational savings. Modelling the self-consistent perturbations from the binary on the disk can alter the planetesimal evolution and potentially increase impact velocities (Marzari et al. 2008). Indeed, we expect that non-axisymmetric structure, such as global spiral patterns, will be imposed by the binary, adding a complex time-dependent term. The actual impact of the full hydrodynamical evolution is still uncertain, however. Even bulk

quantities such as the disk eccentricity induced by a binary companion appear to depend sensitively on the computational scheme (e.g. the wave damping prescription in Paardekooper et al. 2008) and the amount of physics modeled (e.g. the equation of state and whether self-gravity was included in Marzari et al. 2009, Marzari et al. 2012).

However, significant computational effort is still required to follow the evolution of the combined disk, binary and planetesimal system (with $N_{\rm pl} + N_{\rm gas} > 10^5 - 10^6$ particles) for at least $\approx 10^5$ binary revolutions. Therefore, for the purpose of this paper, we will use an alternative code path that activates a fixed gas background and follow the procedure of Marzari & Scholl (2000) and later papers. A more complete description of the system, including the full hydrodynamical evolution of the protoplanetary disk, will be pursued in a follow-up paper.

The particles are integrated forward in time using a "drift-kick-drift" leapfrog integrator with a fixed timestep. Although this numerical scheme is low order, it is adequate for the problem, since planetesimals lie in low-eccentricity orbits. Additionally, it has the advantage that it is one of the integrators suitable for the full SPH simulations (e.g., Wetzstein et al. 2009), enabling detailed comparison between the present runs and future full hydrodynamical simulations. We verified the validity of this assumption by comparing runs without gas drag (Section 6.4) with the output of the RADAU integrator, as implemented in the Mercury code (Chambers & Migliorini 1997), finding good qualitative agreement between the two.

For lack of better observational constraints, we use the standard prescription of a minimum-mass solar nebula (MMSN; Hayashi 1981), with a density profile $\rho_{\rm g}(a) = \rho_0 (a/1{\rm AU})^{-p}$, where a is the barycentric semi-major axis and we take $\rho_0 \approx 1.4 \times 10^{-9}$ g/cm^3 and $p = 2.75$. This prescription for the protoplanetary gas disk will exhert a frictional acceleration at the location of the planetesimal given by

$$\mathbf{f} = -K |\delta \mathbf{v}| \delta \mathbf{v} \ , \tag{6.1}$$

In Equation (6.1), $\delta\mathbf{v} = \mathbf{v}_{\rm pl} - \mathbf{v}_{\rm gas}$ is the relative velocity of the planetesimal with respect to the Keplerian flow of the gas and K is the drag parameter

$$K = \frac{\pi C \rho_{\rm g} R_{\rm pl}^2}{2\mathcal{M}_{\rm pl}} \ . \tag{6.2}$$

The drag parameter is defined in terms of the planetesimal radius $R_{\rm pl}$, the planetesimal mass $\mathcal{M}_{\rm pl}$ (calculated assuming $\rho_{\rm pl} = 3$ g/cm^3), and the dimensionless coefficient C ($C \approx 0.4$ for spherical bodies).

To evaluate the collisional speeds among planetesimals, we follow the dynamical evolution of 30,000 test particles uniformly distributed with barycentric semi-major axes between 0.66 and 6 AU; this range includes the current location of the planet ($a_{\rm P} \approx 0.7$ AU). Particles that travel into the inner boundary or become unbound are removed from the simulation.

The inner boundary was determined by running a simulation with test particles in circular barycentric orbits covering semi-major axes in the range $(1.2a_{\rm b}; 5a_{\rm b})$ for 10^4 years. Particles that suffer close encounters with the central binary or escape the system are deemed unstable. The largest semi-major axis outside which all particles are stable is taken as the inner boundary. The final value for the inner boundary is in excellent agreement with the fitting formula in Holman & Wiegert (1999).

In the full simulation, we take the initial eccentricities and inclinations to be uniformly distributed between 0 and 10^{-5}, though the actual choice of the upper bound is somewhat unimportant given the fact that the initial distribution of orbital parameters is quickly erased within a few orbits of the binary. To obtain reasonable collision statistics for the duration of the simulation, we track planetesimal collisions using the inflated radius prescription (Brahic 1976, Charnoz et al. 2001), with $r_{\rm infl} = 5 \times 10^{-5}$ AU. Collisions are detected by populating a tree structure at each timestep (as part of the SPH algorithm) and walking the tree to locate the nearest neighbors to each planetesimal with $d < 2r_{\rm infl}$ (e.g., Barnes & Hut 1986, Hernquist

& Katz 1989).

6.3.1 Impact classification

The system is initially evolved to 10^5 years. After this interval, planetesimal-planetesimal close encounters are recorded, with the most important parameter being Δv, the impact velocity. We follow Fragner et al. (2011) and Thebault (2011) and adopt the prescription for classifying disruptive impacts for planetesimals presented in Stewart & Leinhardt (2009; SL09). The latter work offers a criterion for catastrophic disruption, the main parameters being the reduced kinetic energy, the masses of the impactors and material properties and constants derived from fits to numerical and laboratory data. SL09 presents fits for classifying catastrophic encounters in two limiting regimes: weak aggregates ("rubble piles") and strong rocks. For each encounter, we calculate the escape velocity $v_{\rm esc}(R_1, R_2)$, the erosive velocity for weak aggregates $v_{\rm weak}(R_1, R_2, \Delta v)$ and the erosive velocity for strong aggregates $v_{\rm strong}(R_1, R_2, \Delta v)$. In regions where $\Delta v < v_{\rm esc}$, unperturbed, runaway accretion is possible. Impacts where $v_{\rm esc} < \Delta v < v_{\rm weak}$ are assumed to still be accreting, though runaway accretion might be disturbed. Finally, we classify impacts where $v_{\rm weak} < \Delta v < v_{\rm strong}$ and $\Delta v > v_{\rm strong}$ as "uncertain" and "erosive", respectively. Locations where the majority of the encounters are classified as erosive can be deemed as unsuitable for the formation of planetary cores. This limitation is size-dependent, since larger planetesimals are more resistant to fragmentation. Therefore, it could, in line of principle, be overcome if the km-sized stage of planet formation is bypassed, and the initial population comprises larger objects (e.g. $R_{\rm pl} > 100$ km).

In our nominal runs (Section 6.4 and 6.5) we assign a planetesimal radius for each particle, randomly distributed between 1 and 10 km. We allow for a non-flat primordial distribution in planetesimal sizes by assigning a weight $f(R_1, R_2)$ to each impact between planetesimals of radius R_1 and R_2. Following Thébault et al. (2008), we use a Maxwellian weighting function

centered around 5 km with $\sigma = 1$ km. A priori, this choice should yield a more accretion-friendly environment, since it weighs collisions between same-sized planetesimals more than different-sized planetesimals.

Finally, we generously classify a radial bin as "accretion-friendly" when more than 50% of all impacts have an outcome of accretion, disturbed accretion or uncertain outcome.

6.4 Simulations without gas drag

We first show the impact statistics for a fiducial simulation without gas drag. In this case, the planetesimals are perturbed by gravitational stirring from the binary companion alone, which is size-independent. Therefore, their eccentricities will oscillate around the forced eccentricity at that semi-major axis,

$$e_{\rm f} = \frac{5}{4}(1-2\mu)\frac{a_{\rm B}}{a}e_{\rm B} \tag{6.3}$$

(Moriwaki & Nakagawa 2004), such that the upper envelope of the eccentricity oscillations is $\approx 2e_{\rm f}$ (Figure 6.1). Although the excited eccentricities are large, the planetesimals are initially weakly phased because the oscillations are coherent and spatially extended; therefore, impact velocities tend to be low. However, the frequency of the oscillation around the forced eccentricity increases with time, ultimately leading to orbital crossing (Thébault et al. 2006). The orbital crossing boundary $a_{\rm cross}$ sweeps outwards in semi-major axis, increasing impact velocities. In our simulation, collisions are recorded after $t = 10^5$ years. As evidenced in Figure 6.1, regions outside ≈ 3.5 AU ($\approx 13a_{\rm B}$) have not experienced orbital crossing after 1.5×10^5 years. This is expected, since $a_{\rm cross}$ is a weak function of time (Thébault et al. 2006). Therefore, encounter velocities will be lower in the outer part of the disk.

Figure 6.2 shows the relative fraction of accreting encounters, disturbed accretion, and encounters that might be erosive for one or both the prescriptions described in Section 6.3.1.

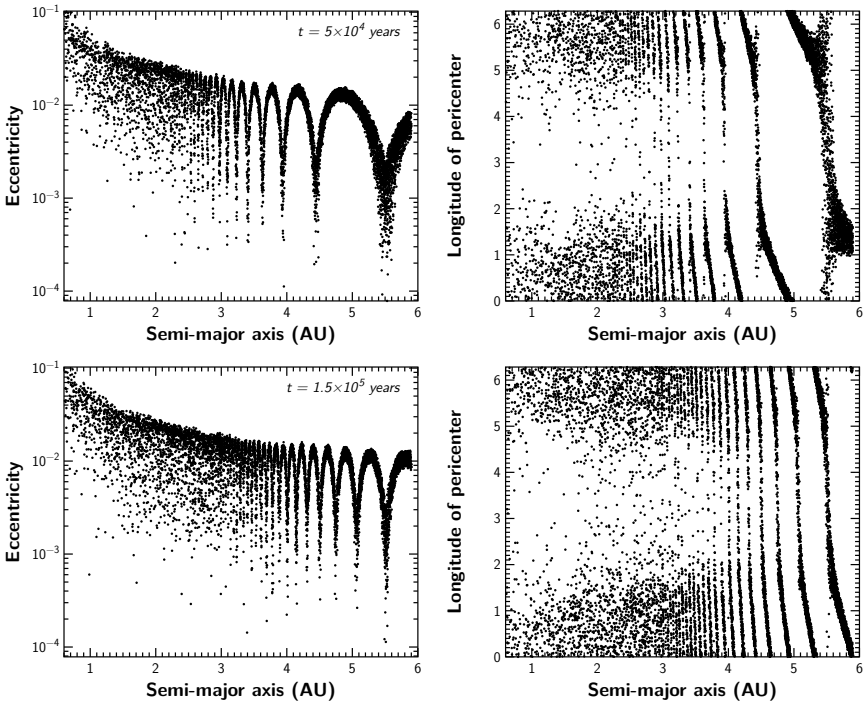

Figure 6.1: Eccentricity e and longitude of pericenter $\varpi - \varpi_{\rm B}$ after 10^4 (*top panel*) and 1.5×10^5 years (*bottom panel*), in absence of gas drag.

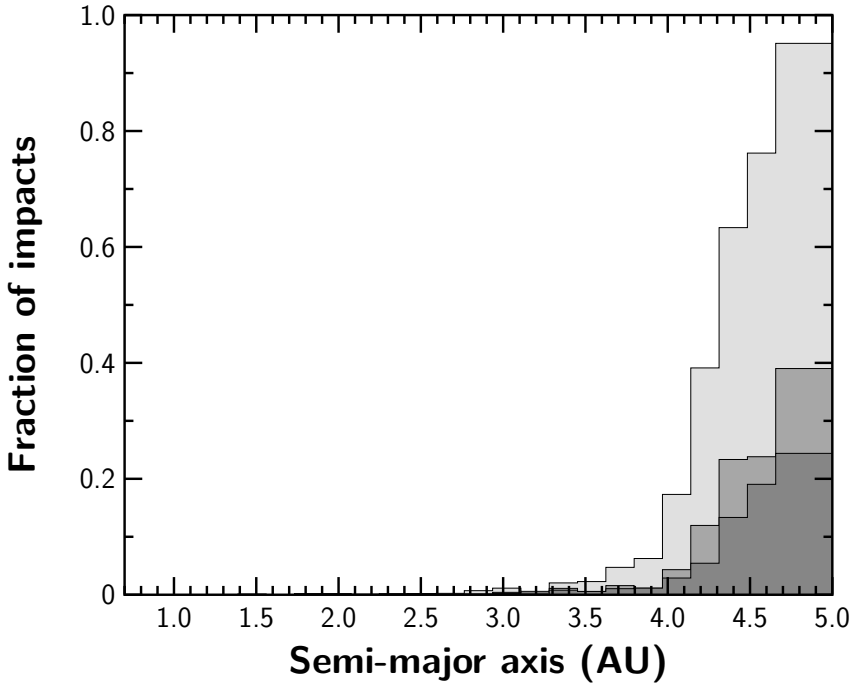

Figure 6.2: Fraction of accreting (dark gray), disturbed (medium gray), uncertain (light gray) and erosive impacts (white), as a function of semi-major axis, for the nominal gas-free run.

For this binary configuration, impact speeds are too high for core formation everywhere inside at least ≈ 4 AU. On longer timescales, even the outer parts of the planetesimal disk may become hostile to accretion, as the orbital crossing boundary moves outwards and raises the impact velocities.

6.5 Simulations with gas drag

Simulations where gas drag is active present a radically different dynamical picture. As expected, gas drag tends to damp the eccentricity oscillations towards the forced eccentricity value (Figure 6.3). The gas drag acceleration (Equation 6.1) is size dependent (proportional to $R_{\rm pl}^{-1}$). Therefore, damping and periastron phasing will be more effective for smaller bodies. However, the eccentricity spread remains somewhat large at small semi-major axes, where the gravitational perturbation of the central binary acts to pump eccentricities. At large semi-major axes, where the damping timescale is longer, the values of eccentricity tend to their counterparts in the simulations without gas drag.

Inside 1 AU, the planetesimal disk is severely depleted due to radial drift. The radial drift timescale can be estimated by assuming the planetesimal loses angular momentum slowly due to the torque from the headwind of the gas (Weidenschilling 1977). For the drag prescription of Equation 6.1, we find an estimate for the infall timescale (in units where $G\mathcal{M} = 1$) is given by

$$\tau_{\rm rd} = \frac{a_{\rm pl}}{v_{\rm rd}} \approx \frac{4}{3} C^{-1} \mathcal{M}_* \frac{\rho_{\rm pl}}{\rho_{\rm gas}} \frac{R_{\rm pl}}{a_{\rm pl}^{1/2}} \left(\delta v\right)^{-2} \ , \tag{6.4}$$

where $\rho_{\rm pl}$ is the density of the planetesimal and $\mathcal{M}_*$ is the total mass of the binary. In the case of planet formation around single stars, eccentricities are very low and $\delta v \sim h_0^2 v_{\rm kep}$ is mainly determined by the local scale height, with a typical timescale at 1 AU of 10^6 years for a 5-km planetesimal.

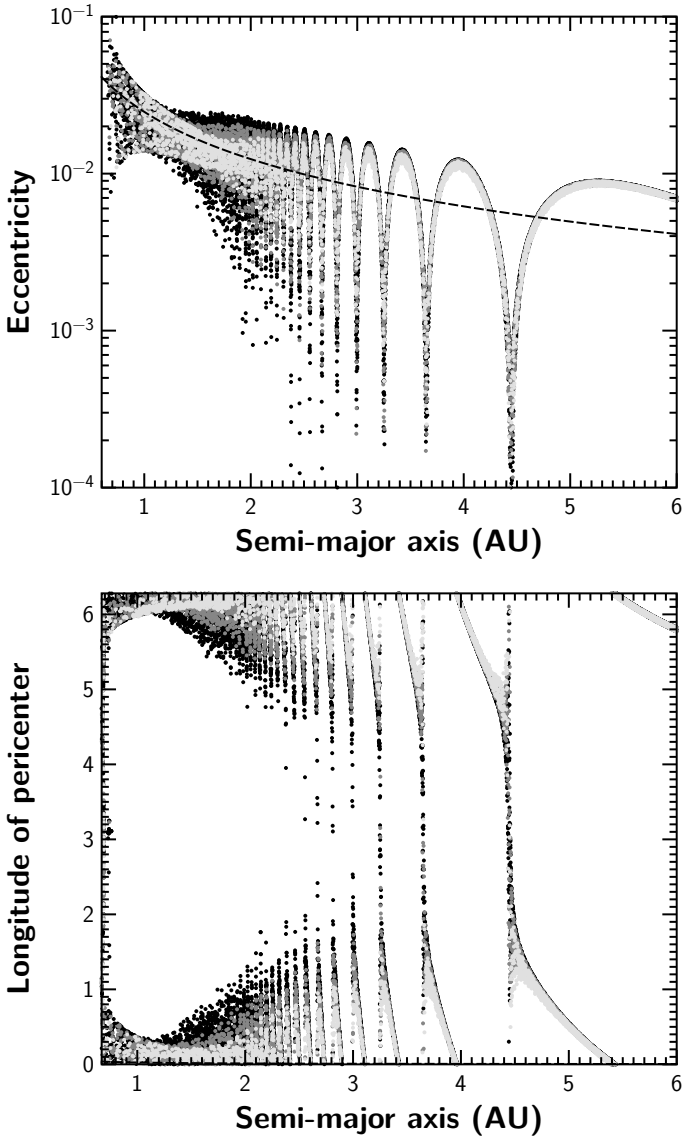

Figure 6.3: Eccentricity e and longitude of pericenter $\varpi - \varpi_{\rm B}$ as a function of semi-major axis. Planetesimals are colorized with respect to their size: light gray ($1 < R_{\rm pl} < 4$ km), medium gray ($4 < R_{\rm pl} < 7$ km), black ($7 < R_{\rm pl} < 10$ km. The dashed line shows the forced eccentricity.

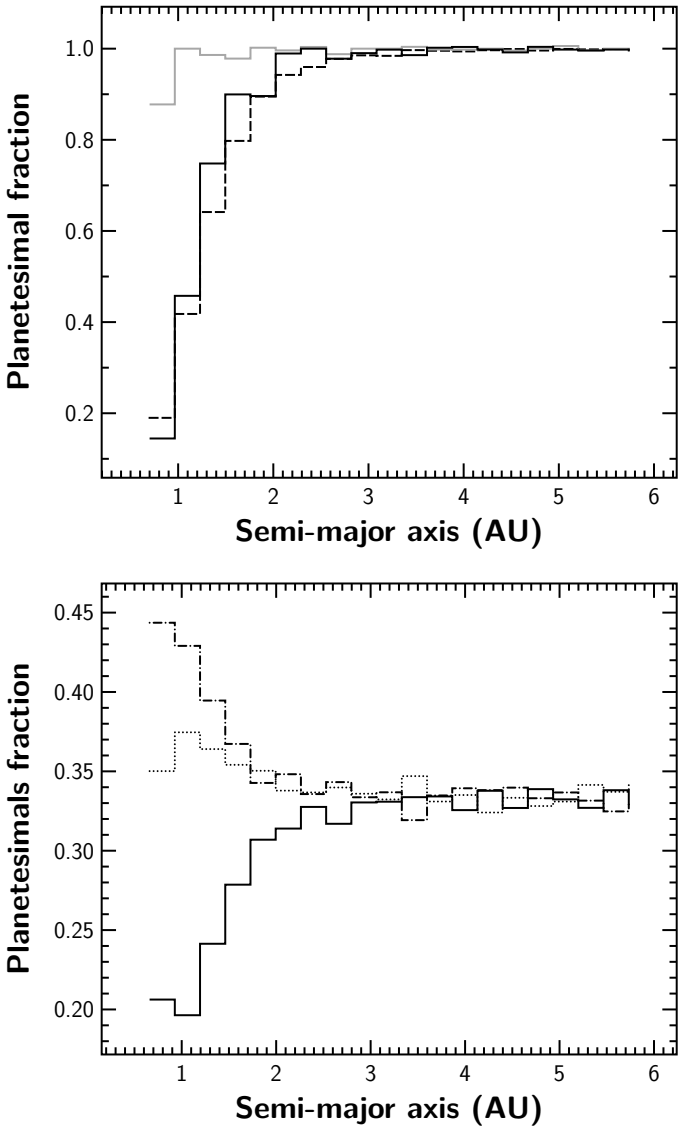

Figure 6.4: *(Top)* Planetesimal number binned in semi-major axis, normalized by the initial distribution in semi-major axis. The N-body run (black line) and the output from an analytic model for the single star case (gray line) and with a forced eccentricity term (dashed line) are shown. *(Bottom)* Fraction of planetesimals with $1 < R_{\rm pl} < 4$ km (solid line), $4 < R_{\rm pl} < 7$ km (dotted line) and $7 < R_{\rm pl} < 10$ km (dash-dotted line).

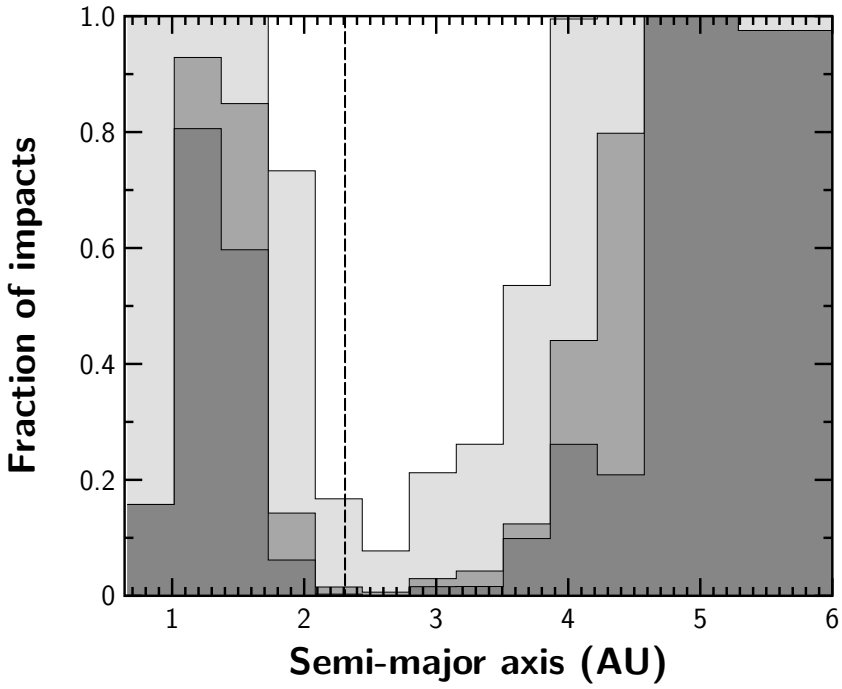

Figure 6.5: Fraction of accreting (dark gray), disturbed (medium gray), uncertain (light gray) and erosive impacts (white), as a function of semi-major axis, for the run with gas drag. The location of the fiducial ice line is plotted (dashed line).

In the circumbinary environment, the perturbation from the binary companion acts to raise eccentricities throughout the planetesimal disk, such that the dominant term contributing to δv is given by the time-varying speed of the planetesimal sampling different gas velocities at the apsides. In this case, drift timescales are a strong function of semi-major axis ($\propto a^{-5/2}$), such that radial drift from the outer parts of the disk cannot replenish the inner disk effectively. Figure 6.4 shows the distribution of planetesimals after $t = 10^5$ years, binned in semi-major axis. We compared the planetesimal distribution of our N-body run with an analytic model based on Equation 6.5. Assuming $\delta v \approx 0.5 e_{\rm f} v_{\rm kep}$, we find good agreement between the two. Finally, the second panel of Figure 6.4 shows that the distribution of planetesimal sizes is skewed towards larger planetesimals at small semi-major axes, since larger planetesimals are less affected by the gas drag. This can contribute to making the inner region more accretion-friendly for two reasons. Firstly, larger planetesimals can withstand larger impact velocities. Secondly, the spread in sizes will be reduced, which means that the spread in the phasing of the planetesimals will also be reduced.

Figure 6.5 shows the fraction of accreting encounters as a function of semi-major axis. We found that the following qualitative situation holds for different radial locations:

1. between the stability boundary and 1 AU, eccentricities are pumped to high values and planetesimal number density is low due to the low radial drift timescale. The majority of encounters are erosive.

2. for a small range in semi-major axis outside 1 AU, the spread in e and ϖ is smaller and planetesimal distributions are skewed towards larger planetesimals. The majority of encounters are accreting.

3. between 1.75 AU and 4 AUs, the magnitude of the eccentricity and the differential phasing raises the impact velocities, such that the majority of the encounters are erosive.

4. outside 4 AUs, orbital crossing has not been realized and gas drag is weaker due to the steep radial dependence of the gas density; therefore, orbits are only weakly phased. The majority of encounters are accreting.

We conclude that planet formation is inhibited only for a small range in semi-major axis (location (d), between 1 and 4 AUs). This range in semi-major axis includes the nominal location of the ice line for an irradiated disk, estimated from the scaling $a_{\rm ice} \sim 2.7{\rm AU}\ (\mathcal{M}/\mathcal{M}_{\odot})^2 \approx 2.3$ AU (Ida & Lin 2004), assuming $\mathcal{M} = \mathcal{M}_{\rm A} + \mathcal{M}_{\rm B}$.

What is the impact of this "forbidden region" for planet formation? It is instructive to refer to the predictions of the standard core accretion paradigm for single stars; in particular, the outcome of large-scale Monte-Carlo planet synthesis models (e.g. Ida & Lin 2004, Mordasini et al. 2009). Mordasini et al. (2012) recently conducted a Monte-Carlo planet synthesis simulation for a variety of disk masses and metallicities, for the nominal case of a 1 $\mathcal{M}_{\odot}$ central star. In the core accretion paradigm, metallicity represents a threshold quantity for the formation of planetary cores. Accordingly, they found that the cores of giant planets ($\mathcal{M} \gtrsim \mathcal{M}_{\rm J}$) tend to preferentially form outside the ice line when the metallicity (which acts as a proxy for the solid content of the disk) is low. The actual location of the ice line scales with the disk mass, which contributes to the spread in semi-major axis.

In Figure (6.6), we plot a different subset of the output of the simulations of Mordasini et al. (2012)[2], focusing on the ensemble of embryos that acquire masses comparable to Kepler-16 b ($0.2\mathcal{M}_{\rm J} < \mathcal{M} < 0.4\mathcal{M}_{\rm J}$). The initial location of the embryo is plotted as a function of metallicity. For disks of solar or super-solar metallicity, such planets are formed throughout the disk, with a substantial fraction formed inside 2 AU (about 40%). At subsolar metallicities comparable to Kepler-16 ([Fe/H] $\approx -0.3 \pm 0.2$), however, such cores are only found outside 2 AU, with a minority lying in location (c) (about 20%). While the synthetic population refers

[2]http://www.mpia-hd.mpg.de/homes/mordasini/Site7.html

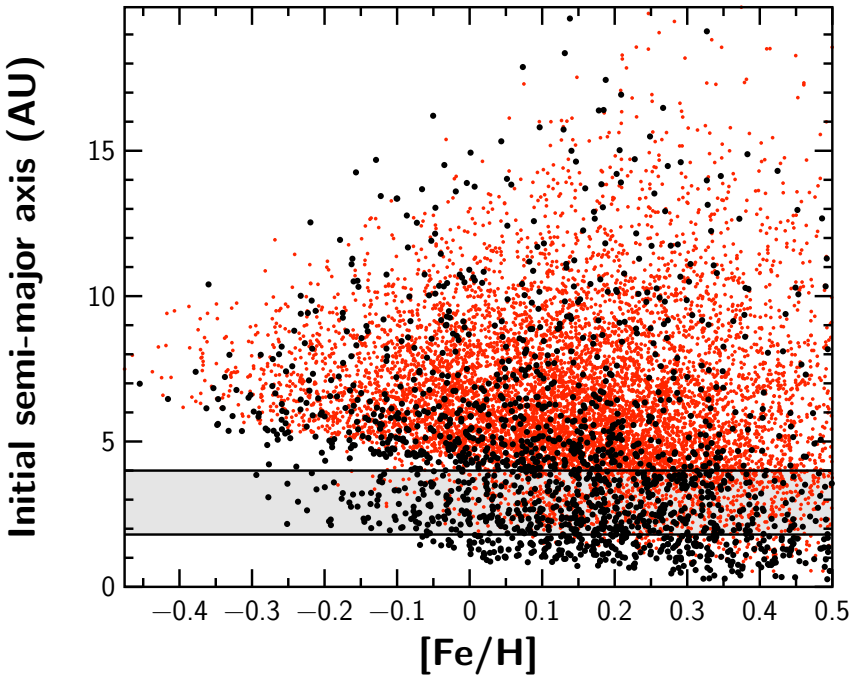

Figure 6.6: Initial location of embryos that grow to final masses $0.2 < \mathcal{M}_{\rm P} < 0.4\mathcal{M}_{\rm J}$ (black points) and $\mathcal{M}_{\rm final} > 1\mathcal{M}_{\rm J}$ (red dots), for a range of metallicities and disk masses. The shaded region corresponds to the range in semi-major axis where embryo formation is disturbed in the Kepler-16 system.

to the nominal 1 $\mathcal{M}_{\odot}$ single star case, with one embryo per disk, it suggests that in-situ planet formation in location (a) might be hampered by the low surface density in solids at 1 AU.

It is also crucial to recognize that in the inner disk, non-axisymmetric perturbations from the disk might be important. The eccentric central binary will likely excite spiral structures, which might act to pump the eccentricity of the inner planetesimals and alter the phasing of their orbits. Indeed, Marzari et al. (2008) conducted full 2D hydrodynamical simulations with a small number of tracer planetesimals embedded in the disk, and found significant oscillations in the eccentricity and longitude of pericenter around the equilibrium value.

6.6 Discussion

Planet formation in presence of close binaries presents a number of challenges to the traditional core accretion paradigm. Historically, most of the theoretical effort has been expended to study pathways to planet formation in S-type orbits for planets that had been observed through RV surveys, or targets with observationally desirable properties (e.g., α Cen). With the launch of *Kepler*, however, we expect that the sample of planets in P-type orbits around eclipsing binaries will rapidly outnumber the handful of planets in circumstellar configurations detected with RV surveys. Indeed, a sample of 750 *Kepler* targets are eclipsing binaries for which eclipses of both stars are observed, and a subset of 18% exhibited deviations in the timing of the eclipses (Welsh et al. 2012). Since the definitive determination of the planetary nature of a putative KOI relies on the detection of tertiary and quaternary eclipses, we expect that as the baseline of the observation increases, more KOIs will be confirmed as genuine circumbinary objects.

In this paper, we have conducted a preliminary simulation of the feasibility of circumbinary planet formation in the Kepler-16 system. In accordance to an earlier study conducted by

Scholl et al. (2007) for a different set of binary parameters, we have found that, for generous initial conditions that favor planetesimal accretion, planet formation appears to be feasible far enough from the central binary. However, we have identified a radial span between 1.75 and 4 AU where planet formation is strongly inhibited. Within the planet accretion framework, the most likely sequence of event is the formation of a core outside the forbidden region, followed by inwards migration driven by tidal interaction with the protoplanetary disk (Pierens & Nelson 2007). Although we measured impact velocities favorable to accretion in the inner AU of the disk, formation *in situ* of Kepler-16 b is less likely due to the low metallicity of the star and non-axisymmetric perturbations from the disk, not modeled in this simulation.

We remark that the simulations presented in this paper only demonstrate that, *choosing the most favorable conditions for planetesimal accretion* and an assumed initial planetesimal size of 1-10 km, the formation of an embryo outside the critical semi-major axis $a_{\rm crit}$ is viable, with traditional migration processes subsequently moving the planet to its current location. Due to computational limitations, we disregarded the evolution of the protoplanetary disk and the collisional outcome of planetesimal impacts. For the former, we plan to follow approximately the hydrodynamical response of the disk with the SPH algorithm included in the SPHIGA code in a follow-up paper. For the latter, the numerical procedure of Paardekooper & Leinhardt (2010) represents a possible approach to follow the evolution of the planetesimal size distribution.

Chapter 7

Discussion

In light of the rapid observational and theoretical progress in the field and the breadth of the exoplanetary "bestiary" uncovered by *Kepler*, in this section I briefly discuss some of the most recent follow-up work in the context of this Thesis and indicate future directions for this work.

7.1 Transit Timing Variations

Much of the excitement in the diagnostic power of TTVs originally resided in its ability to detect terrestrial planets, which would be outside the reach of Doppler surveys. Terrestrial planets residing in mean motion resonances with giant planets would be easily discovered even when their transits were not detected, since they exert TTV signals of the order of several minutes (Agol et al. 2005, Holman & Murray 2005, Steffen & Agol 2007).

However, despite significant observational effort and a few tantalizing signals (e.g., Steffen & Agol 2005, Miller-Ricci et al. 2008, Nascimbeni et al. 2011, Maciejewski et al. 2011), this method seemingly failed to live up to its promise. In Chapter §3, we identified a funda-

mental issue in the characterization of low-mass planets detected through TTVs alone. Indeed, systems that are in or close to a mean motion resonance, which produce the most readily detectable TTV amplitudes, generate signals that are highly degenerate. Consequently, a range of masses and periods of the non-transiting planet can fit the signal, preventing a precise characterization. This degeneracy is due to the fact that, for configurations close to a first-order period commensurability (PC), the dominant frequency and amplitude of the TTV signal are, respectively,

$$P_{TTV} \sim P_{tr}\epsilon^{-1} \tag{7.1}$$

$$A_{TTV} \approx \mu\epsilon^{-1}P_{tr} \tag{7.2}$$

where P_{tr} is the period of the transiting planet, μ is the mass ratio of the perturber to the central star and ϵ is the offset from the nominal resonance (Agol et al. 2005). These scalings do not single out one PC over another (the same is true for higher-order PCs; see, e.g., Boué et al. 2012). If the signal is well characterized by this single frequency, for instance because noise suppressed other harmonics, then the degeneracy is inevitable (Nesvorný & Morbidelli 2008).

Since the launch of *Kepler*, the use of transit timing variations has become pervasive and indispensable for characterizing multiple-transiting systems. Since, in this specific case, periods and phases are known for all bodies, then a TTV dataset coupled with N-body integrations can pinpoint the planetary masses (e.g., Holman et al. 2010, Cochran et al. 2011, Lissauer et al. 2011) or at least ascertain their planetary status through dynamical stability considerations (e.g., Fabrycky et al. 2012a). The detection of low-mass planets with the TTV method as outlined above, however, has been far less fruitful. One of the chief reasons is likely the relative paucity of observed multiple-planet systems where the inner planet is close to a period commensurability with the other planets. Although Fabrycky et al. (2012b) found an excess of planets close to first-order resonances, the pile-up is distinctively wide of the resonance and

clusters around $\epsilon \approx 0.025$ ($\zeta_1 \approx -0.15$). In between PCs and for low-eccentricity orbits, taking the latter fact into account yields an order of magnitude estimation of

$$A_{ttv} \approx 30 \text{ s} \left(\frac{\mathcal{M}_{pert}}{1\mathcal{M}_{\oplus}}\right)\left(\frac{P_{tr}}{3 \text{ d}}\right) \tag{7.3}$$

i.e., on the order of tens of seconds, a signal far more challenging to detect and characterize even with *Kepler*.

Ballard et al. (2011) presented the first non-transiting planet discovered with *Kepler*. Kepler 19-c exerts transit timing variations with an amplitude of 5 minutes. Because of the issue of degeneracy, several scenarios were considered. The planetary status of c was argued on the grounds of dynamical stability (in the case of high eccentricity of the perturber) and constraints from the radial velocity dataset. The culled set of possibilities, nevertheless, spanned many orbits near period commensurabilities. These included perturbers in PCs internal and external to Kepler 19-b and co-orbital perturbers. As anticipated in Chapter §3, the presence of a RV dataset helped exclude $\mathcal{M}_c > 6\mathcal{M}_J$; however, the small dataset could not pinpoint the mass precisely. Recently, Nesvorný et al. (2012) identified a planetary system (KOI-872) where the inner, transiting planet displayed a TTV signal with large amplitude (2 hours). In this case, the perturber was determined to be a Saturn-mass planet ($\mathcal{M} \approx 0.37\mathcal{M}_J$), after ruling out other fits yielding a higher χ^2.

The detection of non-transiting Earth and even super-Earth class planets through the TTV method will likely remain extremely challenging, given the intricacies of interpreting the TTV signal and the low amplitudes found sufficiently away from period commensurabilities (e.g., Veras et al. 2011). We note that obtaining RV datasets of precision comparable to that advocated in Chapter §3 is likely not feasible; this was not anticipated at the time of writing. Indeed, as mentioned in Chapter §1, stars in the *Kepler* sample are typically too faint and active for the kind of RV precision advocated. However, in some circumstances, RV datasets may aid

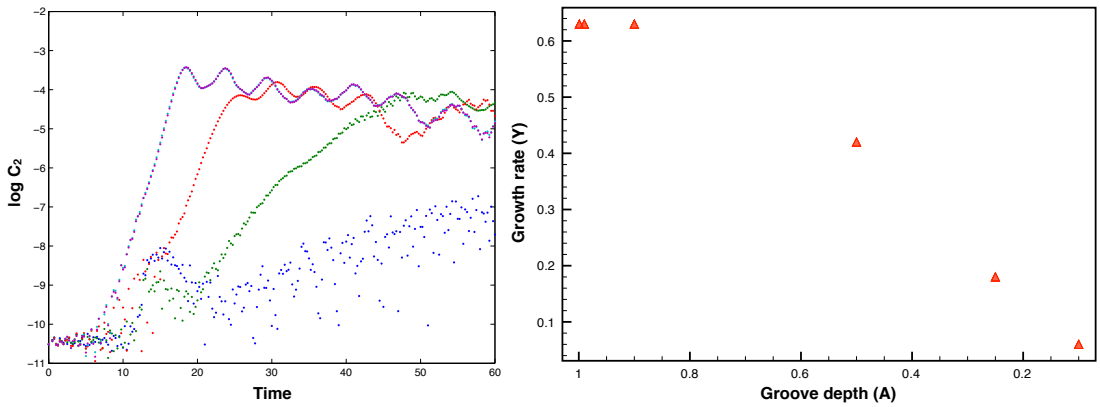

Figure 7.1: (Left) Amplitude of the instability as a function of time for several gap depths A (from left to right, $A = 0.999$, 0.99, 0.9, 0.5, 0.25, 0.1; the evolution of the first three cases is identical). The disk mass is $q_D = 0.16$. (Right) Growth rate as a function of the gap depth.

in excluding massive planets in higher-order resonances from the list of possible configurations. Dynamical stability considerations, in the case of putative massive perturbers, will also help rule out unstable, degenerate solutions.

7.2 Gravitational instabilities driven by planetary gaps

Chapter §5 presented a series of two-dimensional simulations of moderately massive protoplanetary disks, on which a deep gap in surface density was imposed. In our simulations, we found that the presence of the gap drove a strong global instability, even in disks that were not massive enough to be gravitationally unstable otherwise.

Lin & Papaloizou (2011) confirmed our findings by self-consistently following the development of a gap opened by introducing a planet in a smooth disk. They found that global GI modes were launched *during* the development of the gap of a Saturn-mass planet, when the gap depth is only 20-30% relative to the unperturbed disk. This is much shallower than the disks considered in Meschiari & Laughlin (2008). For the same models in Meschiari & Laughlin (2008), we have also found that the instability is active even at moderate and small gap

depths (Figure 7.1, unpublished). The disk in Lin & Papaloizou (2011) was slightly less massive ($q_D \gtrsim 0.06\mathcal{M}_*$) than that considered in this work, although still more massive than the typical MMSN models.

In regards to their effect on planetary migration, they found that the torques exerted by the spiral modes are time-depended and oscillatory. In a follow-up work, Lin & Papaloizou (2012) found outward migration of the planet in models where the Toomre Q decreases radially. As anticipated in Chapter §5, the presence of the spiral modes significantly influences migration. In particular, the gravitationally unstable gap cannot be maintained cleanly as they are disrupted and replenished by the spiral modes (e.g. Figure 5.5). In their simulations, the planet may move rapidly outward and form new gaps, in turn launching new instabilities. Overall, it seems likely that standard, steady-state Type-II migration cannot provide an accurate description of the evolution of gap-opening planets embedded in moderately massive disks.

As noted in Chapter §5, it will be crucial to identify the lower limit in disk mass at which the gap instability is active. This will require further high-resolution numerical simulations. Finally, gas accretion on the planet has been, to date, neglected in hydrodynamical simulations; given the high effective viscosity at the gap location, we remark that this could have further implication in the mass growth and migration of the planet. We will address these questions in a forthcoming study.

7.3 Planet formation in binary systems

Chapter §6 investigated the feasibility of circumbinary planet formation in the Kepler-16 system. We remark that the study presented in Chapter §6 is only preliminary, and a full study including the hydrodynamical evolution of the disk will likely severely modify the ranges in semi-major axis favorable to planetesimal accretion. In fact, we anticipated that the non-

axisymmetric perturbations from the central binary would prevent embryo formation inside the inner AU, even if the pure N-body simulations indicate it as a possible site for runaway accretion.

We remark that other processes may be at work as well to inhibit planet formation. Indeed, simulations presented in the literature to date have assumed that the disk in which the planetesimals are embedded resemble smooth, MMSN-type models initialized on a sub-Keplerian flow, at least as a starting condition. This is likely not representative of real protoplanetary disks, which are expected to experience density fluctuations and small-scale clumpiness as a result of MRI turbulence (Balbus & Hawley 1991). For instance, Laughlin et al. (2004) conducted hydrodynamical simulations, in which a protoplanet embedded in a gaseous disk experienced a random walk as a result of turbulent torques, overwhelming the smooth Type-I migration. They derived a simple prescription for the stochastic turbulent torques, informed by MHD simulations. Each turbulent wake exerted a torque $\mathcal{T}$ on a planet of mass $\mathcal{M}_P$ of the form

$$\mathcal{T}_m = -\frac{mA\xi\Gamma\mathcal{M}_P}{r^{1/2}} e^{-(r-r_c)^2/\sigma^2} \sin(m\theta - \phi - \Omega_C t) \sin(\pi t/\Delta t) \tag{7.4}$$

modeling a m-fold density fluctuation of amplitude $A\xi$, centered on r_c, with pattern speed Ω_c and lifetime Δt; Γ is an attenuation factor which translates the strength of the torques used to sustain turbulent fluctuations into the actual torque exerted by the turbulent fluctuation thus generated. Ida et al. (2008) argued qualitatively that km-sized planetesimals are likely in a highly erosive regime even in presence of nominal levels of turbulence. Nelson & Gressel (2010), using global 3D MHD and shearing box simulations, showed that turbulence excites the velocity dispersion of the planetesimals and dominates their radial migration. Figure 7.2 shows a typical turbulent torque pattern generated by Equation 7.4.

This is likely to be relevant in the configuration examined in Chapter §6 as well. Indeed, we can compare the gas torque (Equation 1.8) with an order-of-magnitude estimate of the summed turbulent torques operating on a planetesimal of radius R_P (Laughlin et al. 2004).

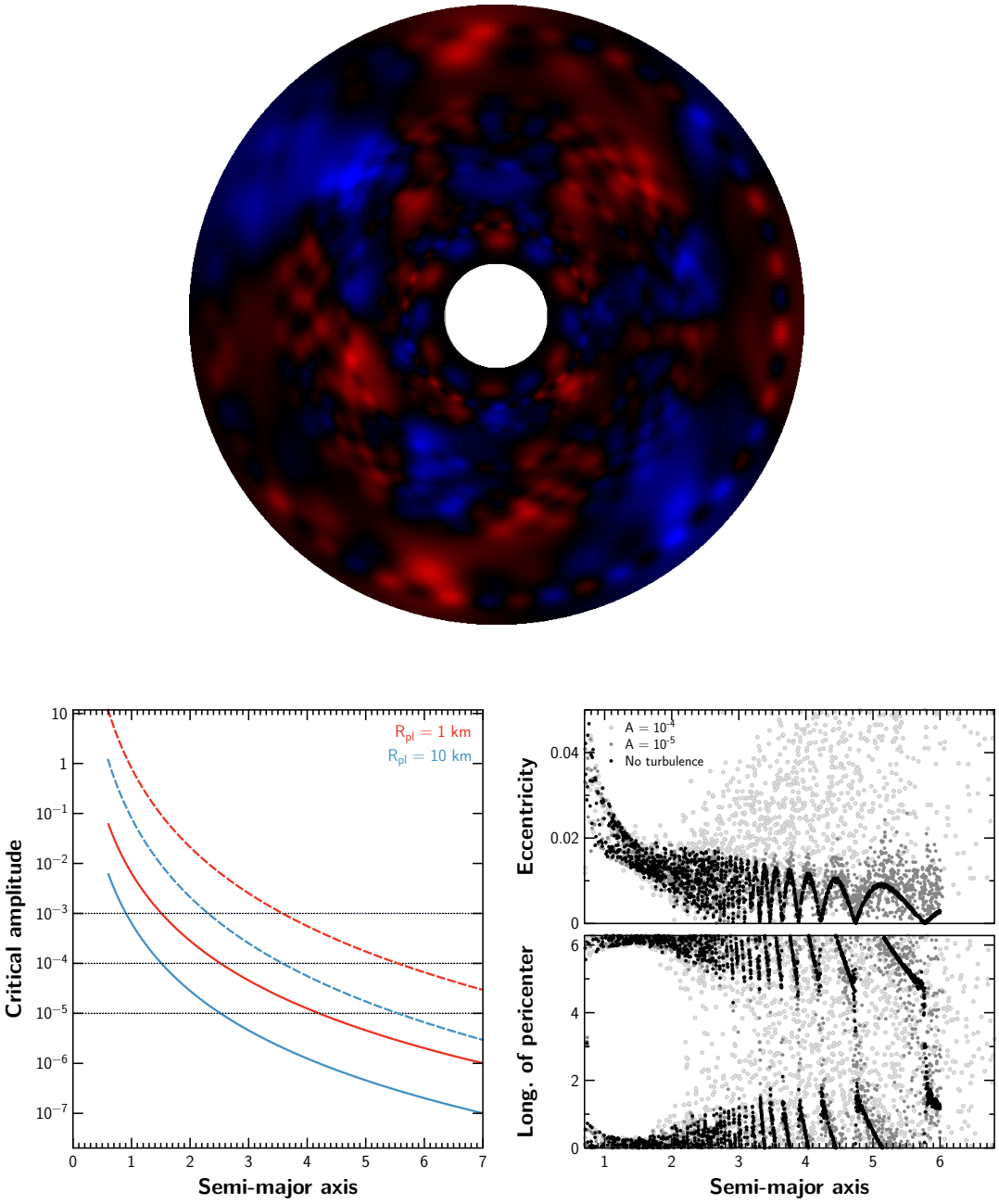

Figure 7.2: (Top) Snapshot of the summed torque pattern as generated by Equation 7.4. Blue areas are positive torques, while red areas are negative torques. (Bottom left) Critical value of A as a function of radius (Equation 7.5). The dashed lines show the same for an accumulation factor $\mathcal{P} = 10^5$ yr$/P_{orb}$. (Bottom right) Orbital elements of planetesimals perturbed with the turbulent torques of Equation 7.4, for $A = 0$, 10^{-5}, 10^{-4}.

Assuming Equation 1.12 for the typical planetesimal speed relative to the gas and the frictional torque of Equation 1.8, then we estimate that the critical amplitude A_C at which turbulent torques equal the frictional torque from the gas is given by

$$A_C = 5 \times 10^{-4} \left(\frac{1\text{AU}}{a}\right)^{9/2} \left(\frac{1 \text{ km}}{R_{pl}}\right) \left(\frac{3 \text{ g cm}^3}{\rho_{pl}}\right) \left(\frac{\mathcal{M}_*}{\mathcal{M}_\odot}\right)^2 \left(\frac{0.05}{h}\right) \left(\frac{0.22}{a_B}\right)^2 \left(\frac{0.15}{e_B}\right)^2 \mathcal{P} \quad (7.5)$$

where a, R_{pl} and ρ_{pl} are the semi-major axis, radius and density of the planetesimal, respectively, $\mathcal{M}_*$ is the total stellar mass and h is the scale height of the disk. The factor $\mathcal{P}$ takes into account that the turbulent torques accumulate in a stochastic fashion; therefore, the critical A_C over the course of an entire simulation is larger by a factor $\mathcal{P} \approx (t_{sim}/P_{orb})^{1/2}$, where P_{orb} represents the typical timescale of a turbulent fluctuation and t_{sim} is the time over which fluctuations are summed (i.e.., the length of the simulation). Although this formula is valid only within an order of magnitude, we can infer from Figure 7.2 that planetesimals outside about 4 AU will be strongly perturbed by the turbulent fluctuations. This is confirmed by preliminary N-body simulations, as shown in the last panel of Figure 7.2.

The presence of these fluctuations is likely to hinder planet formation for several reasons. First, significant eccentricity jitter is added to the planetesimal which is not effectively damped by the gas disk. Second, they alter or destroy the weak phasing in the outer planetesimal disk. This is potentially more problematic than in single-star environments, as the randomization of the pericenter brings these planetesimals, which are already endowed with relatively high eccentricities from the binary perturbations, to collide on different phases of their orbits (potentially at speeds in the erosive regime). Finally, especially at higher values of A, there is a significant component of radial random walk (similarly to Laughlin et al. 2004).

We plan to conduct a future study to investigate this issue. A more precise model of the turbulent torques is the most pressing issue; although Equation 7.4 is a numerically convenient prescription, it is still an ad-hoc, order-of-magnitude ansatz. Full hydrodynamical

simulations will help characterize a more accurate parametrization of the turbulent torques, to be incorporated in the SPHIGA code.

Bibliography

Adams, F. C., Ruden, S. P., & Shu, F. H. 1989, *ApJ*, **347**, 959

Agol, E. & Steffen, J. H. 2007, *MNRAS*, **374**, 941

Agol, E., Steffen, J. H., Sari, R., & Clarkson, W. 2005, *Monthly Notices of the Royal Astronomical Society*, **359**, 567

Alibert, Y., Mordasini, C., & Benz, W. 2004, *A&A*, **417**, L25

Alonso, R., Barbieri, M., Rabus, M., Deeg, H., Belmonte, J., & Almenara, J. 2008, *Astronomy and Astrophysics*, **487**, L5

Alonso, R., Brown, T. M., Torres, G., Latham, D. W., Sozzetti, A., Mandushev, G., Belmonte, J. A., Charbonneau, D., Deeg, H. J., Dunham, E. W., O'Donovan, F. T., & Stefanik, R. P. 2004, *ApJ*, **613**, L153

Andrews, S. M. & Williams, J. P. 2005, *ApJ*, **631**, 1134

Anglada-Escudé, G., López-Morales, M., & Chambers, J. E. 2010, *ApJ*, **709**, 168

Armitage, P. J. 2010, *Astrophysics of Planet Formation*

Bakos, G. Á., Hartman, J. D., Torres, G., Kovács, G., Noyes, R. W., Latham, D. W., Sasselov, D. D., & Béky, B. 2011, *Detection and Dynamics of Transiting Exoplanets, St. Michel*

l'Observatoire, France, Edited by F. Bouchy; R. Díaz; C. Moutou; EPJ Web of Conferences, Volume 11, id.01002, **11**, 1002

Bakos, G. Á., Howard, A. W., Noyes, R. W., Hartman, J., Torres, G., Kovács, G., Fischer, D. A., Latham, D. W., Johnson, J. A., Marcy, G. W., Sasselov, D. D., Stefanik, R. P., Sipőcz, B., Kovács, G., Esquerdo, G. A., Pál, A., Lázár, J., Papp, I., & Sári, P. 2009, *The Astrophysical Journal*, **707**, 446

Balbus, S. A. & Hawley, J. F. 1991, *ApJ*, **376**, 214

Ballard, S., Fabrycky, D., Fressin, F., Charbonneau, D., Desert, J.-M., Torres, G., Marcy, G., Burke, C. J., Isaacson, H., Henze, C., Steffen, J. H., Ciardi, D. R., Howell, S. B., Cochran, W. D., Endl, M., Bryson, S. T., Rowe, J. F., Holman, M. J., Lissauer, J. J., Jenkins, J. M., Still, M., Ford, E. B., Christiansen, J. L., Middour, C. K., Haas, M. R., Li, J., Hall, J. R., McCauliff, S., Batalha, N. M., Koch, D. G., & Borucki, W. J. 2011, *ApJ*, **743**, 200

Balsara, D. S. 1995, *Journal of Computational Physics*, **121**, 357

Baluev, R. V. 2009, *MNRAS*, **393**, 969

Barnes, J. & Hut, P. 1986, *Nature*, **324**, 446

Barnes, R. & Greenberg, R. 2007, *ApJ*, **665**, L67

Barnes, R. & Raymond, S. N. 2004, *ApJ*, **617**, 569

Barnes, S. A. 2001, *ApJ*, **561**, 1095

Bate, M. R., Bonnell, I. A., & Price, N. M. 1995, *Monthly Notices of the Royal Astronomical Society*, **277**, 362

Batygin, K., Bodenheimer, P., & Laughlin, G. 2009, *The Astrophysical Journal Letters*, **704**, L49

Bean, J. L., Benedict, G. F., Charbonneau, D., Homeier, D., Taylor, D. C., McArthur, B., Seifahrt, A., Dreizler, S., & Reiners, A. 2008, *A&A*, **486**, 1039

Bean, J. L. & Seifahrt, A. 2009, *A&A*, **496**, 249

Beaugé, C., Michtchenko, T. A., & Ferraz-Mello, S. 2006, *Monthly Notices of the Royal Astronomical Society*, **365**, 1160

Benedict, G. F., McArthur, B. E., Forveille, T., Delfosse, X., Nelan, E., Butler, R. P., Spiesman, W., Marcy, G., Goldman, B., Perrier, C., Jefferys, W. H., & Mayor, M. 2002, *ApJ*, **581**, L115

Benedict, G. F., McArthur, B. E., Gatewood, G., Nelan, E., Cochran, W. D., Hatzes, A., Endl, M., Wittenmyer, R., Baliunas, S. L., Walker, G. A. H., Yang, S., Kürster, M., Els, S., & Paulson, D. B. 2006, *AJ*, **132**, 2206

Bennett, D. P. 2008, *Detection of Extrasolar Planets by Gravitational Microlensing*, pp 47–88

Binney, J. & Tremaine, S. 1987, *Galactic dynamics*, Princeton, NJ, Princeton University Press, 1987, 747 p.

Bodenheimer, P., Laughlin, G., & Lin, D. N. C. 2003, *ApJ*, **592**, 555

Borucki, W., Koch, D., Basri, G., Batalha, N., Brown, T., Caldwell, D., Caldwell, J., Christensen-Dalsgaard, J., Cochran, W., DeVore, E., Dunham, E. W., Dupree, A., Gautier, T. N. I., Geary, J., Gilliland, R., Gould, A., Howell, S., Jenkins, J., Kondo, Y., Latham, D. W., Marcy, G., Meibom, S., Kjeldsen, H., Lissauer, J., Monet, D., Morrison, D., Sasselov, D., Tarter, J., Boss, A., Brownlee, D., Owen, T., Buzasi, D., Charbonneau, D., Doyle, L., Fortney, J., Ford, E., Holman, M. J., Seager, S., Steffen, J. H., Welsh, W., Rowe, J., Anderson, H., Buchhave, L., Ciardi, D., Walkowicz, L., Sherry, W., Horch, E., Isaacson, H., Everett, M., Fischer, D., Torres, G., Johnson, J., Endl, M., Macqueen, P., Bryson, S., Dotson, J., Haas,

M., Kolodziejczak, J., Cleve, J. V., Chandrasekaran, H., Twicken, J., Quintana, E., Clarke, B., Allen, C., Li, J., Wu, H., Tenenbaum, P., Verner, E., Bruhweiler, F., Barnes, J., & Prsa, A. 2010a, *Science*, **327(5968)**, 977

Borucki, W., Koch, D., Basri, G., Batalha, N., Brown, T., Caldwell, D., Christensen-Dalsgaard, J., Cochran, W., Dunham, E. W., Gautier, T. N., Geary, J., Gilliland, R., Jenkins, J., Kondo, Y., Latham, D. W., Lissauer, J. J., & Monet, D. 2008, *Exoplanets: Detection*, **249**, 17

Borucki, W., Koch, D., Brown, T., Basri, G., Batalha, N., Caldwell, D., Cochran, W., Dunham, E. W., Gautier, T. N. I., Geary, J., Gilliland, R., Howell, S., Jenkins, J., Latham, D. W., Lissauer, J., Marcy, G., Monet, D., Rowe, J., & Sasselov, D. 2010b, *eprint arXiv:1001.0604*

Borucki, W. J., Koch, D., Jenkins, J., Sasselov, D., Gilliland, R., Batalha, N., Latham, D. W., Caldwell, D., Basri, G., Brown, T., Christensen-Dalsgaard, J., Cochran, W. D., DeVore, E., Dunham, E. W., Dupree, A. K., Gautier, T., Geary, J., Gould, A., Howell, S., Kjeldsen, H., Lissauer, J., Marcy, G., Meibom, S., Morrison, D., & Tarter, J. 2009, *Science*, **325**, 709

Boss, A. P. 1997, *Science*, **276**, 1836

Boss, A. P. 2000, *ApJ*, **536**, L101

Boué, G., Oshagh, M., Montalto, M., & Santos, N. C. 2012, *MNRAS*, **422**, L57

Brahic, A. 1976, *Journal of Computational Physics*, **22**, 171

Bryden, G., Beichman, C. A., Carpenter, J. M., Rieke, G. H., Stapelfeldt, K. R., Werner, M. W., Tanner, A. M., Lawler, S. M., Wyatt, M. C., Trilling, D. E., Su, K. Y. L., Blaylock, M., & Stansberry, J. A. 2009, *ApJ*, **705**, 1226

Bryden, G., Chen, X., Lin, D. N. C., Nelson, R. P., & Papaloizou, J. C. B. 1999, *ApJ*, **514**, 344

Butler, R. P., Marcy, G. W., Fischer, D. A., Brown, T. M., Contos, A. R., Korzennik, S. G., Nisenson, P., & Noyes, R. W. 1999, *ApJ*, **526**, 916

Butler, R. P., Marcy, G. W., Williams, E., McCarthy, C., Dosanjh, P., & Vogt, S. S. 1996, *PASP*, **108**, 500

Butler, R. P., Wright, J. T., Marcy, G. W., Fischer, D. A., Vogt, S. S., Tinney, C. G., Jones, H. R. A., Carter, B. D., Johnson, J. A., McCarthy, C., & Penny, A. J. 2006, *ApJ*, **646**, 505

Chambers, J. 2010, *Terrestrial Planet Formation*, pp 297–317

Chambers, J. E. & Migliorini, F. 1997, in *Bulletin of the American Astronomical Society*, Vol. 29, pp 1024–+

Charbonneau, D., Berta, Z. K., Irwin, J., Burke, C. J., Nutzman, P., Buchhave, L. A., Lovis, C., Bonfils, X., Latham, D. W., Udry, S., Murray-Clay, R. A., Holman, M. J., Falco, E. E., Winn, J. N., Queloz, D., Pepe, F., Mayor, M., Delfosse, X., & Forveille, T. 2009, *Nature*, **462(7275)**, 891

Charbonneau, D., Brown, T. M., Burrows, A., & Laughlin, G. 2007, *Protostars and Planets V*, pp 701–716

Charbonneau, D., Brown, T. M., Latham, D. W., & Mayor, M. 2000, *ApJ*, **529**, L45

Charbonneau, P. 1995, *ApJS*, **101**, 309

Charnoz, S., Thébault, P., & Brahic, A. 2001, *A&A*, **373**, 683

Chauvin, G., Lagrange, A.-M., Zuckerman, B., Dumas, C., Mouillet, D., Song, I., Beuzit, J.-L., Lowrance, P., & Bessell, M. S. 2005, *A&A*, **438**, L29

Christiansen, J. L., Ballard, S., Charbonneau, D., Madhusudhan, N., Seager, S., Holman, M. J., Wellnitz, D. D., Deming, D., A'Hearn, M. F., & the EPOXI team 2010, *The Astrophysical Journal*, **710**, 97

Cochran, W. D., Fabrycky, D. C., Torres, G., Fressin, F., Désert, J.-M., Ragozzine, D., Sasselov, D., Fortney, J. J., Rowe, J. F., Brugamyer, E. J., Bryson, S. T., Carter, J. A., Ciardi, D. R., Howell, S. B., Steffen, J. H., Borucki, W. J., Koch, D. G., Winn, J. N., Welsh, W. F., Uddin, K., Tenenbaum, P., Still, M., Seager, S., Quinn, S. N., Mullally, F., Miller, N., Marcy, G. W., MacQueen, P. J., Lucas, P., Lissauer, J. J., Latham, D. W., Knutson, H., Kinemuchi, K., Johnson, J. A., Jenkins, J. M., Isaacson, H., Howard, A., Horch, E., Holman, M. J., Henze, C. E., Haas, M. R., Gilliland, R. L., Gautier, III, T. N., Ford, E. B., Fischer, D. A., Everett, M., Endl, M., Demory, B.-O., Deming, D., Charbonneau, D., Caldwell, D., Buchhave, L., Brown, T. M., & Batalha, N. 2011, *ApJS*, **197**, 7

Correia, A. C. M., Udry, S., Mayor, M., Laskar, J., Naef, D., Pepe, F., Queloz, D., & Santos, N. C. 2005, *A&A*, **440**, 751

Cumming, A. 2004, *Monthly Notices of the Royal Astronomical Society*, **354**, 1165

Cumming, A., Butler, R. P., Marcy, G. W., Vogt, S. S., Wright, J. T., & Fischer, D. A. 2008, *PASP*, **120**, 531

Dawson, R. I. & Fabrycky, D. C. 2010, *ApJ*, **722**, 937

Deeming, T. J. 1975, *Ap&SS*, **36**, 137

Deming, D., Harrington, J., Laughlin, G., Seager, S., Navarro, S. B., Bowman, W. C., & Horning, K. 2007, *ApJ*, **667**, L199

Deming, D., Seager, S., Richardson, L. J., & Harrington, J. 2005, *Nature*, **434**, 740

Doyle, L. R., Carter, J. A., Fabrycky, D. C., Slawson, R. W., Howell, S. B., Winn, J. N., Orosz, J. A., Prsa, A., Welsh, W. F., Quinn, S. N., Latham, D., Torres, G., Buchhave, L. A., Marcy, G. W., Fortney, J. J., Shporer, A., Ford, E. B., Lissauer, J. J., Ragozzine, D., Rucker, M., Batalha, N., Jenkins, J. M., Borucki, W. J., Koch, D., Middour, C. K., Hall, J. R., McCauliff, S., Fanelli, M. N., Quintana, E. V., Holman, M. J., Caldwell, D. A., Still, M., Stefanik, R. P., Brown, W. R., Esquerdo, G. A., Tang, S., Furesz, G., Geary, J. C., Berlind, P., Calkins, M. L., Short, D. R., Steffen, J. H., Sasselov, D., Dunham, E. W., Cochran, W. D., Boss, A., Haas, M. R., Buzasi, D., & Fischer, D. 2011, *Science*, **333**, 1602

Dunham, E. W., Borucki, W. J., Koch, D. G., Batalha, N. M., Buchhave, L. A., Brown, T. M., Caldwell, D. A., Cochran, W. D., Endl, M., Fischer, D., Fűrész, G., Gautier, III, T. N., Geary, J. C., Gilliland, R. L., Gould, A., Howell, S. B., Jenkins, J. M., Kjeldsen, H., Latham, D. W., Lissauer, J. J., Marcy, G. W., Meibom, S., Monet, D. G., Rowe, J. F., & Sasselov, D. D. 2010, *ApJ*, **713**, L136

Eggenberger, A., Udry, S., Chauvin, G., Beuzit, J., Lagrange, A., Ségransan, D., & Mayor, M. 2007, *A&A*, **474**, 273

Fabrycky, D. & Tremaine, S. 2007, *ApJ*, **669**, 1298

Fabrycky, D. C., Ford, E. B., Steffen, J. H., Rowe, J. F., Carter, J. A., Moorhead, A. V., Batalha, N. M., Borucki, W. J., Bryson, S., Buchhave, L. A., Christiansen, J. L., Ciardi, D. R., Cochran, W. D., Endl, M., Fanelli, M. N., Fischer, D., Fressin, F., Geary, J., Haas, M. R., Hall, J. R., Holman, M. J., Jenkins, J. M., Koch, D. G., Latham, D. W., Li, J., Lissauer, J. J., Lucas, P., Marcy, G. W., Mazeh, T., McCauliff, S., Quinn, S., Ragozzine, D., Sasselov, D., & Shporer, A. 2012a, *ApJ*, **750**, 114

Fabrycky, D. C., Lissauer, J. J., Ragozzine, D., Rowe, J. F., Agol, E., Barclay, T., Batalha, N.,

Borucki, W., Ciardi, D. R., Ford, E. B., Geary, J. C., Holman, M. J., Jenkins, J. M., Li, J., Morehead, R. C., Shporer, A., Smith, J. C., Steffen, J. H., & Still, M. 2012b, *ArXiv e-prints*

Fischer, D. A., Laughlin, G., Butler, P., Marcy, G., Johnson, J., Henry, G., Valenti, J., Vogt, S., Ammons, M., Robinson, S., Spear, G., Strader, J., Driscoll, P., Fuller, A., Johnson, T., Manrao, E., McCarthy, C., Muñoz, M., Tah, K. L., Wright, J., Ida, S., Sato, B., Toyota, E., & Minniti, D. 2005, *ApJ*, **620**, 481

Ford, E. B. 2005, *The Astronomical Journal*, **129**, 1706

Ford, E. B. 2006, *The Astrophysical Journal*, **642**, 505

Ford, E. B. 2009, *New Astronomy*, **14**, 406

Ford, E. B., Fabrycky, D. C., Steffen, J. H., Carter, J. A., Fressin, F., Holman, M. J., Lissauer, J. J., Moorhead, A. V., Morehead, R. C., Ragozzine, D., Rowe, J. F., Welsh, W. F., Allen, C., Batalha, N. M., Borucki, W. J., Bryson, S. T., Buchhave, L. A., Burke, C. J., Caldwell, D. A., Charbonneau, D., Clarke, B. D., Cochran, W. D., Désert, J.-M., Endl, M., Everett, M. E., Fischer, D. A., Gautier, III, T. N., Gilliland, R. L., Jenkins, J. M., Haas, M. R., Horch, E., Howell, S. B., Ibrahim, K. A., Isaacson, H., Koch, D. G., Latham, D. W., Li, J., Lucas, P., MacQueen, P. J., Marcy, G. W., McCauliff, S., Mullally, F. R., Quinn, S. N., Quintana, E., Shporer, A., Still, M., Tenenbaum, P., Thompson, S. E., Torres, G., Twicken, J. D., Wohler, B., & the Kepler Science Team 2012, *ApJ*, **750**, 113

Ford, E. B. & Gaudi, B. S. 2006, *The Astrophysical Journal*, **652**, L137

Ford, E. B., Rowe, J. F., Fabrycky, D. C., Carter, J. A., Holman, M. J., Lissauer, J. J., Ragozzine, D., Steffen, J. H., Batalha, N. M., Borucki, W. J., Bryson, S., Caldwell, D. A., Dunham, E. W., Gautier, III, T. N., Jenkins, J. M., Koch, D. G., Li, J., Lucas, P., Marcy,

G. W., McCauliff, S., Mullally, F. R., Quintana, E., Still, M., Tenenbaum, P., Thompson, S. E., & Twicken, J. D. 2011, *ApJS*, **197**, 2

Fragner, M. M., Nelson, R. P., & Kley, W. 2011, *A&A*, **528**, A40+

Gary, B. 2009, *http://brucegary.net/AXA/x.htm*

Gautier, III, T. N., Charbonneau, D., Rowe, J. F., Marcy, G. W., Isaacson, H., Torres, G., Fressin, F., Rogers, L. A., Désert, J.-M., Buchhave, L. A., Latham, D. W., Quinn, S. N., Ciardi, D. R., Fabrycky, D. C., Ford, E. B., Gilliland, R. L., Walkowicz, L. M., Bryson, S. T., Cochran, W. D., Endl, M., Fischer, D. A., Howell, S. B., Horch, E. P., Barclay, T., Batalha, N., Borucki, W. J., Christiansen, J. L., Geary, J. C., Henze, C. E., Holman, M. J., Ibrahim, K., Jenkins, J. M., Kinemuchi, K., Koch, D. G., Lissauer, J. J., Sanderfer, D. T., Sasselov, D. D., Seager, S., Silverio, K., Smith, J. C., Still, M., Stumpe, M. C., Tenenbaum, P., & Van Cleve, J. 2012, *ApJ*, **749**, 15

Gilliland, R. L. & Baliunas, S. L. 1987, *ApJ*, **314**, 766

Gilliland, R. L., Chaplin, W. J., Dunham, E. W., Argabright, V. S., Borucki, W. J., Basri, G., Bryson, S. T., Buzasi, D. L., Caldwell, D. A., Elsworth, Y. P., Jenkins, J. M., Koch, D. G., Kolodziejczak, J., Miglio, A., van Cleve, J., Walkowicz, L. M., & Welsh, W. F. 2011, *ApJS*, **197**, 6

Gillon, M. 2009, *ArXiv e-prints*

Gillon, M., Deming, D., Demory, B.-O., Lovis, C., Seager, S., Mayor, M., Pepe, F., Queloz, D., Segransan, D., Udry, S., Delmelle, S., & Magain, P. 2010, *A&A*, **518**, A25

Gingold, R. A. & Monaghan, J. J. 1977, *MNRAS*, **181**, 375

Goldreich, P. & Tremaine, S. 1980, *ApJ*, **241**, 425

Grant, R. 1852, *The Sources of Science, New York: Johnson, 1966, Reprint from the London edition 1852*, pp –

Gregory, P. C. 2005, *ApJ*, **631**, 1198

Gregory, P. C. 2005, *Bayesian Logical Data Analysis for the Physical Sciences: A Comparative Approach with 'Mathematica' Support*

Guedes, J. M., Rivera, E. J., Davis, E., Laughlin, G., Quintana, E. V., & Fischer, D. A. 2008, *ApJ*, **679**, 1582

Hayashi, C. 1981, *Progress of Theoretical Physics Supplement*, **70**, 35

Henry, G. W., Marcy, G. W., Butler, R. P., & Vogt, S. S. 2000, *ApJ*, **529**, L41

Hernquist, L. & Katz, N. 1989, *Astrophysical Journal Supplement Series (ISSN 0067-0049)*, **70**, 419

Heyl, J. S. & Gladman, B. J. 2007, *Monthly Notices of the Royal Astronomical Society*, **377**, 1511

Holman, M. J., Fabrycky, D. C., Ragozzine, D., Ford, E. B., Steffen, J. H., Welsh, W. F., Lissauer, J. J., Latham, D. W., Marcy, G. W., Walkowicz, L. M., Batalha, N. M., Jenkins, J. M., Rowe, J. F., Cochran, W. D., Fressin, F., Torres, G., Buchhave, L. A., Sasselov, D. D., Borucki, W. J., Koch, D. G., Basri, G., Brown, T. M., Caldwell, D. A., Charbonneau, D., Dunham, E. W., Gautier, T. N., Geary, J. C., Gilliland, R. L., Haas, M. R., Howell, S. B., Ciardi, D. R., Endl, M., Fischer, D., Fürész, G., Hartman, J. D., Isaacson, H., Johnson, J. A., MacQueen, P. J., Moorhead, A. V., Morehead, R. C., & Orosz, J. A. 2010, *Science*, **330**, 51

Holman, M. J. & Murray, N. W. 2005, *Science*, **307**, 1288

Holman, M. J. & Wiegert, P. A. 1999, *AJ*, **117**, 621

Horne, J. H. & Baliunas, S. L. 1986, *ApJ*, **302**, 757

Howard, A. W., Johnson, J. A., Marcy, G. W., Fischer, D. A., Wright, J. T., Henry, G. W., Isaacson, H., Valenti, J. A., Anderson, J., & Piskunov, N. E. 2011, *ApJ*, **726**, 73

Hubickyj, O., Bodenheimer, P., & Lissauer, J. J. 2005, *Icarus*, **179**, 415

Hut, P., Makino, J., & McMillan, S. 1995, *ApJ*, **443**, L93

Ida, S., Guillot, T., & Morbidelli, A. 2008, *ApJ*, **686**, 1292

Ida, S. & Lin, D. N. C. 2004, *ApJ*, **604**, 388

Jenkins, J. M., Borucki, W. J., Koch, D. G., Marcy, G. W., Cochran, W. D., Welsh, W. F., Basri, G., Batalha, N. M., Buchhave, L. A., Brown, T. M., Caldwell, D. A., Dunham, E. W., Endl, M., Fischer, D. A., Gautier, III, T. N., Geary, J. C., Gilliland, R. L., Howell, S. B., Isaacson, H., Johnson, J. A., Latham, D. W., Lissauer, J. J., Monet, D. G., Rowe, J. F., Sasselov, D. D., Howard, A. W., MacQueen, P., Orosz, J. A., Chandrasekaran, H., Twicken, J. D., Bryson, S. T., Quintana, E. V., Clarke, B. D., Li, J., Allen, C., Tenenbaum, P., Wu, H., Meibom, S., Klaus, T. C., Middour, C. K., Cote, M. T., McCauliff, S., Girouard, F. R., Gunter, J. P., Wohler, B., Hall, J. R., Ibrahim, K., Kamal Uddin, A., Wu, M. S., Bhavsar, P. A., Van Cleve, J., Pletcher, D. L., Dotson, J. L., & Haas, M. R. 2010, *ApJ*, **724**, 1108

Jones, H. R. A., Butler, R. P., Tinney, C. G., O'Toole, S., Wittenmyer, R., Henry, G. W., Meschiari, S., Vogt, S., Rivera, E., Laughlin, G., Carter, B. D., Bailey, J., & Jenkins, J. S. 2010, *MNRAS*, **403**, 1703

Jurić, M. & Tremaine, S. 2008, *ApJ*, **686**, 603

Kalas, P., Graham, J. R., Chiang, E., Fitzgerald, M. P., Clampin, M., Kite, E. S., Stapelfeldt, K., Marois, C., & Krist, J. 2008, *Science*, **322**, 1345

Kipping, D. M. 2010, *MNRAS*, **407**, 301

Kipping, D. M., Fossey, S. J., & Campanella, G. 2009, *Monthly Notices of the Royal Astronomical Society*, **400**, 398

Kley, W., Lee, M. H., Murray, N., & Peale, S. J. 2005, *A&A*, **437**, 727

Kley, W. & Nelson, R. P. 2012, *ArXiv e-prints*

Kobayashi, H. & Ida, S. 2001, *Icarus*, **153**, 416

Koch, D. G., Borucki, W., Dunham, E. W., Geary, J., Gilliland, R., Jenkins, J., Latham, D. W., Bachtell, E., Berry, D., Deininger, W., Duren, R., Gautier, T. N., Gillis, L., Mayer, D., Miller, C. D., Shafer, D., Sobeck, C. K., Stewart, C., & Weiss, M. 2004, *Optical*, **5487**, 1491

Koch, D. G., Borucki, W. J., Basri, G., Batalha, N. M., Brown, T. M., Caldwell, D., Christensen-Dalsgaard, J., Cochran, W. D., DeVore, E., Dunham, E. W., Gautier, III, T. N., Geary, J. C., Gilliland, R. L., Gould, A., Jenkins, J., Kondo, Y., Latham, D. W., Lissauer, J. J., Marcy, G., Monet, D., Sasselov, D., Boss, A., Brownlee, D., Caldwell, J., Dupree, A. K., Howell, S. B., Kjeldsen, H., Meibom, S., Morrison, D., Owen, T., Reitsema, H., Tarter, J., Bryson, S. T., Dotson, J. L., Gazis, P., Haas, M. R., Kolodziejczak, J., Rowe, J. F., Van Cleve, J. E., Allen, C., Chandrasekaran, H., Clarke, B. D., Li, J., Quintana, E. V., Tenenbaum, P., Twicken, J. D., & Wu, H. 2010, *ApJ*, **713**, L79

Kokubo, E. & Ida, S. 2000, *Icarus*, **143**, 15

Laskar, J. & Correia, A. C. M. 2009, *A&A*, **496**, L5

Latham, D. W., Borucki, W. J., Koch, D. G., Brown, T. M., Buchhave, L. A., Basri, G., Batalha, N. M., Caldwell, D. A., Cochran, W. D., Dunham, E. W., Fűrész, G., Gautier, III, T. N.,

Geary, J. C., Gilliland, R. L., Howell, S. B., Jenkins, J. M., Lissauer, J. J., Marcy, G. W., Monet, D. G., Rowe, J. F., & Sasselov, D. D. 2010, *ApJ*, **713**, L140

Laughlin, G. & Chambers, J. E. 2001, *ApJ*, **551**, L109

Laughlin, G., Deming, D., Langton, J., Kasen, D., Vogt, S., Butler, P., Rivera, E., & Meschiari, S. 2009, *Nature*, **457**, 562

Laughlin, G., Korchagin, V., & Adams, F. C. 1997, *ApJ*, **477**, 410

Laughlin, G. & Rozyczka, M. 1996, *ApJ*, **456**, 279

Laughlin, G., Steinacker, A., & Adams, F. C. 2004, *ApJ*, **608**, 489

Lee, M. H. & Peale, S. J. 2002, *The Astrophysical Journal*, **567**, 596

Léger, A., Rouan, D., Schneider, J., Barge, P., Fridlund, M., Samuel, B., Ollivier, M., Guenther, E., Deleuil, M., Deeg, H. J., Auvergne, M., Alonso, R., Aigrain, S., Alapini, A., Almenara, J. M., Baglin, A., Barbieri, M., Bruntt, H., Bordé, P., Bouchy, F., Cabrera, J., Catala, C., Carone, L., Carpano, S., Csizmadia, S., Dvorak, R., Erikson, A., Ferraz-Mello, S., Foing, B., Fressin, F., Gandolfi, D., Gillon, M., Gondoin, P., Grasset, O., Guillot, T., Hatzes, A., Hébrard, G., Jorda, L., Lammer, H., Llebaria, A., Loeillet, B., Mayor, M., Mazeh, T., Moutou, C., Pätzold, M., Pont, F., Queloz, D., Rauer, H., Renner, S., Samadi, R., Shporer, A., Sotin, C., Tingley, B., Wuchterl, G., Adda, M., Agogu, P., Appourchaux, T., Ballans, H., Baron, P., Beaufort, T., Bellenger, R., Berlin, R., Bernardi, P., Blouin, D., Baudin, F., Bodin, P., Boisnard, L., Boit, L., Bonneau, F., Borzeix, S., Briet, R., Buey, J.-T., Butler, B., Cailleau, D., Cautain, R., Chabaud, P.-Y., Chaintreuil, S., Chiavassa, F., Costes, V., Parrho, V. C., de Oliveira Fialho, F., Decaudin, M., Defise, J.-M., Djalal, S., Epstein, G., Exil, G.-E., Fauré, C., Fenouillet, T., Gaboriaud, A., Gallic, A., Gamet, P., Gavalda, P., Grolleau, E., Gruneisen, R., Gueguen, L., Guis, V., Guivarc'h, V., Guterman, P., Hallouard, D., Hasiba, J., Heuripeau,

F., Huntzinger, G., Hustaix, H., Imad, C., Imbert, C., Johlander, B., Jouret, M., Journoud, P., Karioty, F., Kerjean, L., Lafaille, V., Lafond, L., Lam-Trong, T., Landiech, P., Lapeyrere, V., Larqué, T., Laudet, P., Lautier, N., Lecann, H., Lefevre, L., Leruyet, B., Levacher, P., Magnan, A., Mazy, E., Mertens, F., Mesnager, J.-M., Meunier, J.-C., Michel, J.-P., Monjoin, W., Naudet, D., Nguyen-Kim, K., Orcesi, J.-L., Ottacher, H., Perez, R., Peter, G., Plasson, P., Plesseria, J.-Y., Pontet, B., Pradines, A., Quentin, C., Reynaud, J.-L., Rolland, G., Rollenhagen, F., Romagnan, R., Russ, N., Schmidt, R., Schwartz, N., Sebbag, I., Sedes, G., Smit, H., Steller, M. B., Sunter, W., Surace, C., Tello, M., Tiphène, D., Toulouse, P., Ulmer, B., Vandermarcq, O., Vergnault, E., Vuillemin, A., & Zanatta, P. 2009, *Astronomy and Astrophysics*, **506**, 287

Lin, D. N. C., Bodenheimer, P., & Richardson, D. C. 1996, *Nature*, **380**, 606

Lin, D. N. C. & Papaloizou, J. 1979, *MNRAS*, **186**, 799

Lin, D. N. C. & Papaloizou, J. C. B. 1993, in E. H. Levy & J. I. Lunine (eds.), *Protostars and Planets III*, pp 749–835

Lin, M.-K. & Papaloizou, J. C. B. 2011, *MNRAS*, **415**, 1445

Lin, M.-K. & Papaloizou, J. C. B. 2012, *MNRAS*, **421**, 780

Lissauer, J. J. 1993, *ARA&A*, **31**, 129

Lissauer, J. J., Fabrycky, D. C., Ford, E. B., Borucki, W. J., Fressin, F., Marcy, G. W., Orosz, J. A., Rowe, J. F., Torres, G., Welsh, W. F., Batalha, N. M., Bryson, S. T., Buchhave, L. A., Caldwell, D. A., Carter, J. A., Charbonneau, D., Christiansen, J. L., Cochran, W. D., Desert, J.-M., Dunham, E. W., Fanelli, M. N., Fortney, J. J., Gautier, III, T. N., Geary, J. C., Gilliland, R. L., Haas, M. R., Hall, J. R., Holman, M. J., Koch, D. G., Latham, D. W., Lopez,

E., McCauliff, S., Miller, N., Morehead, R. C., Quintana, E. V., Ragozzine, D., Sasselov, D., Short, D. R., & Steffen, J. H. 2011, *Nature*, **470**, 53

Lodato, G. & Price, D. J. 2010, *Monthly Notices of the Royal Astronomical Society*, **405**, 1212

Lodato, G. & Rice, W. K. M. 2004, *Monthly Notices of the Royal Astronomical Society*, **351**, 630

Lovis, C. & Fischer, D. 2010, *Exoplanets*, pp 27–53, Tucson, AZ: University of Arizona Press

Lovis, C., Mayor, M., Pepe, F., Alibert, Y., Benz, W., Bouchy, F., Correia, A. C. M., Laskar, J., Mordasini, C., Queloz, D., Santos, N. C., Udry, S., Bertaux, J.-L., & Sivan, J.-P. 2006, *Nature*, **441**, 305

Lucy, L. B. 1977, *AJ*, **82**, 1013

Maciejewski, G., Dimitrov, D., Neuhäuser, R., Tetzlaff, N., Niedzielski, A., Raetz, S., Chen, W. P., Walter, F., Marka, C., Baar, S., Krejcová, T., Budaj, J., Krushevska, V., Tachihara, K., Takahashi, H., & Mugrauer, M. 2011, *MNRAS*, **411**, 1204

Marcy, G. W., Butler, R. P., Fischer, D., Vogt, S. S., Lissauer, J. J., & Rivera, E. J. 2001, *ApJ*, **556**, 296

Marcy, G. W., Butler, R. P., Vogt, S. S., Fischer, D., & Lissauer, J. J. 1998, *ApJ*, **505**, L147

Marcy, G. W., Butler, R. P., Vogt, S. S., Fischer, D. A., Henry, G. W., Laughlin, G., Wright, J. T., & Johnson, J. A. 2005, *ApJ*, **619**, 570

Mardling, R. A. 2010, *MNRAS*, **407**, 1048

Marois, C., Macintosh, B., Barman, T., Zuckerman, B., Song, I., Patience, J., Lafrenière, D., & Doyon, R. 2008, *Science*, **322**, 1348

Marzari, F., Baruteau, C., Scholl, H., & Thebault, P. 2012, *A&A*, **539**, A98

Marzari, F. & Scholl, H. 2000, *The Astrophysical Journal*, **543**, 328

Marzari, F., Scholl, H., Thébault, P., & Baruteau, C. 2009, *Astronomy and Astrophysics*, **508**, 1493

Marzari, F., Thébault, P., & Scholl, H. 2008, *ApJ*, **681**, 1599

Mayor, M., Bonfils, X., Forveille, T., Delfosse, X., Udry, S., Bertaux, J.-L., Beust, H., Bouchy, F., Lovis, C., Pepe, F., Perrier, C., Queloz, D., & Santos, N. C. 2009a, *Astronomy and Astrophysics*, **507**, 487

Mayor, M., Pepe, F., Queloz, D., Bouchy, F., Rupprecht, G., Lo Curto, G., Avila, G., Benz, W., Bertaux, J.-L., Bonfils, X., Dall, T., Dekker, H., Delabre, B., Eckert, W., Fleury, M., Gilliotte, A., Gojak, D., Guzman, J. C., Kohler, D., Lizon, J.-L., Longinotti, A., Lovis, C., Megevand, D., Pasquini, L., Reyes, J., Sivan, J.-P., Sosnowska, D., Soto, R., Udry, S., van Kesteren, A., Weber, L., & Weilenmann, U. 2003, *The Messenger*, **114**, 20

Mayor, M. & Queloz, D. 1995, *Nature*, **378**, 355

Mayor, M., Udry, S., Lovis, C., Pepe, F., Queloz, D., Benz, W., Bertaux, J.-L., Bouchy, F., Mordasini, C., & Segransan, D. 2009b, *A&A*, **493**, 639

Meschiari, S. & Laughlin, G. 2008, *ApJ*, **679**, L135

Meschiari, S., Laughlin, G., Vogt, S. S., Butler, R. P., Rivera, E. J., Haghighipour, N., & Jalowiczor, P. 2011, *ApJ*, **727**, 117

Meschiari, S. & Laughlin, G. P. 2010, *ApJ*, **718**, 543

Meschiari, S., Wolf, A. S., Rivera, E., Laughlin, G., Vogt, S., & Butler, P. 2009, *Publications of the Astronomical Society of the Pacific*, **121**, 1016

Miller-Ricci, E., Rowe, J. F., Sasselov, D., Matthews, J. M., Guenther, D. B., Kuschnig, R., Moffat, A. F. J., Rucinski, S. M., Walker, G. A. H., & Weiss, W. W. 2008, *The Astrophysical Journal*, **682**, 586

Miralda-Escudé, J. 2002, *The Astrophysical Journal*, **564**, 1019

Monaghan, J. J. 1992, *ARA&A*, **30**, 543

Monaghan, J. J. & Gingold, R. A. 1983, *Journal of Computational Physics*, **52**, 374

Mordasini, C., Alibert, Y., Benz, W., Klahr, H., & Henning, T. 2012, *A&A*, **541**, A97

Mordasini, C., Alibert, Y., Benz, W., & Naef, D. 2009, *A&A*, **501**, 1161

Moriwaki, K. & Nakagawa, Y. 2004, *ApJ*, **609**, 1065

Morris, J. P. & Monaghan, J. J. 1997, *Journal of Computational Physics*, **136**, 41

Murray, C. D. & Dermott, S. F. 2000, *Solar System Dynamics*

Murray, J. R. 1996, *Monthly Notices of the Royal Astronomical Society*, **279**, 402

Naef, D., Mayor, M., Beuzit, J. L., Perrier, C., Queloz, D., Sivan, J. P., & Udry, S. 2004, *A&A*, **414**, 351

Nascimbeni, V., Piotto, G., Bedin, L. R., Damasso, M., Malavolta, L., & Borsato, L. 2011, *A&A*, **532**, A24

Nelson, A. F. 2000, *ApJ*, **537**, L65

Nelson, A. F., Benz, W., Adams, F. C., & Arnett, D. 1998, *ApJ*, **502**, 342

Nelson, R. P. & Gressel, O. 2010, *MNRAS*, **409**, 639

Nelson, R. P. & Papaloizou, J. C. B. 2002, *Monthly Notices of the Royal Astronomical Society*, **333**, L26

Nesvorný, D. 2009, *The Astrophysical Journal*, **701**, 1116

Nesvorný, D. & Beaugé, C. 2010, *The Astrophysical Journal Letters*, **709**, L44, Notes

Nesvorný, D., Kipping, D. M., Buchhave, L. A., Bakos, G. Á., Hartman, J., & Schmitt, A. R. 2012, *Science*

Nesvorný, D. & Morbidelli, A. 2008, *The Astrophysical Journal*, **688**, 636

Nordström, B., Mayor, M., Andersen, J., Holmberg, J., Pont, F., Jørgensen, B. R., Olsen, E. H., Udry, S., & Mowlavi, N. 2004, *A&A*, **418**, 989

Paardekooper, S.-J. & Leinhardt, Z. M. 2010, *MNRAS*, **403**, L64

Paardekooper, S.-J., Thébault, P., & Mellema, G. 2008, *Monthly Notices of the Royal Astronomical Society*, **386**, 973

Pál, A., Bakos, G., Torres, G., Noyes, R., Latham, D., Kovács, G., Marcy, G., Fischer, D., Butler, R., Sasselov, D., Sipőcz, B., Esquerdo, G., Kovács, G., Stefanik, R., Lázár, J., Papp, I., & Sári, P. 2008, *The Astrophysical Journal*, **680**, 1450

Papaloizou, J. C. B. & Lin, D. N. C. 1995, *ARA&A*, **33**, 505

Papaloizou, J. C. B., Nelson, R. P., Kley, W., Masset, F. S., & Artymowicz, P. 2007, *Protostars and Planets V*, pp 655–668

Papaloizou, J. C. B. & Szuszkiewicz, E. 2005, *Monthly Notices of the Royal Astronomical Society*, **363**, 153

Papaloizou, J. C. B. & Terquem, C. 2006, *Reports on Progress in Physics*, **69**, 119

Payne, M. J., Ford, E. B., & Veras, D. 2010, *The Astrophysical Journal Letters*, **712**, L86

Pepe, F., Lovis, C., Ségransan, D., Benz, W., Bouchy, F., Dumusque, X., Mayor, M., Queloz, D., Santos, N. C., & Udry, S. 2011, *A&A*, **534**, A58

Pierens, A. & Nelson, R. P. 2007, *A&A*, **472**, 993

Pierens, A. & Nelson, R. P. 2008a, *A&A*, **478**, 939

Pierens, A. & Nelson, R. P. 2008b, *A&A*, **483**, 633

Pollack, J. B., Hubickyj, O., Bodenheimer, P., Lissauer, J. J., Podolak, M., & Greenzweig, Y. 1996, *Icarus*, **124**, 62

Pont, F., Hébrard, G., Irwin, J. M., Bouchy, F., Moutou, C., Ehrenreich, D., Guillot, T., Aigrain, S., Bonfils, X., Berta, Z., Boisse, I., Burke, C., Charbonneau, D., Delfosse, X., Desort, M., Eggenberger, A., Forveille, T., Lagrange, A.-M., Lovis, C., Nutzman, P., Pepe, F., Perrier, C., Queloz, D., Santos, N. C., Ségransan, D., Udry, S., & Vidal-Madjar, A. 2009, *A&A*, **502**, 695

Pourbaix, D., Nidever, D., McCarthy, C., Butler, R. P., Tinney, C. G., Marcy, G. W., Jones, H. R. A., Penny, A. J., Carter, B. D., Bouchy, F., Pepe, F., Hearnshaw, J. B., Skuljan, J., Ramm, D., & Kent, D. 2002, *A&A*, **386**, 280

Press, W. H., Teukolsky, S. A., Vetterling, W. T., & Flannery, B. P. 1992, *Cambridge: University Press*

Price, D. J. 2004, *Ph.D. thesis*, Institute of Astronomy, Madingley Rd, Cambridge, CB2 0HA, UK ¡EMAIL¿dprice@cantab.net¡/EMAIL¿

Price, D. J. 2012, *Journal of Computational Physics*, **231**, 759

Queloz, D., Bouchy, F., Moutou, C., Hatzes, A., Hébrard, G., Alonso, R., Auvergne, M., Baglin, A., Barbieri, M., Barge, P., Benz, W., Bordé, P., Deeg, H. J., Deleuil, M., Dvorak, R., Erikson, A., Mello, S. F., Fridlund, M., Gandolfi, D., Gillon, M., Guenther, E., Guillot, T., Jorda, L., Hartmann, M., Lammer, H., Léger, A., Llebaria, A., Lovis, C., Magain, P., Mayor, M., Mazeh, T., Ollivier, M., Pätzold, M., Pepe, F., Rauer, H., Rouan, D., Schneider, J., Segransan, D., Udry, S., & Wuchterl, G. 2009, *Astronomy and Astrophysics*, **506**, 303

Quintana, E. V. & Lissauer, J. J. 2006, *Icarus*, **185**, 1

Quintana, E. V., Lissauer, J. J., Chambers, J. E., & Duncan, M. J. 2002, *ApJ*, **576**, 982

Rivera, E. J., Laughlin, G., Butler, R. P., Vogt, S. S., Haghighipour, N., & Meschiari, S. 2010, *ApJ*, **719**, 890

Rivera, E. J., Lissauer, J. J., Butler, R. P., Marcy, G. W., Vogt, S. S., Fischer, D. A., Brown, T. M., Laughlin, G., & Henry, G. W. 2005, *ApJ*, **634**, 625

Rosswog, S. 2009, *New Astronomy Reviews*, **53**, 78

Rosswog, S. & Price, D. 2007, *Monthly Notices of the Royal Astronomical Society*, **379**, 915

Sándor, Z. & Kley, W. 2006, *A&A*, **451**, L31

Sándor, Z., Kley, W., & Klagyivik, P. 2007, *A&A*, **472**, 981

Santos, N. C., Israelian, G., Mayor, M., Rebolo, R., & Udry, S. 2003, *A&A*, **398**, 363

Scargle, J. D. 1982, *ApJ*, **263**, 835

Scholl, H., Marzari, F., & Thébault, P. 2007, *MNRAS*, **380**, 1119

Sellwood, J. A. & Kahn, F. D. 1991, *MNRAS*, **250**, 278

Sellwood, J. A. & Lin, D. N. C. 1989, *MNRAS*, **240**, 991

Setiawan, J., Henning, T., Launhardt, R., Müller, A., Weise, P., & Kürster, M. 2008, *Nature*, **451**, 38

Shakura, N. I. & Sunyaev, R. A. 1973, *A&A*, **24**, 337

Shankland, P. D., Rivera, E. J., Laughlin, G., Blank, D. L., Price, A., Gary, B., Bissinger, R., Ringwald, F., White, G., Henry, G. W., McGee, P., Wolf, A. S., Carter, B., Lee, S., Biggs, J., Monard, B., & Ashley, M. C. B. 2006, *ApJ*, **653**, 700

Shu, F. H., Tremaine, S., Adams, F. C., & Ruden, S. P. 1990, *ApJ*, **358**, 495

Silvotti, R., Schuh, S., Janulis, R., Solheim, J.-E., Bernabei, S., Østensen, R., Oswalt, T. D., Bruni, I., Gualandi, R., Bonanno, A., Vauclair, G., Reed, M., Chen, C.-W., Leibowitz, E., Paparo, M., Baran, A., Charpinet, S., Dolez, N., Kawaler, S., Kurtz, D., Moskalik, P., Riddle, R., & Zola, S. 2007, *Nature*, **449**, 189

Slawson, R. W., Prša, A., Welsh, W. F., Orosz, J. A., Rucker, M., Batalha, N., Doyle, L. R., Engle, S. G., Conroy, K., Coughlin, J., Gregg, T. A., Fetherolf, T., Short, D. R., Windmiller, G., Fabrycky, D. C., Howell, S. B., Jenkins, J. M., Uddin, K., Mullally, F., Seader, S. E., Thompson, S. E., Sanderfer, D. T., Borucki, W., & Koch, D. 2011, *AJ*, **142**, 160

Sod, G. A. 1978, *Journal of Computational Physics*, **27**, 1

Steffen, J. H. & Agol, E. 2005, *Monthly Notices of the Royal Astronomical Society: Letters*, **364**, L96

Steffen, J. H. & Agol, E. 2007, *Transiting Extrapolar Planets Workshop ASP Conference Series*, **366**, 158

Stewart, S. T. & Leinhardt, Z. M. 2009, *ApJ*, **691**, L133

Stone, J. M., Gardiner, T. A., Teuben, P., Hawley, J. F., & Simon, J. B. 2008, *ApJS*, **178**, 137

Stone, J. M. & Norman, M. L. 1992, *ApJS*, **80**, 753

Takeda, G., Ford, E. B., Sills, A., Rasio, F. A., Fischer, D. A., & Valenti, J. A. 2007, *ApJS*, **168**, 297

Takeuchi, T., Miyama, S. M., & Lin, D. N. C. 1996, *ApJ*, **460**, 832

Tanner, A., Beichman, C., Bryden, G., Lisse, C., & Lawler, S. 2009, *ApJ*, **704**, 109

Thebault, P. 2011, *Celestial Mechanics and Dynamical Astronomy*, **111**, 29

Thébault, P., Marzari, F., & Scholl, H. 2002, *Astronomy and Astrophysics*, **384**, 594

Thébault, P., Marzari, F., & Scholl, H. 2006, *Icarus*, **183**, 193

Thébault, P., Marzari, F., & Scholl, H. 2008, *Monthly Notices of the Royal Astronomical Society*, **388**, 1528

Thébault, P., Marzari, F., Scholl, H., Turrini, D., & Barbieri, M. 2004, *Astronomy and Astrophysics*, **427**, 1097

Toomre, A. 1981, in *The structure and evolution of normal galaxies*, pp 111–136

Trilling, D. E., Bryden, G., Beichman, C. A., Rieke, G. H., Su, K. Y. L., Stansberry, J. A., Blaylock, M., Stapelfeldt, K. R., Beeman, J. W., & Haller, E. E. 2008, *ApJ*, **674**, 1086

Udry, S., Bonfils, X., Delfosse, X., Forveille, T., Mayor, M., Perrier, C., Bouchy, F., Lovis, C., Pepe, F., Queloz, D., & Bertaux, J.-L. 2007, *A&A*, **469**, L43

Udry, S., Bonfils, X., Delfosse, X., Forveille, T., Mayor, M., Perrier, C., Bouchy, F., Lovis, C., Pepe, F., Queloz, D., & Bertaux, J.-L. 2007, *A&A*, **469**, L43

Unwin, S. C., Shao, M., Tanner, A. M., Allen, R. J., Beichman, C. A., Boboltz, D., Catanzarite, J. H., Chaboyer, B. C., Ciardi, D. R., Edberg, S. J., Fey, A. L., Fischer, D. A., Gelino, C. R.,

Gould, A. P., Grillmair, C., Henry, T. J., Johnston, K. V., Johnston, K. J., Jones, D. L., Kulkarni, S. R., Law, N. M., Majewski, S. R., Makarov, V. V., Marcy, G. W., Meier, D. L., Olling, R. P., Pan, X., Patterson, R. J., Pitesky, J. E., Quirrenbach, A., Shaklan, S. B., Shaya, E. J., Strigari, L. E., Tomsick, J. A., Wehrle, A. E., & Worthey, G. 2008, *PASP*, **120**, 38

Valenti, J. A. & Fischer, D. A. 2005, *ApJS*, **159**, 141

Varnière, P., Quillen, A. C., & Frank, A. 2004, *ApJ*, **612**, 1152

Veras, D., Ford, E. B., & Payne, M. J. 2011, *ApJ*, **727**, 74

Vogt, S. S., Allen, S. L., Bigelow, B. C., Bresee, L., Brown, B., Cantrall, T., Conrad, A., Couture, M., Delaney, C., Epps, H. W., Hilyard, D., Hilyard, D. F., Horn, E., Jern, N., Kanto, D., Keane, M. J., Kibrick, R. I., Lewis, J. W., Osborne, J., Pardeilhan, G. H., Pfister, T., Ricketts, T., Robinson, L. B., Stover, R. J., Tucker, D., Ward, J., & Wei, M. Z. 1994, in D. L. C. E. R. C. Eds. (ed.), *Proc. SPIE Instrumentation in Astronomy VIII*, Vol. 2198, pp 362–+

Vogt, S. S., Butler, R. P., Marcy, G. W., Fischer, D. A., Henry, G. W., Laughlin, G., Wright, J. T., & Johnson, J. A. 2005, *ApJ*, **632**, 638

Vogt, S. S., Marcy, G. W., Butler, R. P., & Apps, K. 2000, *ApJ*, **536**, 902

Vogt, S. S., Wittenmyer, R. A., Butler, R. P., O'Toole, S., Henry, G. W., Rivera, E. J., Meschiari, S., Laughlin, G., Tinney, C. G., Jones, H. R. A., Bailey, J., Carter, B. D., & Batygin, K. 2010, *The Astrophysical Journal*, **708**, 1366

Weidenschilling, S. J. 1977, *MNRAS*, **180**, 57

Welsh, W. F., Orosz, J. A., Carter, J. A., Fabrycky, D. C., Ford, E. B., Lissauer, J. J., Prša, A., Quinn, S. N., Ragozzine, D., Short, D. R., Torres, G., Winn, J. N., Doyle, L. R., Barclay,

T., Batalha, N., Bloemen, S., Brugamyer, E., Buchhave, L. A., Caldwell, C., Caldwell, D. A., Christiansen, J. L., Ciardi, D. R., Cochran, W. D., Endl, M., Fortney, J. J., Gautier, III, T. N., Gilliland, R. L., Haas, M. R., Hall, J. R., Holman, M. J., Howard, A. W., Howell, S. B., Isaacson, H., Jenkins, J. M., Klaus, T. C., Latham, D. W., Li, J., Marcy, G. W., Mazeh, T., Quintana, E. V., Robertson, P., Shporer, A., Steffen, J. H., Windmiller, G., Koch, D. G., & Borucki, W. J. 2012, *Nature*, **481**, 475

Wetzstein, M., Nelson, A. F., Naab, T., & Burkert, A. 2009, *The Astrophysical Journal Supplement*, **184**, 298

Winn, J. N., Albrecht, S., Johnson, J. A., Torres, G., Cochran, W. D., Marcy, G. W., Howard, A. W., Isaacson, H., Fischer, D., Doyle, L., Welsh, W., Carter, J. A., Fabrycky, D. C., Ragozzine, D., Quinn, S. N., Shporer, A., Howell, S. B., Latham, D. W., Orosz, J., Prsa, A., Slawson, R. W., Borucki, W. J., Koch, D., Barclay, T., Boss, A. P., Christensen-Dalsgaard, J., Girouard, F. R., Jenkins, J., Klaus, T. C., Meibom, S., Morris, R. L., Sasselov, D., Still, M., & Van Cleve, J. 2011, *ApJ*, **741**, L1

Winn, J. N., Johnson, J. A., Howard, A. W., Marcy, G. W., Bakos, G. Á., Hartman, J., Torres, G., Albrecht, S., & Narita, N. 2010, *ApJ*, **718**, 575

Wittenmyer, R. A., Endl, M., Cochran, W. D., Levison, H. F., & Henry, G. W. 2009, *ApJS*, **182**, 97

Wittenmyer, R. A., Welsh, W. F., Orosz, J. A., Schultz, A. B., Kinzel, W., Kochte, M., Bruhweiler, F., Bennum, D., Henry, G. W., Marcy, G. W., Fischer, D. A., Butler, R. P., & Vogt, S. S. 2005, *ApJ*, **632**, 1157

Wolszczan, A. & Frail, D. A. 1992, *Nature*, **355**, 145

Wright, J. T. 2005, *PASP*, **117**, 657

Wright, J. T., Marcy, G. W., Butler, R. P., & Vogt, S. S. 2004, *ApJS*, **152**, 261

Wright, J. T., Marcy, G. W., Fischer, D. A., Butler, R. P., Vogt, S. S., Tinney, C. G., Jones, H. R. A., Carter, B. D., Johnson, J. A., McCarthy, C., & Apps, K. 2007, *ApJ*, **657**, 533

Wright, J. T., Upadhyay, S., Marcy, G. W., Fischer, D. A., Ford, E. B., & Johnson, J. A. 2009, *ApJ*, **693**, 1084

Wu, Y. & Goldreich, P. 2002, *ApJ*, **564**, 1024

Wu, Y. & Murray, N. 2003, *ApJ*, **589**, 605

Xie, J.-W., Payne, M. J., Thébault, P., Zhou, J.-L., & Ge, J. 2011, *ApJ*, **735**, 10

Xie, J.-W. & Zhou, J.-L. 2009, *ApJ*, **698**, 2066

Zsom, A., Sándor, Z., & Dullemond, C. P. 2011, *A&A*, **527**, A10

Appendix A

Radial velocity data

Star	Julian Date	RV [m/s]	Uncertainty [m/s]
HD128311	2450983.8269	-12.95	1.45
HD128311	2451200.13787	-21.49	1.92
HD128311	2451342.85836	62.75	2.05
HD128311	2451370.82904	105.66	1.88
HD128311	2451409.7466	125.71	1.62
HD128311	2451410.74909	118.14	2.01
HD128311	2451552.16457	68.78	1.85
HD128311	2451581.17009	13.35	1.64
HD128311	2451680.02544	-60.10	2.17
HD128311	2451974.16142	62.03	1.74
HD128311	2451982.15276	32.30	1.48
HD128311	2452003.02274	12.76	1.87
HD128311	2452003.90155	29.10	1.98
HD128311	2452005.13013	27.90	1.55
HD128311	2452061.87832	-40.29	1.54
HD128311	2452062.86745	-11.26	1.67
HD128311	2452096.77585	-28.60	1.85
HD128311	2452098.84799	-29.98	1.47
HD128311	2452128.76635	0.34	1.92
HD128311	2452162.72385	20.45	1.69
HD128311	2452308.17255	145.33	1.68
HD128311	2452333.15973	116.19	1.70
HD128311	2452335.11752	110.11	1.74
HD128311	2452362.99402	147.81	1.63
HD128311	2452364.0802	146.12	1.64
HD128311	2452389.99056	102.62	1.69
HD128311	2452390.95689	107.14	1.75
HD128311	2452445.82646	84.67	1.67

Continued on next page

Star	Julian Date	RV [m/s]	Uncertainty [m/s]
HD128311	2452486.82719	23.42	1.47
HD128311	2452488.77091	41.04	1.70
HD128311	2452515.73138	-28.04	1.74
HD128311	2452653.17621	-77.69	1.63
HD128311	2452654.16042	-91.95	2.01
HD128311	2452681.16095	-89.58	1.61
HD128311	2452683.06288	-63.52	1.61
HD128311	2452712.00457	-29.41	1.59
HD128311	2452712.9736	-42.69	1.97
HD128311	2452776.96054	-38.47	1.64
HD128311	2452777.88355	-20.30	1.52
HD128311	2452803.89833	-27.27	1.56
HD128311	2452804.95803	-30.48	1.37
HD128311	2452805.7997	-15.74	1.68
HD128311	2452806.8411	-10.35	1.43
HD128311	2452828.83471	-13.99	1.40
HD128311	2452832.73928	-8.04	1.41
HD128311	2452833.78281	-0.25	1.65
HD128311	2452834.8681	27.73	1.48
HD128311	2452848.79535	6.40	1.37
HD128311	2452849.79819	-8.08	1.40
HD128311	2452850.8023	-3.43	1.51
HD128311	2452897.71788	40.35	1.73
HD128311	2453015.15236	17.69	1.42
HD128311	2453016.16984	-32.96	1.51
HD128311	2453017.15716	-74.27	1.42
HD128311	2453018.1667	-43.69	1.51
HD128311	2453046.17351	-32.26	1.55
HD128311	2453069.13345	0.15	1.45
HD128311	2453072.09787	15.05	1.56
HD128311	2453074.0121	13.54	1.56
HD128311	2453077.14425	-3.24	1.69
HD128311	2453153.86726	73.53	1.42
HD128311	2453179.85039	79.98	1.37
HD128311	2453180.8187	99.09	1.39
HD128311	2453181.81424	110.06	1.39
HD128311	2453195.80089	86.89	1.37
HD128311	2453196.84413	111.83	1.42
HD128311	2453238.75863	118.34	1.32
HD128311	2453239.75002	113.54	1.36
HD128311	2453240.79285	118.12	1.36
HD128311	2453369.16921	97.05	1.32
HD128311	2453370.16823	106.49	1.45
HD128311	2453425.10853	0.00	1.33
HD128311	2453479.98589	-54.65	1.26
HD128311	2453480.82755	-36.91	1.29
HD128311	2453483.85825	-72.19	1.29

Continued on next page

Star	Julian Date	RV [m/s]	Uncertainty [m/s]
HD128311	2453550.83029	-88.99	1.27
HD128311	2453777.10722	47.45	1.45
HD128311	2453841.99566	27.22	1.52
HD128311	2453927.85578	-37.32	1.31
HD128311	2453984.74394	-0.37	1.61
HD128311	2454139.13869	104.91	1.46
HD128311	2454294.83885	66.98	1.37
HD128311	2454300.80781	32.49	1.34
HD128311	2454313.81904	24.38	1.34
HD128311	2454335.76089	-14.90	1.36
HD128311	2454343.73608	-30.73	1.68
HD128311	2454491.09174	-47.96	1.46
HD128311	2454545.06007	-64.56	1.31
HD128311	2454545.06167	-64.23	1.53
HD128311	2454545.06326	-64.43	1.45
HD128311	2454546.05466	-46.06	1.51
HD128311	2454546.05637	-40.64	1.48
HD128311	2454546.05822	-40.13	1.43
HD128311	2454547.04719	-23.55	1.53
HD128311	2454547.04965	-24.17	1.47
HD128311	2454547.05175	-23.06	1.45
HD128311	2454601.04411	-33.27	1.33
HD128311	2454601.04662	-36.03	1.43
HD128311	2454601.05113	-32.03	1.42
HD128311	2454601.90825	0.41	1.36
HD128311	2454601.90973	1.35	1.44
HD128311	2454601.91119	3.33	1.46
HD31253	2450838.75189	-1.44	1.97
HD31253	2451043.12399	-11.98	1.64
HD31253	2451073.03263	-10.12	1.43
HD31253	2451170.90537	6.52	1.78
HD31253	2451228.78516	11.64	1.38
HD31253	2451411.13343	3.54	2.19
HD31253	2451550.87137	-20.13	1.58
HD31253	2451581.85884	-4.86	1.69
HD31253	2451757.13309	7.45	1.58
HD31253	2451793.11793	8.50	1.78
HD31253	2451883.00052	2.05	1.80
HD31253	2451884.08282	-0.63	1.73
HD31253	2451898.01005	6.44	1.61
HD31253	2451898.99796	-2.59	1.54
HD31253	2451899.99476	1.53	1.48
HD31253	2451901.00753	-1.13	1.47
HD31253	2451973.74609	-7.57	1.83
HD31253	2451974.76077	-7.26	1.63
HD31253	2452235.85335	1.28	1.62
HD31253	2452536.0926	0.00	1.55

Continued on next page

Star	Julian Date	RV [m/s]	Uncertainty [m/s]
HD31253	2452575.9947	8.16	1.79
HD31253	2452898.09851	-11.51	1.50
HD31253	2453241.13429	5.63	1.52
HD31253	2453338.87214	-6.96	1.37
HD31253	2453339.99226	-7.29	1.50
HD31253	2453984.09331	16.52	1.44
HD31253	2454084.05142	14.81	1.55
HD31253	2454130.84528	7.33	1.60
HD31253	2454131.74964	12.59	1.62
HD31253	2454138.73395	2.24	1.57
HD31253	2454396.90266	-9.87	1.52
HD31253	2454398.01742	-2.69	1.67
HD31253	2454464.89612	3.30	1.61
HD31253	2454491.84891	14.32	1.44
HD31253	2454545.76603	15.23	1.50
HD31253	2454872.8586	4.84	0.89
HD31253	2455202.8103	-10.39	0.94
HD31253	2455257.82885	-9.67	0.73
HD218566	2450366.85498	4.96	1.16
HD218566	2450666.08942	-5.59	1.20
HD218566	2450690.03236	-5.47	1.27
HD218566	2450714.98919	2.14	1.22
HD218566	2450715.94463	3.39	1.16
HD218566	2450983.10118	2.63	1.14
HD218566	2451012.0364	5.34	1.35
HD218566	2451050.944	1.41	1.24
HD218566	2451071.96025	-1.88	1.19
HD218566	2451343.03657	-10.88	1.26
HD218566	2451369.03547	-9.64	1.23
HD218566	2451410.98964	-1.87	1.24
HD218566	2451440.89265	-3.74	1.36
HD218566	2451552.72759	-4.50	1.49
HD218566	2451900.73713	4.46	1.17
HD218566	2452096.07187	-0.44	1.28
HD218566	2452242.72507	-5.51	1.47
HD218566	2452488.04912	-4.53	1.57
HD218566	2452535.87165	1.94	1.27
HD218566	2452575.73785	1.66	1.63
HD218566	2452806.11771	9.82	1.47
HD218566	2452828.95884	6.88	1.33
HD218566	2452898.94265	-2.34	1.31
HD218566	2453195.98598	1.18	1.29
HD218566	2453303.88246	11.50	1.22
HD218566	2453603.06616	-9.95	1.34
HD218566	2453969.05624	-0.58	1.29
HD218566	2454279.10762	-6.49	1.08
HD218566	2454286.09348	-3.75	1.47

Continued on next page

Star	Julian Date	RV [m/s]	Uncertainty [m/s]
HD218566	2454295.07876	-2.51	1.24
HD218566	2454429.76038	6.90	1.19
HD218566	2454430.7458	6.11	1.28
HD218566	2454455.76108	-0.65	1.25
HD218566	2454456.75051	0.00	1.31
HD218566	2454457.73398	-2.57	1.35
HD218566	2454460.7473	-2.97	1.41
HD218566	2454461.77092	-0.23	1.12
HD218566	2454634.09288	16.87	1.32
HD218566	2454635.06583	13.14	1.09
HD218566	2454636.05577	13.31	1.25
HD218566	2454637.11095	11.36	1.38
HD218566	2454638.06397	15.15	1.20
HD218566	2454639.07829	13.05	1.21
HD218566	2454641.10707	12.30	1.13
HD218566	2454642.12403	8.85	1.27
HD218566	2454674.93117	-2.08	1.28
HD218566	2454688.94686	0.48	1.20
HD218566	2454689.96737	-0.90	1.47
HD218566	2454717.93868	-7.51	1.30
HD218566	2454719.95623	-4.17	1.24
HD218566	2455202.76214	-5.92	1.05
HD177830	2450276.02505	-16.32	0.94
HD177830	2450605.0434	-5.29	0.95
HD177830	2450666.88551	-17.61	1.03
HD177830	2450982.93951	0.32	1.11
HD177830	2451009.93206	-9.34	1.04
HD177830	2451068.81716	-30.65	0.95
HD177830	2451069.85005	-30.62	1.05
HD177830	2451070.8953	-28.30	1.00
HD177830	2451071.83118	-31.40	1.01
HD177830	2451072.82007	-27.97	1.00
HD177830	2451073.81795	-25.70	0.89
HD177830	2451074.80785	-33.00	0.98
HD177830	2451075.89814	-36.45	1.08
HD177830	2451311.10969	30.25	1.07
HD177830	2451312.10751	29.00	1.17
HD177830	2451313.10582	18.91	1.02
HD177830	2451314.12858	27.42	1.09
HD177830	2451341.95441	27.81	0.96
HD177830	2451367.91448	15.43	1.03
HD177830	2451368.90654	11.00	1.17
HD177830	2451369.91809	12.37	1.26
HD177830	2451409.84682	-14.23	1.07
HD177830	2451410.80182	-21.64	1.05
HD177830	2451411.7991	-10.96	1.09
HD177830	2451438.74187	-19.97	0.94

Continued on next page

Star	Julian Date	RV [m/s]	Uncertainty [m/s]
HD177830	2451439.76021	-21.77	0.94
HD177830	2451440.86979	-15.17	1.06
HD177830	2451441.72339	-17.34	1.08
HD177830	2451488.723	-18.59	1.07
HD177830	2451679.0564	37.36	0.97
HD177830	2451680.09782	34.51	0.98
HD177830	2451703.07726	44.29	1.10
HD177830	2451704.01943	50.70	1.13
HD177830	2451705.06457	40.08	1.16
HD177830	2451706.03088	43.40	1.04
HD177830	2451707.09076	38.21	0.99
HD177830	2451754.88242	27.80	1.07
HD177830	2451755.95107	20.80	0.91
HD177830	2451792.76348	10.88	1.06
HD177830	2451972.15641	-3.68	0.90
HD177830	2452008.12955	16.41	1.31
HD177830	2452031.09883	34.39	1.27
HD177830	2452061.99221	32.14	1.22
HD177830	2452094.87498	30.09	1.38
HD177830	2452128.88145	35.41	1.20
HD177830	2452445.97578	29.87	1.41
HD177830	2452536.83488	22.53	1.23
HD177830	2452832.84731	26.84	1.27
HD177830	2453180.04734	-6.76	1.07
HD177830	2453479.09184	-15.74	0.85
HD177830	2453546.9159	-23.27	0.95
HD177830	2453550.00554	-22.80	1.17
HD177830	2453551.0872	-22.60	0.95
HD177830	2453552.03093	-20.95	1.01
HD177830	2453842.1199	-3.60	0.97
HD177830	2453927.8927	-17.17	0.97
HD177830	2453982.89128	-14.60	0.88
HD177830	2454250.06746	-3.40	1.10
HD177830	2454309.06516	-27.53	1.19
HD177830	2454337.79715	-22.34	1.02
HD177830	2454343.76189	-26.49	0.97
HD177830	2454396.73487	-12.53	1.13
HD177830	2454546.12536	38.66	1.00
HD177830	2454547.13854	46.41	1.13
HD177830	2454549.12824	41.49	1.25
HD177830	2454601.10229	26.24	0.98
HD177830	2454634.02218	8.79	1.23
HD177830	2454641.86106	2.98	1.23
HD177830	2454673.06538	-7.09	1.18
HD177830	2454674.85466	-5.25	1.30
HD177830	2454702.932	-19.50	1.08
HD177830	2454721.8108	-24.46	1.18

Continued on next page

Star	Julian Date	RV [m/s]	Uncertainty [m/s]
HD177830	2454819.6869	6.80	1.08
HD177830	2454820.703	9.61	1.34
HD177830	2455022.06235	17.50	0.67
HD177830	2455024.07549	17.97	0.59
HD177830	2455049.9886	3.13	0.62
HD177830	2455051.99471	1.72	0.61
HD177830	2455053.99914	-2.06	0.61
HD177830	2455143.76056	-19.72	0.82
HD177830	2455166.72642	-16.43	0.79
HD177830	2455168.719	-22.96	0.80
HD177830	2455259.15406	17.08	0.65
HD99492	2450462.11396	-2.62	1.51
HD99492	2450546.98786	-3.46	1.39
HD99492	2450837.93254	-2.66	1.58
HD99492	2450862.89899	-4.70	1.51
HD99492	2450955.87664	-7.05	1.18
HD99492	2451172.1016	-4.12	1.59
HD99492	2451228.0359	-6.80	1.53
HD99492	2451311.81632	3.26	1.63
HD99492	2451544.17265	-6.23	1.27
HD99492	2451582.97494	0.43	1.34
HD99492	2451704.80591	-1.45	1.60
HD99492	2451898.154	-14.46	1.41
HD99492	2451973.05309	3.64	1.37
HD99492	2452095.75205	-0.65	1.55
HD99492	2452097.75372	-7.23	1.56
HD99492	2452333.13941	6.24	1.65
HD99492	2452334.07988	0.68	1.62
HD99492	2452334.96832	1.21	1.59
HD99492	2452364.06813	3.76	1.44
HD99492	2452445.76826	-6.52	1.50
HD99492	2452654.0096	4.61	1.66
HD99492	2452681.12348	-9.59	1.49
HD99492	2452711.85884	-1.61	1.38
HD99492	2452804.76559	-7.22	1.50
HD99492	2452805.8763	3.93	1.56
HD99492	2452806.76363	-0.41	1.34
HD99492	2452989.17142	-15.59	1.64
HD99492	2453015.11944	12.03	1.58
HD99492	2453016.13436	5.95	1.50
HD99492	2453017.12192	7.38	1.43
HD99492	2453044.12757	-0.95	1.56
HD99492	2453045.99907	5.04	1.49
HD99492	2453071.87076	-5.55	1.50
HD99492	2453073.94075	-6.96	1.58
HD99492	2453076.98361	-3.05	1.45
HD99492	2453153.80258	-0.24	0.90

Continued on next page

Star	Julian Date	RV [m/s]	Uncertainty [m/s]
HD99492	2453179.8227	0.03	1.05
HD99492	2453180.78204	5.64	1.82
HD99492	2453181.80817	0.78	1.38
HD99492	2453195.77591	-7.65	1.43
HD99492	2453196.79478	-5.25	1.47
HD99492	2453339.15773	9.35	1.25
HD99492	2453340.15072	6.86	1.26
HD99492	2453369.11509	8.69	1.26
HD99492	2453425.00213	4.15	0.99
HD99492	2453480.7608	-0.12	0.99
HD99492	2453725.10303	-6.29	0.99
HD99492	2453747.14058	11.43	0.98
HD99492	2453748.09771	12.59	0.98
HD99492	2453753.04165	1.96	0.97
HD99492	2453754.0226	-1.19	0.94
HD99492	2453775.98197	2.52	0.92
HD99492	2453776.97819	3.21	1.00
HD99492	2453777.95159	3.59	0.94
HD99492	2453779.9725	8.18	0.99
HD99492	2453806.9178	-7.76	0.84
HD99492	2453926.76507	-6.52	0.98
HD99492	2453927.76293	-10.13	0.91
HD99492	2454084.15598	4.58	0.99
HD99492	2454139.06371	8.81	0.84
HD99492	2454216.89805	-6.64	1.00
HD99492	2454246.79967	6.69	0.89
HD99492	2454248.81168	2.27	1.32
HD99492	2454250.80061	2.98	1.35
HD99492	2454251.80481	3.25	1.34
HD99492	2454255.7664	6.56	0.92
HD99492	2454277.74307	12.18	1.37
HD99492	2454278.74994	12.42	1.25
HD99492	2454279.74851	6.76	1.16
HD99492	2454285.75191	-1.62	1.33
HD99492	2454294.75867	3.43	1.39
HD99492	2454300.73897	-2.32	1.41
HD99492	2454455.10965	-3.78	1.11
HD99492	2454456.13058	-3.21	0.97
HD99492	2454491.02322	-6.50	1.49
HD99492	2454493.13458	-8.64	1.77
HD99492	2454544.98228	0.55	1.38
HD99492	2454546.96314	7.37	1.58
HD99492	2454547.87194	7.70	1.46
HD99492	2454548.84741	9.15	1.54
HD99492	2454635.75444	8.39	1.40
HD99492	2454638.75095	1.07	1.37
HD99492	2454967.94781	-8.07	0.84

Continued on next page

Star	Julian Date	RV [m/s]	Uncertainty [m/s]
HD99492	2454968.85572	-5.80	1.11
HD99492	2455021.77564	-2.02	1.07
HD99492	2455023.7545	1.08	1.72
HD99492	2455168.15578	-7.30	1.05
HD99492	2455201.10543	4.16	0.82
HD99492	2455203.03618	-4.10	0.78
HD99492	2455258.06769	-10.91	0.85
HD74156	2452007.90133	99.69	1.97
HD74156	2452236.00802	-35.73	2.08
HD74156	2452243.12308	-35.62	1.89
HD74156	2452307.88593	35.08	2.32
HD74156	2452573.14014	14.26	2.12
HD74156	2452682.96251	0.00	2.31
HD74156	2452711.82095	-43.62	2.32
HD74156	2452777.80074	-18.09	1.76
HD74156	2453017.86356	-135.63	2.06
HD74156	2453339.08245	-3.45	1.83
HD74156	2453426.89112	-169.07	1.87
HD74156	2453746.94049	153.42	1.91
HD74156	2454428.06769	117.86	1.83
HD74156	2454461.07193	-68.78	2.26
HD74156	2454464.99262	32.97	2.02
HD74156	2454490.94372	106.20	1.98
HD74156	2454492.91425	105.85	1.93
HD74156	2454545.88984	94.84	2.01
HD74156	2454601.82659	77.13	1.95
HD74156	2455202.89314	-1.01	1.41
HD74156	2455258.00214	0.38	1.28

Table A.1: Keck radial velocity data for HD128311, HD31253, HD218566, HD177830, HD99492, and HD74156.